Investigations on Influenza A Virus Morphology

Daniel Max Goldfarb, BSc MRes

Submitted in fulfilment of the requirements for the degree of

Doctor of Philosophy in Virology

Institute of Infection Immunity & Inflammation

College of Medical, Veterinary and Life Sciences

Oilthigh Ghlaschu – University of Glasgow

December 2021

Abstract

Clinical isolates of influenza A virus (IAV) typically form a pleomorphic population of virions that present as a continuum of morphologies broadly classified as filaments, bacilli, and spheres. Laboratory strains of IAV, however present mainly as spherical and bacilliform particles, suggesting a role for filaments *in vivo*. How these filaments form is not fully understood, but it has previously been shown that mutations in the viral matrix protein (M1) can be determinants of filament formation. In this work we show that filament formation also depends on multiple other genetic factors. To this end, we compared two IAV strains A/equine/Ohio/03 (O/2003) and A/equine/South Africa/4/03 (SA/2003) and found that SA/2003 could form filaments while O/2003 could not, despite no differences in their M1 sequences. To map the genetic basis of this difference, we generated reassortant viruses between O/2003 and SA/2003 and identified segments 1 (encoding polymerase basic protein 2, PB2), 4 (haemagglutinin, HA) and 6 (neuraminidase, NA) as determinants of morphology. We established that single mutations in segments 4 and 6, which alter the HA and NA proteins, alter virion morphology. To our surprise, we also identified three synonymous mutations in segment 1 of the virus that were determinants of filament formation despite not altering any known protein. We then extended this work to unravel the associated mechanisms of this change and found despite some differences in the activity of NA, contribution of HA to filament production, and differences in segment 1 RNA structure, there was no clear underlying mechanism. Given, that we were unable to identify the mechanisms associated with the change in morphology, we further extended this work to identify the factors involved in morphogenesis. To characterize IAV filament morphogenesis we employed cryogenic electron tomography (Cryo-ET) of vitrified equine fibroblasts (E. Derm). Although we were unable to identify any additional factors associated with IAV budding, we were able to generate a robust pipeline for studying filament formation. These results show that M1 is not the only determinant of IAV morphology, and that the ability to form filaments, a poorly studied but natural characteristic of IAV infection, is in fact modulated by multiple proteins and RNA determinants.

Table of Contents

List of Tables

List of Figures

Acknowledgements

Part of the work presented in this thesis has been carried out by members of the Murcia group and other members of the CVR:

- The virus rescues and cloning of the viruses used in the morphological determinants chapter (Chapter 4) were carried out by Ilaria Piras, MRC-University of Glasgow Centre for Virus Research
- The alignments of the positions of interest in the morphological determinants chapter (Chapter 4) were carried out by Jordan Bone, MRC-University of Glasgow Centre for Virus Research
- The cryogenic electron microscopy for the ultrastructure of IAV budding site chapter (Chapter 6) was conducted by James Streetly, Scottish Centre for Macromolecular Imaging
- The plunge freezing for the ultrastructure of IAV budding site chapter (Chapter 6) was conducted by Andrew Burns, MRC- University of Glasgow Centre for Virus Research

Personal Acknowledgements

I would like to thank Pablo Murcia for giving me the opportunity to join his laboratory. These last five years have been extremely challenging but have also been one of the most intellectually stimulating and exciting parts of my life. The effort that you put in to ensure that we got the most out of ourselves and our science was greatly appreciated and undoubtedly made me a better scientist.

I would also like to thank Ed Hutchinson for being extremely supportive and helpful throughout the entirety of my PhD. I will dearly miss our conversations that instilled me with so much excitement for doing science.

I would like to thank David Bhella for helping me navigate the difficult world of structural biology and giving me so much of your time.

I would like to thank Stephen Carter who has given so much of his time to help me with the final stages of my thesis.

Thank you as well to Olwyn Byron and Chris Boutell who have been great assessors during difficult times.

I would also like to say a big thank you to the rest of the Murcia group, but specifically Julien, Ilaria, Jo, Kieran, and Andreu, who have truly made coming to work something to look forward to!

A big thank you as well to my family who have been extremely supportive throughout my entire educational journey, I simply could not have done it without you.

Finally, I would like to thank my wife Hannah, who has been there every step of the way with me. I cannot thank you enough for putting up with me during the highs and lows of the PhD. Your comfort, encouragement, and occasional telling off were appreciated more than words can describe

Impact of COVID-19

Between April 2020-November 2020 I became a part of two teams in the CVR COVID-19 response and therefore was not working on my own PhD project. This hiatus was partially covered in a funded 3-month submission extension from the Medical Research Council and an additional 3 months of funding from the CVR. As part of my work during the CVR COVID-19 response, I contributed to multiple publications that are unrelated to the subject of this thesis that are listed below:

1- Banerjee AK, Blanco MR, Bruce EA, Honson DD, Chen LM, Chow A, Bhat P, Ollikainen N, Quinodoz SA, Loney C, Thai J, Miller ZD, Lin AE, Schmidt MM, Stewart DG, **Goldfarb D**, De Lorenzo G, Rihn SJ, Voorhees R, Botten JW, Majumdar D, Guttman M. (2020) SARS-CoV-2 disrupts splicing, translation, and protein trafficking to suppress host defenses. **Cell**

2- Rihn SJ, Merits A, Bakshi S, Turnbull ML, Alexander AJT, Baillie C, Brennan B, Brown F, Brunker K, Bryden SR, Burness KA, Carmichael S, Cole SJ, Cowton VM, Davies P, Davis C, De Lorenzo G, Donald CL, Dorward M, Dunlop JI, Fares M, da Silva Filipe A, Freitas JR, Furnon W, Gestuveo RJ, **Goldfarb D**, Gunson R, Hastie CJ, Herder V, Hughes J, Johnson C, Johnson N, Kohl A, Leech H, Lello LS, Li K, Lieber GJ, Liu X, Loney C, Mair D, Nichols J, Nomikou K, Orr A, Orton R, Palmarini M, Parr Y, Pinto R, Raggett S, Royle J, Cameron Ruiz N, Shepherd J, Smollett K, Stewart DG, Stewart M, Sugrue E, Szemiel A, Taggart A, Thomson EC, Tong L, Toth R, Varjak M, Wang S, Wickenhagen A, Wilkinson SG, Wyatt PG, Zusinaite E, Alessi D, Patel AH, Zaid A, Wilson SJ, Mahalingam S. (2020) A Plasmid DNA-Launched SARS-CoV-2 Reverse Genetics System and Coronavirus Toolkit for COVID-19 Research **PLOS Biology**

3- Dee K, **Goldfarb D**, Haney J, Amat JAR, Herder V, Stewart M, Szemiel AM, Baguelin M, Murcia PM (2021) Human rhinovirus infection blocks SARS-CoV-2 replication within the respiratory epithelium: implications for COVID-19 epidemiology **The Journal of Infectious Diseases**

4- Herder V, Dee K, Wojtus J, **Goldfarb D**, Rozario C, Gu Q, Jarrett R, Epifano I; Stevenson A; McFarlane S, Stewart M, Szemiel A, Pinto R, Masdefiol Garriga A, Graham S, Murcia PR, Boutell C (2021) Elevated temperature inhibits SARS-CoV-2 replication in respiratory epithelium independently of the induction of IFN-mediated innate immune defences **PLOS Biology**

Author's Declaration

I, Daniel Max Goldfarb, hereby certify that, except where explicit reference is made to the contribution of others, this thesis is the result of my own work and has not been submitted for any other degree at the University of Glasgow or any other institution. I acknowledge that the work undertaken for completion of this PhD thesis was supported by a Medical Research Council Doctoral Training Programme (MRC-DTP) studentship (Grant MR/R502327/1)

Date: 30th of December 2021

Signature:

Printed name: Daniel Max Goldfarb

Abbreviations

^{o}C	Degrees Celsius
bNA	Bacterial neuraminidase
CPE	Cytopathic effect
CRAC	Cholesterol recognition amino acid consensus
cRNA	Complementary ribonucleic acid
Cryo-EM	Cryogenic electron microscopy
DAPI	4',6-diamidino-2-phenylindole
DMEM	Dulbecco modified eagle medium
dNTPs	Deoxyribonucleotide triphosphate
dsDNA	Double stranded deoxyribonucleic acid
dsRNA	Double stranded ribonucleic acid
DTT	1,4-Dithiothreitol
EI	Equine influenza
EIV	Equine influenza virus
ER	Endoplasmic reticulum
ESCRT	Endosomal sorting complex required for transport
FIB-SEM	Focused ion beam scanning electron microscopy
HA	Haemagglutinin
hpi	hours post infection
IAV	Influenza A virus
ICV	Irregularly coated vesicles
IRF3	Interferon regulatory factor 3
LIR	LC3 interacting region
LRT	Lower respiratory tract
M	Matrix
MDCK	Madin Darby canine kidney
MES	2-(N-Morpholino)ethanesulfonic acid sodium salt, 4Morpholineethanesulfonic acid sodium
MOI	Multiplicity of infection
mRNA	Messenger ribonucleic acid
NA	Neuraminidase
NaCl	Sodium chloride
NEP	Nuclear export protein

NHBE	Normal human bronchial epithelial
NIP	Non-infectious particle
NLS	Nuclear localization signal
nm	Nanometer
NS1	Non-structural protein 1
NP	Nucleoprotein
O/2003	A/equine/Ohio/2003
ORF	Open reading frame
PA	Polyacidic protein
PolyA	Polyadenylated
PBS	Phosphate buffered saline
pH	Potential hydrogen
Pfu	Plaque forming units
PB1	Polybasic protein 1
PB2	Polybasic protein 2
PRR	Pathogen recognition receptor
qPCR	Quantitative polymerase chain reaction
RBS	Receptor binding site
RdRp	RNA dependent RNA polymerase
RIG-I	Retinoic acid-inducible gene I
RT	Reverse transcriptase
SA/2003	A/equine/South Africa/4/2003
SEM	Scanning electron microscopy
SF DMEM	Serum free Dulbecco modified eagle medium
SRP	Signal recognition particle
ssRNA	Single stranded ribonucleic acid
TEM	Transmission electron microscopy
TGN	Trans Golgi network
TMD	Transmembrane domain
Udorn	A/Udorn/1972
Vic75	A/Victoria/3/1975
VLP	Virus like particle
vRNA	Viral ribonucleic acid
vRNP	Viral ribonucleoprotein
WT	Wild type

1 Introduction

Influenza viruses are a major respiratory pathogen for a multitude of animals and is the cause of the eponymous disease, influenza. Influenza A virus (IAV), the most common and virulent form of the virus in human populations, is the focus of this study (Kremer et al., 1996).

1.1 Equine Influenza

Equine influenza (EI) is a highly contagious respiratory disease caused by equine influenza virus (EIV), which most commonly affects horses under the age of four and is the most important respiratory illness in racehorses (Arthur and Suann, 2011). In fact, some racecourses experience several outbreaks within a single racing season, which can lead to a significant economic loss for the equine industry (Smyth et al., 2011). Although EIV is rarely serious and is naturally cleared by the infected horse, the loss of valuable practice time and performance drop due to recovery from the infection can last weeks to months, which represents a large economic burden to the racing industry (Rosanowski et al., 2019).

1.1.1 Etiology

The etiologic agent of EI is an IAV, which belongs to the virus family *Orthomyxoviridae*. This virus family is comprised of seven genera: Influenza A, B, C, and D viruses, Thogotovirus, Quaranjavirus, and Isavirus. IAV, the genera responsible for equine influenza, is further subdivided into subtypes dependent on the structure of the two glycoproteins hemagglutinin (HA) and neuraminidase (NA). At time of writing there are currently 18 subtypes of HA and 11 subtypes of NA known, and the combination of the glycoprotein subtypes is given as the virus subtype e.g. H3N2 or H1N1 (Howley et al., 2021). However, the only two subtypes of IAV that have been identified in horses are H3N8 and H7N7. IAVs are further classified by host, origin, strain, number of isolation, and year of isolation. In addition to horses, IAVs are able to infect a variety of animals including but not limited to dogs, pigs, humans, and birds (Parrish and Kawaoka, 2005).

1.1.2 Transmission and clinical presentation

EIV is a highly contagious virus that is mostly spread by large liquid droplets and aerosols generated by the sneezing and coughing of an infected animal. While close contact between an infected animal and an uninfected animal is the most common cause of rapid transmission of the disease, both fomite and long-range transmission have been reported (Dionisio et al., 2021, Hughes et al., 2012). In uncomplicated cases, the infection usually lasts between two and ten days, with symptoms appearing three to five days following exposure to the virus. Infectious virus is shed during the incubation period and can continue for up to five days following the onset of the disease. However it has been shown the immunologically naïve horses can remain infectious for longer than horses that have vaccine or infection derived immunity (Landolt, 2014).
Typical symptoms include: a sudden, potentially biphasic fever, serious nasal discharge, anorexia, depression, and a non-productive continuous cough. Examination of the respiratory tract of infected horses has shown that bronchitis, tracheitis, and pharyngitis are also common hallmarks of the disease (Elton and Bryant, 2011). In addition to these symptoms, some horses also display muscle stiffness and pain, and are therefore reluctant to move. In young foals EI is a more serious disease that can cause viral pneumonia and other potentially life-threatening complications (Elton and Bryant, 2011, Daly et al., 2011).

1.1.3 Diagnosis and isolation

EIV, much like any other IAV infection, spreads rapidly amongst a susceptible population and early diagnosis and isolation is key to preventing a large outbreak. Several diagnostic tools are available to diagnose ongoing or past EIV infections including serological assays to detect NP, enzyme-linked immunosorbent assay (ELISA (Directigen™ Flu ELISA)), Next generation sequencing (NGS) and polymerase chain reaction (PCR) against nucleoprotein (NP) (Timoney, 1996, Lu et al., 2010, Rash, 2017). Most importantly for the scope of this study, is virus isolation, whereby a nasopharyngeal swab from an infected horse is isolated in embryonated chicken eggs or passaged through Madin-Darby canine kidney (MDCK) cells. The virus is detected by hemagglutinin inhibition (HI) tests using specific antisera to the two known subtypes of EIV: H3N8 and H7N7. While isolation and testing are time consuming, characterization of circulating viruses is

vital for surveillance and for the update of vaccines (Damiani et al., 2008, Bryant et al., 2011).

1.1.4 History

EIV was first isolated in Prague in 1956 during an outbreak of EI, and the causative agent was identified as a H7N7 IAV of avian origin (Sovinova and Ludvik, 1959). This EIV, A/equine/Prague/1956, was initially named equine-1-influenza and was associated with sporadic outbreaks in horses for two decades post-isolation (Lewis et al., 2011, Hughes et al., 2012). A different subtype of EIV, initially designated equine-2-influenza, was isolated in 1963 in Florida and was also of avian origin (Scholtens et al., 1964, Kitchen et al., 1963, Wilson et al., 1965). In contrast, this new EIV was a different subtype (H3N8), and this subtype is still the circulating causative agent of all modern EIV (Karamendin et al., 2016). H3N8 EIVs have caused sporadic epidemics and was the cause of the 1965 pandemic that was notable in that it infected a wide age range of horses compared to the then circulating H7N7 EIV. While there was a period of co-circulation of both subtypes of EIV in the 1960's and 1970's, H7N7 EIV has not been isolated since the 1980's and is thought to have been outcompeted by H3N8 EIV and pushed toward extinction (Karamendin et al., 2016, Murcia et al., 2011). Since the emergence of the H3N8 EIV, there have been several major outbreaks in both vaccinated and naïve horses, most notably the recent 2019 European outbreak that resulted in a suspension in horseracing in February 2019 (Paillot et al., 2019). The current EIV is now present in most of the world apart from New Zealand, Australia, Japan, and Iceland, whose eradication programs eliminated the virus after a major outbreak in 2007 (Garner et al., 2011, Rosanowski et al., 2016).

The main reservoir of IAV, and indeed EIV, is thought to be wild waterfowl (Webster et al., 1992). In fact, avian species have been shown to host a wide array of different IAV subtypes and strains, most of which are not transmissible to mammals, however, through the accumulation of mutations or reassortment events, IAVs are occasionally able to successfully infect and transmit in a new species (Parrish et al., 2015). These cross-species jumps are usually associated with outbreaks, epidemics, and in rare cases pandemics in mammal populations, but can also establish a new lineage of the virus in a different host species. The

cross-species jump of avian H3N8 into horses is a clear and important example of this phenomenon. It has been shown that establishment of a viral lineage in a new host requires a myriad of changes in the viral genome in order to both infect tissues in a different animal, as well as utilize different host machinery for replication (Parrish and Kawaoka, 2005, Parrish et al., 2015, Long et al., 2016).

1.1.5 H3N8 Evolution

EIV evolution has traditionally been studied by looking at HA phylogeny and investigation of the efficacy of vaccines (Daly et al., 1996, Kawaoka et al., 1989, Lai et al., 2004, Bryant et al., 2009). When looking at HA phylogeny, one observes two different phenomena: antigenic drift and antigenic shift. Antigenic drift is the gradual accumulation of mutations, mainly located in the globular head of HA, which can eventually result in antibody escape. Antigenic drift is the main mechanism by which IAVs as a whole are able to cause seasonal outbreaks. Antigenic shift, on the other hand, is a drastic change in the antigenic sites of the virus by means of reassortment. Reassortment occurs when two different IAV strains simultaneously infect the same cell and exchange two or more genomic segments (Webster and Govorkova, 2014). This swap of genomic segments can cause drastic changes to the virus and is in fact the mechanism that led to the 2009 H1N1 IAV pandemic (Vijaykrishna et al., 2010). During the period of co-circulation between H3N8 and H7N7 EIVs, there was reassortment observed between the subtypes (Murcia et al., 2011). This reassortment appears to have been solely with the polymerase subunits, as no H7N8 or H3N7 viruses have ever been identified. Reassortment of other genomic segments is common, however, it has been shown that segments 7 and segment 8 are somewhat conserved along the history of EIV (Chauche et al., 2018, Elton et al., 2013).

While it was initially assumed that EIV was both genetically stagnant, with respect to human IAVs, and that horses were a dead-end host for IAVs (Landolt, 2014), it has been clearly shown that EIV is continually accumulating mutations in all of its viral segments suggesting an ongoing evolutionary process (Murcia et al., 2010). For the first 20 years of H3N8 EIV it was present as a single phylogenetic lineage, but has since diverged into two distinct lineages: American and Eurasian. Of these two lineages, the American lineage represents all currently circulating viruses. The

American lineage has further split into three sub-lineages and from those sub-lineages there are further clades. The focus of this study are two EIVs that are in Florida Clade 1, which is in the sublineage Florida in the American lineage (Murcia et al., 2011). This information is of note because the viruses A/equine/Ohio/2003 and A/equine/South Africa/04/2003 used in this study are not only prototype viruses of this clade but also represent the strain of virus used in the current vaccine (Singh et al., 2018).

1.2 Influenza A Virus

1.2.1 IAV Genome

IAV is a segmented, negative-sense, RNA virus that is a member of the virus family *Orthomyxoviridae*. It has 8 segments of single stranded RNA that are connected to NP bundles. These NP bundles are capped by a polymerase complex that consists of the three polymerase protein subunits: PB2 (polymerase basic 2), PB1 (polymerase basic 1), and PA (polymerase acidic). These 8 bundles of RNA and protein are encapsidated by a helix of the matrix protein (M1), which is then itself attached to a host derived lipid envelope. In the host derived lipid envelope there are three viral proteins that are responsible for multiple parts of the viral life cycle: M2 (matrix protein 2), HA (hemagglutinin), and NA (neuraminidase). In addition to the eight proteins mentioned, the remaining major proteins NS1 (non-structural protein 1) and NEP (nuclear export protein) are responsible for immune antagonism and nuclear export respectively (Howley et al., 2021). A brief summary of each genomic segment, the proteins produced, and functions of each protein is shown below in Table 1.1.

Table 1.1: IAV genome summary: genes, proteins, and functions (Vasin et al., 2014).

Segment (Gene)	Nucleotide Length (kb)	Protein(s)	Function
1(PB2)	2.3	PB2	Cap binding subunit, polymerase complex
2(PB1)	2.3	PB1 PB1-F2 PB1-N40	Catalytical subunit of polymerase Virulence factor, interacts with PB1 and influences polymerase activity Balances PB1 and PB1-F2 expression
3(PA)	2.2	PA PA-N155 & PA-N182 PA-X	Endonuclease subunit of the polymerase complex It is not known what these proteins do, but it has been shown that it affects replication activity (Muramoto et al., 2013) Modulates the host antiviral response
4(HA)	1.7	HA	Receptor binding envelope protein
5(NP)	1.6	NP	Binds viral RNA into a vRNP complex
6(NA)	1.5	NA	Envelope protein that cleaves HA-sialic acid (receptor) interaction
7(M)	1.0	M1 M2 M42	Main component of viral membrane and important for morphogenesis Ion channel protein Splice variant of M2, which can functionally replace M2

8(NS)	.89	NS1 NEP	Antiviral antagonist and regulator of host gene expression Nuclear export protein, involved in vRNP transport out of the nucleus

1.2.2 Virion structure

IAV virions, as briefly described above, use a host-derived envelope decorated with HA and NA glycoproteins and to a lesser extent M2 (Hutchinson et al., 2014). This envelope is supported by the matrix protein M1, which forms a lattice which is closely associated with the interior of the lipid bilayer. Inside the M1 lattice, is the IAV genome in which each of the eight RNA segments is present in their own RNP complex. A simplified representation of virion organization is shown below in figure 1.1.

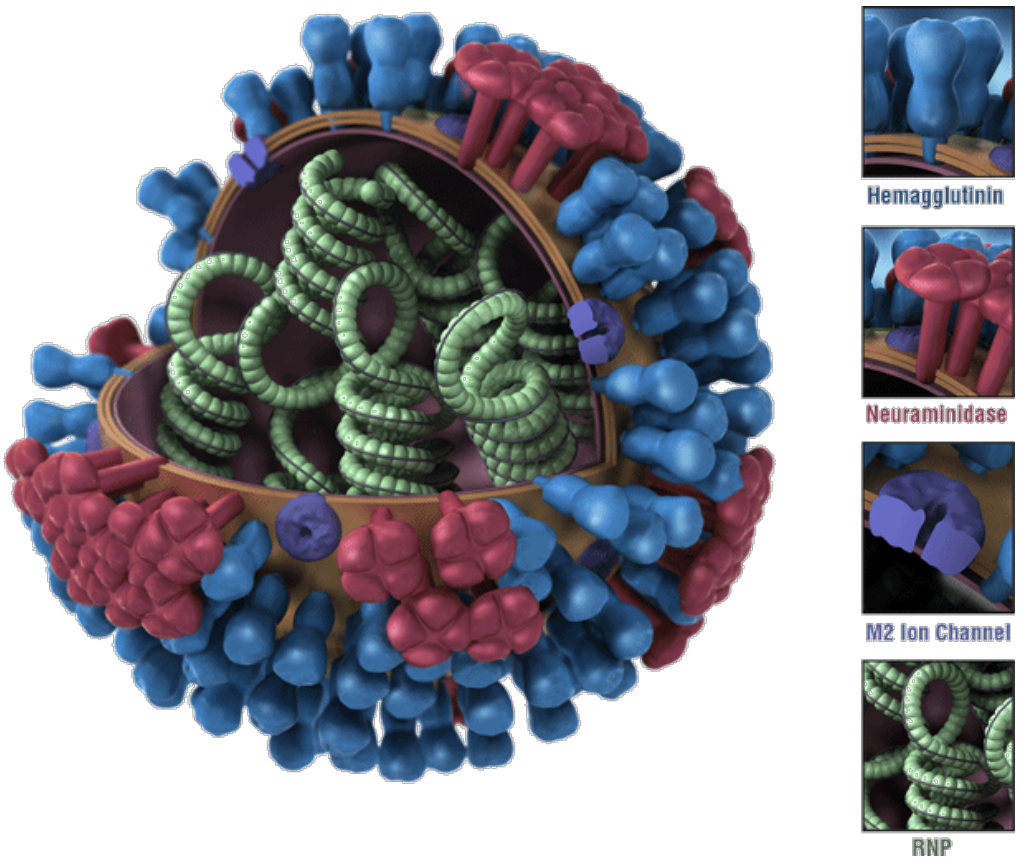

Figure 1.1 Representation of an IAV virion
Adapted from the CDC (Centers for Disease Control and Prevention, 2019).

The viral protein NS1 and cellular proteins not mentioned can be found in virions but are not essential and usually found at low levels (Hutchinson et al., 2014, Shaw et al., 2008).

In contrast to the highly ordered IAV structure shown above, IAV populations are rarely structurally homogenous and more often present as a range of sizes from 120nm diameter spheres to filamentous virions that can exceed 20μm in length (Roberts and Compans, 1998, Bourmakina and Garcia-Sastre, 2003, Harris et al., 2006). Despite the vast increase in length associated with filamentous particles, filaments maintain a consistent diameter of around 80nm (Calder et al., 2010, Vijayakrishnan et al., 2013, Dadonaite et al., 2016), which is most likely due to the differences in M1 structure (Peukes et al., 2020, Calder et al., 2010, Selzer et al., 2020). Given the difference in size between filaments and spheres, one would expect a difference in infectivity and/or replication between either morphology, however it has been shown that there is little to no difference in either characteristic within a population (Roberts et al., 1998, Noda et al., 2006, Rossman et al., 2010b). To this end, it has also been shown that despite the difference in available space in the virion each morphology only incorporates one set of vRNPs (Noda et al., 2006, Calder et al., 2010, Rossman et al., 2010b, Vijayakrishnan et al., 2013). However, the organization of glycoproteins between spherical (~120nm), bacilliform (250nm), and filamentous (>250nm) particles (Vijayakrishnan et al., 2013) is not similar, and in fact the filamentous virions have a characteristic polarization of NA on the proximal end of a budding virion and a polarization of RNPs on the distal end (Harris et al., 2006, Calder et al., 2010, Vijayakrishnan et al., 2013, Vahey and Fletcher, 2019a).

1.3 IAV replication

The IAV replication cycle is defined as the series of steps that start with the attachment of a virus particle to the receptor on a permissive host cell and ends with the release of newly formed virions capable of infecting other permissive cells. Below in figure 1.2 is a schematic representation of the major steps of the IAV life cycle.

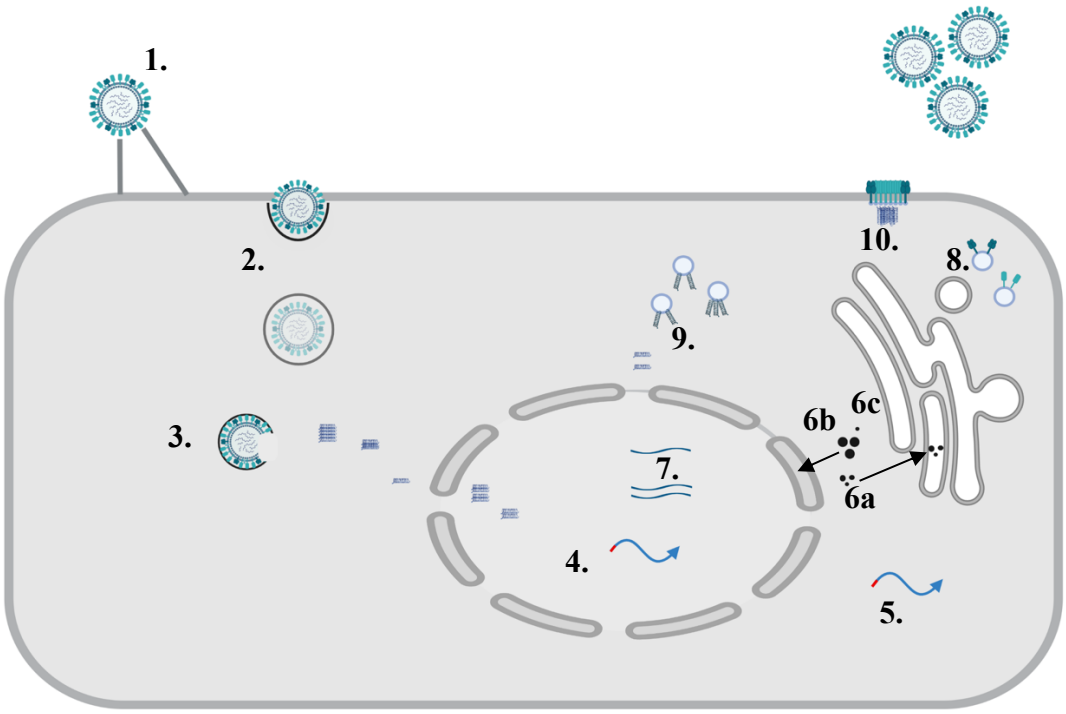

Figure 1.2 Schematic representation of the IAV replication cycle
1. Receptor binding. 2. Endocytosis. 3. Acidification, fusion, and release of RNPs, followed by translocation of RNPs to the nucleus. 4. mRNA transcription 5. Translation of viral proteins 6a. HA, NA, and M2 sorting in the endoplasmic reticulum 6b. Trafficking of PB1, PB2, PA, NP, M1, and NEP into the nucleus. 6c. NS1 in the cytoplasm. 7. RNA replication (vRNA and cRNA) 8. HA and NA trafficking to the plasma membrane. 9. vRNP trafficking to the plasma membrane. 10. Assembly and budding. Created with BioRender.com.

1.3.1 Virion binding and entry

In order to enter the host cell and begin the replication process IAV must first bind to a cellular receptor. Specifically, the receptor binding protein HA binds terminally linked sialic acids that are present on the cell surface and bound to a variety of host glycoproteins and glycolipids. Not all sialic acid linkages are receptors for all IAVs, in fact the structure of the sialic acid is important for HA binding affinity and the difference in these linkages affects tropism. While there are a variety of sialic acid conformations, the general distinction in the context of IAV is between α2,3 and α2,6 linked sialic acids. The main difference between these two types of sialic acid conformations is the linkage between the terminal galactose and the sialic acid. For example, if the linkage occurs between the 2nd carbon of the sialic acid hexose and the 3rd carbon of the galactose hexose then the sialic acid is a α2,3 linkage (Ito et al., 2000). This small difference leads to a big difference in HA binding preference, and in fact is a major determinant of tropism (Shinya et al.,

2006). It is thought that the difference in binding preference is due to the glycan topology of the sialic acid with α2,6-linked sialic acids having an umbrella-like topology, whereas α2,3 sialic acids have a cone-like topology (Chandrasekaran et al., 2008). Avian and equine influenza virus HAs preferentially bind α2,3 sialic acids, (Collins et al., 2014, Shinya et al., 2006), while human influenza virus HAs preferentially bind α2,6 sialic acids (Matrosovich et al., 2004). The difference in binding preference also leads to a difference in tissue tropism, as α2,3 sialic acids are predominately found in the epithelial cells of the avian gut (Shinya et al., 2006) and ciliated epithelial cells in the equine upper respiratory tract (Collins et al., 2014), while α2,6 sialic acids are present in the human respiratory tract on both ciliated and unciliated cells (Matrosovich et al., 2004). It is important to note however, that there is not a clear presence or absence of specific linkages in different tissues, but rather a distribution of linkages with different proportions along the respiratory tract of mammals (Barnard et al., 2019).

Once an IAV virion is bound to the cell, it can then by internalized by the cell through three known mechanisms: clathrin-independent or clathrin-dependent endocytosis (Matlin et al., 1981, Sieczkarski and Whittaker, 2002), or for larger filamentous virions, micropinocytosis (Rossman et al., 2012).

1.3.2 Virus fusion and vRNP translocation to the nucleus

Independent of the mechanism of entry the virus will end up in a rapidly acidifying vacuole, which when it reaches a certain pH range, will initiate fusion between the membrane of the vacuole and the virus (Stegmann et al., 1990). The process of endosome maturation occurs as the endosome goes from the cell surface toward the cell interior and coincides with acidification by a vacuolar ATPase (Murphy, 1991). IAV fusion, which is pH dependent, also varies between IAV strains, and is triggered by the irreversible unfolding of the hydrophobic fusion peptide from the core of the HA trimer to the vacuole membrane (Galloway et al., 2013). The conformational change of the HA protein and its attachment to the vacuole membrane brings both membranes close together until the vesicle and viral membranes fuse (White and Whittaker, 2016). Concurrently with the endosome maturation, the viral particle is also acidifying through a similar process. M2, the ion channel protein that is present at low abundance in the viral particle, is responsible for the acidification and increase of potassium concentration inside the

virion (Wang et al., 1995, Hutchinson et al., 2014). While at normal pH and low salt concentration vRNPs are bound to M1 (Zhirnov, 1992, Ye et al., 1999), at low pH M1 disassociates from the vRNP complex (Bui et al., 1996). This dissociation is crucial for the next stage of the replication cycle, as it now frees the vRNPs to translocate to the nucleus (Bui et al., 1996). Now that the viral and vesicular membranes are fused, the vRNPs can now exit the viral particle and enter the cytoplasm (Cros et al., 2005). Once they enter the cytoplasm, they are then ferried to the nucleus by cellular importin-α proteins that recognize the nuclear localization signals on the NP proteins (Cros et al., 2005, Gabriel et al., 2008, Gabriel et al., 2011).

1.3.3 Transcription of viral mRNA

mRNA transcription via the viral RNA dependent RNA polymerase (RdRp) of each genome occurs once the vRNPs enter the nucleus. IAV uses a process called cap-snatching in which 10-15 nucleotides from the 5’ end of capped host pre-mRNA are cleaved by the viral endonuclease PA, which then produces a short nucleotide sequence that can act as a primer for transcription by the RdRp (Dias et al., 2009, Reich et al., 2014, De Vlugt et al., 2018). When the RdRp gets to the 3’ end of the mRNA sequence it generates a polyadenylated tail by stuttering over the uracil residues present at the 5’ end of the vRNA sequence (De Vlugt et al., 2018, Poon et al., 1998). Together, these processes allow the newly produced transcripts to hijack the host machinery to be translated into viral proteins without being targeted for degradation. In addition to the conventionally transcribed mRNA, segments 7 and 8, contain two ORFs each that are transcribed using the host pre-mRNA splicing machinery, which recognizes sequences on segment 7 and 8 that are similar to eukaryotic splicing signals (Lamb et al., 1981, Dubois et al., 2014). These two mRNA transcripts correspond to the M2 and NEP proteins which are necessary for the viral life cycle (McCown and Pekosz, 2005, O'Neill et al., 1998).

1.3.4 Translation of viral proteins

Due to the presence of a 5’-methylguanylate cap and a polyA tail, viral mRNA transcripts are able to use the host machinery to be translated into viral proteins while avoiding degradation. Apart from the main viral proteins, there are several accessory and minor protein products that are expressed at later stages in the

virus reproductive cycle. One of these proteins PB1-F2, which induces apoptosis, is produced via leaky ribosome scanning and occurs in the alternative +1 reading frame of the segment 2 mRNA (Chen et al., 2001). In segment 2 PB1-N40, a truncated form of PB1 that is initiated from a start codon downstream of the initial start codon is also produced and is responsible for maintaining the balance between expression of the full length PB1 and PB1-F2 expression (Wise et al., 2009). Other alternative polypeptides are produced at this stage, including but not limited to PA-X, PA-N155, and PA-N182 (Muramoto et al., 2013). These accessory proteins appear to be strain dependent and not necessary for successful replication of the virus.

1.3.5 Translocation of nuclear proteins

PB1, PB2, PA, and NP are all transported into the nucleus once they have been translated to provide further transcriptional support as subunits of the RdRp. These proteins are trafficked to the nucleus in a similar fashion as the vRNPs in the beginning of the replication cycle, as they each possess their own NLS (Hutchinson and Fodor, 2013). Despite the similarity to the initial translocation of vRNPs to the nucleus, the polymerase proteins use different host factors for each protein to complete the trafficking (Hutchinson and Fodor, 2013). After translation, M1, NS1, and NEP are also translocated to the nucleus whereby M1 is responsible for modulating the directionality of nuclear transport (Martin and Helenius, 1991), NS1 is responsible for abrogating the interferon response (Ayllon and Garcia-Sastre, 2015), and NEP is responsible for recruitment of CRM1 and nuclear export of vRNPs (Huang et al., 2013). Together these proteins act to produce further mRNA and thereby more viral proteins, as well as produce both complementary RNA (cRNA) and vRNA.

1.3.6 Maturation of IAV membrane proteins

IAV membrane proteins are synthesized in endoplasmic reticulum (ER) associated ribosomes and are co-translationally directed to the ER through interactions of their hydrophobic targeting sequences and the signal recognition particle (SRP) (Bos et al., 1984, Daniels et al., 2003, Dou et al., 2014, Hull et al., 1988). Once the polypeptides are bound to the SRP they are targeted to the SRP receptor that is present on the ER membrane. The still elongating HA, NA, and M2 polypeptides

are then passed into the ER lumen with the help of Sec61 protein channel called the translocon (Hull et al., 1988, Gorlich et al., 1992). While in the ER the transmembrane domain (TMD) of the membrane proteins are partitioned to ensure that they are of appropriate length to activate membrane integration (Hessa et al., 2007), properly folded with the help of N-linked glycans (Daniels et al., 2003), and oligomerized (Wang et al., 2008, Holsinger and Lamb, 1991). Following oligomerization, HA, NA, and M2 are trafficked to the Golgi apparatus before making the final journey to the plasma membrane.

1.3.7 NS1 function

NS1 has multiple functions in the IAV life cycle, however the most important function of the NS1 protein is antagonism of the interferon (IFN) response. One of the mechanisms by which NS1 delays or stops the normal cellular innate immune response, is by inhibiting the retinoic acid-inducible gene I (RIG-I) sensing of double stranded RNA (dsRNA). It accomplishes this by restricting the activation of IFN regulatory factor 3 (IRF3) (Mibayashi et al., 2007).

1.3.8 Production of cRNA, vRNA, and vRNP

When the initial protein products are translocated back to the nucleus Figure 1.2, they encounter vRNPs that are present from the initial steps of the viral infection and use these vRNPs as templates to generate both cRNA and vRNA. In early stages of infection, the emphasis is on mRNA production in order to generate sufficient amounts of viral proteins, while in later stages of the infection there is a shift to cRNA and vRNA production. This shift toward replication of the viral genomes involves the production of cRNA, a template for genomic vRNA synthesis (Shapiro and Krug, 1988). One of the catalysts of this switch is thought to be M1, which as mentioned before has already been trafficked into the nucleus. It has been shown that M1 is responsible for transcription inhibition by vRNP binding, and this inhibition is one of the factors that results in a change of templates from genomic vRNA to cRNA (Ye et al., 1999, Baudin et al., 2001). Another and possibly more important factor in the change between transcription of mRNA and replication of vRNA involves the orientation and interactions between the RdRp and mRNA or cRNA. While transcription of mRNA occurs between a polymerase complex that is attached to the vRNP, replication of vRNA requires

RdRp that are not associated with the vRNP (Jorba et al., 2009). To this end, it has been shown that genome replication occurs in the absence of a primer and is solely dependent on the cDNA template (Vreede et al., 2008, Reich et al., 2014). A structural insight into this mechanism has shown that there are conformational changes of the polymerase that enables the process from pre-initiation to recycling of the template (Wandzik et al., 2020).

1.3.9 HA and NA transport to the plasma membrane

After the maturation of HA and NA as detailed in 1.3.6, the glycoproteins are trafficked through the trans-Golgi network (TGN) to the cell surface. While it has been shown that HA and NA colocalize shortly after synthesis and that they are transported to plasma membrane via apical recycling endosomes, the specifics of the transport pathway have not been elucidated (Sato et al., 2019). Current evidence suggests that HA and NA are lipid raft associated proteins that are targeted to the apical surface (Ohkura et al., 2014). These apical targeting vesicles are not Rab11 associated and are likely associated with RAB17 and RAB23 (Sato et al., 2019). The IAV glycoproteins are specifically targeted to the site of budding, which is characterized by its lipid profile, cholesterol-rich coalescence of raft domains (Hess et al., 2005). It is also thought that the glycoprotein organization and membrane preference is due to the cytoplasmic domains of the HA and NA, which when removed can change virus morphology and infectivity (Zhang et al., 2000, Mitnaul et al., 1996, Jin et al., 1997, Jin et al., 1994). While HA and NA have been shown to co-cluster in this budding region with M2 present on the periphery, as well as the rough organization of the other cellular proteins, the processes underlying IAV budding site organization are largely unknown (Leser and Lamb, 2017).

1.3.10 vRNP transport from the nucleus to the site of budding

Nuclear export of vRNPs is a highly coordinated process dependent on viral proteins M1 and NEP, individual vRNPs, and host factors CRM1 and Hsc70 (Iwatsuki-Horimoto et al., 2004, Boulo et al., 2007, Neumann et al., 2000, Watanabe et al., 2014). In order to the exit the nucleus M1, NEP, and individual vRNPs form a complex that enables them, with the help of the host factors mentioned above, to exit the nucleus through the nuclear pore complexes (Manz

et al., 2012). CRM1 disassociates shortly after nuclear exit and vRNPs associate with Rab11 vesicles (Amorim et al., 2011). These Rab11 vesicles are transported to either a liquid organelle inclusion body closely associated to the ER (Alenquer et al., 2019) or a modified ER membrane that is close to the site of budding (de Castro Martin et al., 2017). While there is a large amount known about vRNP transport, there is also a fair amount of contradictory evidence and multiple plausible models for vRNP trafficking from the nucleus to the IAV budding site. For example, while it is known that RAB11 coated structures are responsible for transport from the nucleus to the modified ER or liquid organelles adjacent to the site of budding, it is unclear whether they are recycling endosomes coated in RAB11, a modified tubulated ER that extends throughout the cell, or some combination thereof. One such model suggests that the initial transport of RNPs occurs via RAB11 coated vesicles that are either trafficked in a microtubule dependent or independent manner from the microtubule organizing center (MTOC) (Amorim et al., 2011) toward a liquid organelle present near the ER exit site (Alenquer et al., 2019). This liquid organelle is essentially a viral inclusion body, whereby individual RNPs can find other RNP binding partners before then being transported toward the budding site. Another model suggests that RNP transport is endosome independent, and rather dependent on major ER remodeling. This model suggests that a combination of recruitment and remodeling of the rough ER to the area near the MTOC is responsible for transporting RAB11 irregularly coated vesicles (ICV) from the nucleus to the cell surface (de Castro Martin et al., 2017).

1.3.11 Assembly and Budding

Virion formation occurs at the plasma membrane and is specifically thought to occur in areas of lipid rafts (Barman et al., 2001, Leser and Lamb, 2005). Recent work on the subject suggests that the lipid raft hypothesis is incorrect, as lipid raft characteristic molecules, sphingolipids and cholesterol, are actually not present in higher proportions in budding sites (Wilson et al., 2015). To this end, it was found that by depleting cholesterol and thereby disrupting lipid raft formation, the number of released viruses increases (Barman and Nayak, 2007). Despite these contradictory results, it was found that by depleting cholesterol, virion stability does decrease, which suggests that while lipid rafts are not essential for IAV budding

they may be important for the stability of virions (Bajimaya et al., 2017). The accepted model for IAV budding initiation is as follows: HA and NA are trafficked to specific regions on the apical plasma membrane with M2 accumulating on the boundaries of the lipid raft (Leser and Lamb, 2017), M1 is then recruited and associates with the cytoplasmic tails of HA and NA, and then RNP bundles are trafficked and bind M1.

While M1 can associate with the plasma membrane independent of any other viral factors, the strength of this association increases with the presence of the viral glycoproteins on the cell surface (Jin et al., 1997, Baudin et al., 2001, Hilsch et al., 2014). The importance of this association is shown in the drop in budding efficiency seen in HA, NA, and M2 TMD deletion viruses (Chen et al., 2008, Zhang et al., 2000). Once M1 is present on the plasma membrane, vRNPs that are already present in a 7+1 cluster (7 RNP segments surrounding a central RNP) (Noda et al., 2006), are recruited to viral protein enriched areas of membrane and initiate budding (Chou et al., 2013).

The specific mechanistic details of IAV budding have not been elucidated, but what is known however, is that HA and NA when cellularly expressed are both capable of initiating membrane curvature in the absence of M2 or M1 and can even produce budding virus-like particles (VLPs) (Chen et al., 2007). By introducing M1 or M2 into the viral protein expression system described in Chen et al., 2007, it was found that the structure of the VLPs produced has an organizational structure more similar to that of IAV (Chlanda et al., 2015). In fact this expression system that included HA, NA, M1, and M2, was even able to replicate the budding mechanism that is observed in IAV infection, whereby the membrane joining the host cell and the nascent viral particle is constricted until scission occurs (Chlanda et al., 2015). IAV scission, the last step in the budding process, has been clearly demonstrated to be a function of the M2 protein (Rossman et al., 2010b). The role of M2 in budding is two-fold: induction of membrane curvature, as well as the final scission of the viral and cellular membranes. M2-mediated abscission represents an endosomal sorting complex required for transport (ESCRT) protein independent method of viral abscission that is dependent on the action of the M2 cytoplasmic tail and localization near the neck of viral budding (Rossman et al., 2010b).

1.3.12 Non-infectious particles

The multifactorial process of the IAV replication cycle can and does result in errors at various stages. One such error is the production of viral particles that resemble mature virions but lack one or more characteristics of mature virions that make them incapable of completing a full round of replication. These non-infectious particles (NIPs) are defined as a virus particle that cannot complete a successful round of replication without the presence of a co-infecting virus (Brooke, 2014). Under the umbrella of NIPs there are multiple categories, two such categories are: semi-infectious particles (SIPs) and defective interfering particles (DIPs) (Marcus et al., 2009, Wei et al., 2007). Semi-infectious particles are viruses that do not contain a full complement of RNPs, so they are able to infect a host cell but not complete the replication cycle unless they are complemented with the missing genomic segment (Fonville et al., 2015). Defective interfering particles on the other hand, have internal deletions in one of the eight RNA segment, which can result in replication interference through competitive inhibition and stimulation of IFN that can make cells refractory to infection (Alnaji and Brooke, 2020). Given that RNPs are not required for budding, as described above, another class of NIPs are empty virions (Gomez-Puertas et al., 2000). While NIPs appear as a useless byproduct of IAV replication, it has been shown that the ratio of NIPs to infectious viruses can be as high at 10:1 in a natural infection (Brooke et al., 2013).

1.4 IAV morphology

Viral particles isolated from clinical infections typically display as a pleiomorphic population that consists of spherical, bacilliform, and filamentous particles that range in size from 120nm to more than 20μm (Itoh et al., 2009, Seladi-Schulman et al., 2013, Chu et al., 1949). The filamentous segment of this population is lost in cell culture or embryonated chicken egg passage. Thus, most laboratory adapted strains of IAV present as a more homogeneous population of spheres and bacilli (Seladi-Schulman et al., 2013). However, it has been shown that a low number of passages in an *in vivo* model can change the phenotype back from spherical to filamentous. The phenotypic shift from spherical to filamentous, or vice versa, has not been observed for all strains and some strains which have undergone extensive laboratory passage still maintain filamentous morphology (Bourmakina and Garcia-Sastre, 2003). This appears to be a conserved phenotype of

Orthomyxoviridae viruses as it has been observed in all influenza viruses as well as salmon anemia virus (Nakatsu et al., 2018, Koren, 1997).

1.4.1 Genetic determinants of morphology

There are multiple viral factors that have been shown to influence morphology and most have been mapped to segment 7 of the IAV genome (Dadonaite et al., 2016). Other genetic determinants of morphology have been identified on segments 4, 5, and 6, which have been shown to alter the HA, NP, and NA proteins respectively (Rossman et al., 2010a, Zhang et al., 2000, Jin et al., 1997, Bialas et al., 2014). Likewise, mutations on segment 7 that alter the structure of M2 have also been associated with a change in morphology. Although these determinants are located outside the M1 protein, it appears that even the seemingly matrix independent structural changes affect morphology via interactions with the matrix protein.

As described earlier in section 1.3.11, HA and NA are sufficient to initiate budding in a VLP system, however M1 and M2 are required to give structure to the budding membranes. Although, in the absence of the glycoproteins, M1 and M2 are not sufficient to initiate budding and in fact M1 is not visualized at the cell membrane without the presence of HA and NA, suggesting a role for the glycoproteins in M1 recruitment (Chlanda et al., 2015). To this end, it has also been observed that the binding avidity between the RNP bundles and M1 is a strong correlate with morphology, as vRNPs that cannot disassociate as readily from complex with M1 in the earlier stages of the replicative process are more likely spherical (Liu et al., 2002).

The importance of segment 7, and specifically M1, to morphology is no surprise considering the importance of M1 in both the stability and morphogenesis of IAV. M1, as described in 1.2.2 makes up the matrix layer of the viral particle, and it is plausible that due to its role as the main structural protein of the virus that alterations to this protein structure can have significant effects on virus morphology (Peukes et al., 2020). To this end, several amino acids have been identified as determinants of morphology when observed in certain genetic backgrounds. For example, the key amino acid positions that modulate morphology in the context of a H3N8 EIV M1 protein (Elton et al., 2013) may not have the same importance in the context of a Human H1N1 (Bourmakina and

Garcia-Sastre, 2003). A summary of the known amino acid positions in M1 that affect virus morphology is shown below in Table 1.2.

Table 1.2: A summary of the known amino acid morphological determinants of M1.

M1 position	Phenotype	Genetic Background	Reference
30Asp	Spherical->Filamentous	A/California/04/2009	(Bialas et al., 2012)
41Val	Filamentous->Spherical	A/Udorn/1972 A/Victoria/3/1975	(Roberts et al., 1998, Elleman and Barclay, 2004)
41Pro	More Filamentous	A/Netherland/602/2009	(Campbell et al., 2014)
85Asn*	Filamentous->Spherical	A/Equine/Newmarket/11/2003 A/Puerto Rico/8/1934	(Elton et al., 2013)
85Ser*	Spherical->Filamentous	A/Puerto Rico/8/1934 A/Equine/Miami/1963	(Elton et al., 2013)
87Ser	Spherical->Filamentous	A/Puerto Rico/8/1934	(Seladi-Schulman et al., 2013)
92Ser	Spherical->Filamentous	A/Puerto Rico/8/1934	(Seladi-Schulman et al., 2013)
95Lys	Filamentous->Spherical	A/WSN/1933 Segment 7: A/Udorn/1972	(Bourmakina and Garcia-Sastre, 2003)
101Gly	Spherical->Filamentous	A/Puerto Rico/8/1934	(Seladi-Schulman et al., 2013)
102Ala	Spherical->Filamentous	A/WSN/1933	(Burleigh et al., 2005)
169Ile	Filamentous->Spherical	A/Netherland/602/2009	(Seladi-Schulman et al., 2013)

183Ala	Spherical->Filamentous	A/WSN/1933	(Zhang et al., 2015)
185Ala	Spherical->Filamentous	A/WSN/1933	(Zhang et al., 2015)
198Lys	Filamentous->Spherical	A/Netherland/602/2009	(Seladi-Schulman et al., 2013)
204Asp	Filamentous->Spherical	A/WSN/1933 Segment 7: A/Udorn/1972	(Bourmakina and Garcia-Sastre, 2003)
218Ala*	Spherical->Filamentous	A/WSN/1933	(Elleman and Barclay, 2004)

While some of the mutations listed above are portable into multiple virus backbones, it appears that others are highly context dependent suggesting unsurprisingly that there are M1 differences between strains. Initial studies into the genetic source of morphology compared the sequences of filamentous and spherical strains and identified any dissimilarities. From these dissimilarities, mutant viruses were able to be generated using reverse genetics and the effect of each amino acid on morphology was observed. For example, one study observed that spherical strains contained a lysine at position 95 and an aspartic acid at position 204 (Bourmakina and Garcia-Sastre, 2003). When these mutations were introduced into segment 7 of a filamentous virus A/Udorn/1972 (Udorn), it was found that these amino acids were sufficient to stop filament production in the context of a spherical virus A/WSN/1933 (WSN) (Bourmakina and Garcia-Sastre, 2003). Likewise, another study looked at 41Val, a residue present in spherical strains, and found that it was also able to generate spherical viruses in a filamentous backbone such as A/Victoria/3/1975 (Vic75). However in this context 95Lys does not have the same effect as it has in the context of WSN + Udorn M. This apparent disagreement makes a clear case for the context dependence of some IAV morphological determinants (Elleman and Barclay, 2004).

The second protein produced by a spliced version of segment 7 mRNA, M2, also has an important role to play in morphology. As mentioned previously, the cytoplasmic tail and transmembrane domain of M2 are important for correct virion

formation and alterations to these regions can have significant effects on virion stability and infectivity (Rossman et al., 2010b). A possible mechanistic explanation for this phenomenon is the interactions between M2 cytoplasmic tails and M1 in the early stages of morphogenesis (Grantham et al., 2010, McCown and Pekosz, 2006). For examples, the LC3-interacting region on the carboxy terminus of M2 has been shown to affect the extent of filament budding and alterations to this region can reduce the size and proportion of filaments produced (Beale et al., 2014).

Although the mechanisms by which protein-protein interactions govern IAV morphology in unclear, it is clear that morphogenesis is a multi-factorial process. Segment 7 amino acid determinants of morphology are located along the length of the M1 protein, but the exact mechanism of action is unknown for each of them. While some identified changes in the protein like Ser183Ala and Thr185Ala have been hypothesized to affect the folding of the C-terminal domain and thereby effect the stability of the matrix helices (Peukes et al., 2020, Selzer et al., 2020), other amino acid determinants have no known mechanism. In addition to destabilizing mutations to the matrix protein, interactions between two M1 subunits, other viral proteins, and cellular factors all contribute to morphological changes. Recently, the full-length native structure has been solved for the M1 protein which opens further avenues to study matrix dependent morphological changes (Selzer et al., 2020, Peukes et al., 2020)

1.4.2 Cellular determinants of morphology

In addition to filamentous determinants that exist in the viral genome, the cell type infected has a significant role in the shape of the viral particles being produced (Roberts and Compans, 1998). The degree of cellular polarization is an important factor for virion morphology, as it has been shown that the same virus infecting two different types of fibroblasts produced differing levels of filaments (Al-Mubarak et al., 2015). In addition, the cellular cytoskeleton is an important indicator of virion morphology. For example, upon treating cells with cytochalasin D, a toxin that inhibits the polymerization of actin, the number of filamentous virions produced drops significantly, without affecting spherical virions (Roberts and Compans, 1998, Simpson-Holley et al., 2002). In a similar vein, disruption of the microtubule network using nocodazole can also specifically hamper filament production,

however recent data appears to suggest that it may be a more global effect (Roberts and Compans, 1998, Amorim et al., 2011). As described in section 1.3.10, Rab11 is a family of key GTPases involved in the transport of RNPs and other viral proteins to budding adjacent organizational sites, and it was found that depletion of Rab11a blocks filament formation (Bruce et al., 2010). In contrast, silencing of the Rab11 proteins resulted in a log reduction of viral titers from infected cells (Eisfeld et al., 2011). When knocking down FIP3, a rab11 interacting protein, it was found that filament production was reduced, suggesting a specific role for FIP3 in filament production (Bruce et al., 2010). Rab11 on the other hand, is important for vRNP transport so its role in virion budding appears to be important for all virion production and not specifically filaments (Amorim et al., 2011). Another cellular factor that is important for filament formation is cholesterol. Depletion of cholesterol completely abrogates filament production which is most likely due to its possible association with M2 cytoplasmic tails (Rossman et al., 2010b).

1.4.3 Environmental effects on morphology

Cellular and viral factors are clearly important for filament formation; however, it has been shown recently that the extracellular environment has a role to play in virus morphology. For example, it has been shown that virus grown in the presence of antibody directed against M2 disrupts filament formation and skews the virus population toward spheres (Roberts et al., 1998, Rossman et al., 2010b). Likewise, it has also been shown that virus grown in the presence of neuraminidase inhibitor skews the morphological population toward smaller viruses (Vahey and Fletcher, 2019b). In addition, it has been postulated that the presence of a low-Reynolds number mucosal environment might increase the proportion of filaments in the viral populations (Vahey and Fletcher, 2019a). Taken together, these results suggest that the extracellular environment can also modulate filament populations.

1.4.4 Functional differences between morphologies

The effect of the extracellular environment on the proportion of different viral morphologies (Vahey and Fletcher, 2019a) and the presence of pleiomorphy in clinical isolates of IAV (Chu et al., 1949, Seladi-Schulman et al., 2013) suggests a

functional role for filamentous forms *in vivo*. To this end, filamentous IAV has been shown to move with directed motion and penetrate host mucus to a larger extent than spherical and bacilliform particles in a three-dimensional air-liquid interface culture system (Vahey and Fletcher, 2019a). Despite these attributed functions, the biological significance of the various IAV morphologies is unknown.

2 Aims

The overall aim of this project was to identify the genetic determinants of IAV morphology and understand the multi-factorial process of IAV morphogenesis, using super-resolution confocal microscopy and cryogenic electron microscopy.

Specifically, I aimed to:

I. To identify the molecular determinants of H3N8 EIV morphology
II. To analyze the role of specific nucleotide and amino acid changes on EIV structure.
III. To confirm which specific mutations are associated with a morphological shift
IV. To evaluate the role of these specific mutations in the resulting protein or RNA structure
V. To identify the underlying mechanisms by which the mutations are determining virus shape
VI. To characterize the ultrastructure of the IAV budding site to identify factors involved in morphogenesis.

3 Materials and methods

3.1 Antibodies and dyes

Table 3.1: Primary antibodies raised against IAV

Antibody	Application	Source
Mouse monoclonal anti-H3	Immunofluorescence (1:2000)	Parrish Lab, Cornell University
Rabbit polyclonal anti-NP	Immunofluorescence (1:1000)	Parrish Lab, Cornell University
Mouse monoclonal anti-NA	Immunofluorescence (1:1500)	Parrish Lab, Cornell University

Table 3.2: Plant lectins

Lectin	Application	Source
Maackia Amurensis Lectin II (MAL II), Biotinylated	Immunofluorescence (10µg/mL)	Vector Laboratories #B-1265-1
Sambucus Nigra Lectin (SNA, EBL), CY5®	Immunofluorescence (10µg/mL	Vector Laboratories #CL-1305-1

Table 3.3: Secondary antibodies

Antibody/Stain	Application	Source
Goat Anti-Mouse IgG Alexa Fluor 488	Immunofluorescence (1:1000)	Abcam #ab150113
Donkey Anti-Rabbit IgG Alexa Fluor 647	Immunofluorescence (1:1000)	Abcam #ab150075
Fluorescein Avidin D, FITC	Immunofluorescence (15µg/mL)	Vector Laboratories A-2001-5

Table 3.4: Fluorescent dyes and mounting media

Mounting media	Application	Source
Vectashield HardSet with DAPI	Immunofluorescence /Immunohistochemistry (7µL)	Vector Laboratories H-1500
Vectashield HardSet with Phalloidin-TRITC	Immunofluorescence (7µL)	Vector Laboratories H-1600

3.2 Oligonucleotides

Table 3.5: Oligonucleotides

Name	Sequence (5'->3')	T_m	GC %
IAV Uni12	GCCGGAGCTCTGCAGATATCAGCRAAAGCAGG	77	56
IAV Uni12g	GCCGGAGCTCTGCAGATATCAGCGAAAGCAGG	79	59
A/Equine/Ohio/2003 PB2 Forward	GAGAGTCAGCAAAATGGGAGTGGA	62	50.0
A/Equine/Ohio/2003 PB2 Reverse	TCCCCTTTGATCCCGAACTCTT	61	50.0
A/Equine/Ohio/2003 NP Forward	GACGAAAAGGCAACGAACCC	69	57.1
A/Equine/Ohio/2003 NP Reverse	AACTCCTCAGCATTGTCTCCG	60	55.0
Universal M Forward	AAGACAAGACCAATCCTGTCACCTCT	60	52.3
Universal M Reverse	TCTACGCTGCAGTCCTCGCT	70	54.5
PB2 Probe (6-FAM/TAMRA)	AGTGGTGGTGAGCATTGACCG	68	46.1
NP Probe (6-FAM/TAMRA)	CGTGCCTTCCTTTGACATGAGC	67.	60.0
M Probe (6-FAM/TAMRA)	TCACGCTCACCGTGCCCAGTG	76.	66.6

3.3 Cell culture

3.3.1 Cell maintenance

Cell maintenance media for normal cellular maintenance varied by cell type used. For Madin-Darby Canine Kidney (MDCK; ATCC CCL-34) and 293T (ATCC CRL-3216) cells were grown at 37°C and 5% CO_2 in Dulbecco's modified Eagle's medium (DMEM) high glucose, GlutaMax, and pyruvate (ThermoFisher Scientific) supplemented with 10% Fetal Bovine Serum (FBS; Gibco Life Technologies).

While, Equine Dermal Fibroblast cells (E. Derm, ATCC CCL-57) were grown at 37ºC and 5% CO_2 in DMEM high glucose, GlutaMax, and pyruvate supplemented with 15% Fetal Bovine Serum (FBS; Gibco Life Technologies).

3.3.2 Subculture

Cells were routinely grown in either 75cm^2, 150cm^2, 250cm^2 flasks and passaged when reaching confluence for MDCK and 293T, and 95% confluence for E. Derm cells. For propagation, the cell monolayer was washed with phosphate buffered saline without calcium (PBS 1X, Gibco ThermoFisher Scientific, pH 7.3) and incubated with 3mL, 5mL or 8mL respectively of 0.25% EDTA trypsin (TrypLE Express, Gibco) for 5 minutes at 37º C with 5% CO_2 for E. Derm cells and 293T, and 30 minutes at 37ºC with 5% CO_2 for MDCK. Once detached the cells were diluted 1:6 in maintenance media and then added into sterile flasks containing 10mL, 20mL, or 30mL of maintenance media depending on flask size. Additional cells were counted and used for assays.

3.3.3 Long-term storage

Cells were kept in liquid nitrogen for long term storage. Post-trypsinization, cells were centrifuged at 200xg for 5 minutes and then resuspended in storage media (90% FBS, 10% dimethyl sulfoxide (DMSO, ThermoFisher Scientific). The suspension was counted and then aliquoted at a concentration of 2.5 x 10^6 cells/vial in 2mL cryogenic tubes. The vials were slowly frozen using a Mr. Frosty freezing container placed into a -80ºC freezer and transferred after 24hrs into liquid nitrogen.

3.4 Virus

3.4.1 Reverse genetics viruses

Experiments were performed using reverse genetics equine influenza viruses (EIVs), which include two H3N8 EIVs: A/equine/South Africa/2003 and A/equine/Ohio/2003, as well as various reassortant and mutagenized viruses using one or the other background. A full summary of the viruses used in this work can be found below in table 3.6

Table 3.6: List of viruses used

Virus	Background	Abbreviation
A/equine/Ohio/1/2003	A/equine/Ohio/1/2003	O/2003
A/equine/South Africa/2003	A/equine/South Africa/2003	SA/2003
A/equine/Ohio/1/2003-SA/2003-segment 1 (PB2)	A/equine/Ohio/1/2003	SA1
A/equine/Ohio/1/2003-SA/2003-segment 2 (PB1)	A/equine/Ohio/1/2003	SA2
A/equine/Ohio/1/2003-SA/2003-segment 3 (PA)	A/equine/Ohio/1/2003	SA3
A/equine/Ohio/1/2003-SA/2003-segment 4 (HA)	A/equine/Ohio/1/2003	SA4
A/equine/Ohio/1/2003-SA/2003-segment 5 (NP)	A/equine/Ohio/1/2003	SA5
A/equine/Ohio/1/2003-SA/2003-segment 6 (NA)	A/equine/Ohio/1/2003	SA6
A/equine/Ohio/1/2003-SA/2003-segment 7 (M)	A/equine/Ohio/1/2003	SA7
A/equine/Ohio/1/2003-SA/2003-segment 8 (NS)	A/equine/Ohio/1/2003	SA8
A/equine/South Africa/2003-O/2003-segment 1 (PB2)	A/equine/South Africa/2003	O1
A/equine/South Africa/2003-O/2003-segment 2 (PB1)	A/equine/South Africa/2003	O2
A/equine/South Africa/2003-O/2003-segment 3 (PA)	A/equine/South Africa/2003	O3
A/equine/South Africa/2003-O/2003-segment 4 (HA)	A/equine/South Africa/2003	O4

A/equine/South Africa/2003-O/2003-segment 5 (NP)	A/equine/South Africa/2003	O5
A/equine/South Africa/2003-O/2003-segment 6 (NA)	A/equine/South Africa/2003	O6
A/equine/South Africa/2003-O/2003-segment 7 (M)	A/equine/South Africa/2003	O7
A/equine/South Africa/2003-O/2003-segment 8 (NS)	A/equine/South Africa/2003	O8
A/equine/Ohio/1/2003-PB2 I212V	A/equine/Ohio/1/2003	PB2 212V
A/equine/Ohio/1/2003-PB2 I731V	A/equine/Ohio/1/2003	PB2 731V
A/equine/Ohio/1/2003-PB2 I212V, I731V	A/equine/Ohio/1/2003	PB2 212V+731V
A/equine/Ohio/1/2003-PB2 601C,700C,762T	A/equine/Ohio/1/2003	PB2 3’
A/equine/Ohio/1/2003-PB2 171T, 387T	A/equine/Ohio/1/2003	PB2 5’
A/equine/Ohio/1/2003-PB2 171T, 387T, 601C, 700C, 762T	A/equine/Ohio/1/2003	PB2SYN
A/equine/Ohio/1/2003-HA Q236P	A/equine/Ohio/1/2003	HA236P
A/equine/Ohio/1/2003-HA 992G, 1175A, 1340A	A/equine/Ohio/1/2003	HASYN
A/equine/Ohio/1/2003-PB2 601C, 700C	A/equine/Ohio/1/2003	PB2 601+700
A/equine/Ohio/1/2003-PB2 601C, 762T	A/equine/Ohio/1/2003	PB2 601+762
A/equine/Ohio/1/2003-	A/equine/Ohio/1/2003	PB2 700+762

PB2 700C, 762T		
A/equine/South Africa/2003-O/2003-segments 1,4, and 6 (PB2, HA, and NA)	A/equine/South Africa/2003	O146
A/equine/South Africa/2003-HA 236Q, NA271E, PB2 601T, 700T, 762C	A/equine/South Africa/2003	SA Mini

3.4.2 Creating virus stocks

All viral stocks used for experimental infections were grown to Passage 2 (P2). P0 rescue stocks were used to infect overconfluent MDCK cells in T75 flasks to produce a P1 viral stock. To reduce defective particles, P0 stocks were titrated by plaque assay and between 10-100PFU in 3mL of infectious media were added per flask, which amounts to an approximate MOI of $1x10^{-5}$. 2-3 days post-infection, when there was 80% cytopathic effect (CPE) visible in the monolayer, the virus was collected and centrifuged at 300xg and the supernatant was aliquoted and stored at -80^{o}C. This process was repeated for the P1 stock, in order to expand it to the P2 working stock. The viral titers were determined for each viral stock as described in section 3.4.3.

3.4.3 Viral titer determination

Viral concentrations were determined by plaque assay in MDCK cells. In order to determine the viral titer, the stock was titrated in 12-well plates of MDCK cells seeded at $2.5x10^{5}$ per well the day prior to the titration. The virus solution was diluted in 96-well plates containing Temin's Modified Eagle Medium 2X (MEM, Gibco) and 1µg/mL TPCK (Sigma Aldrich, T1426), by adding 30µL of solution to 270µL on the first row of the plate, and then doing 10-fold dilutions down the plate (while switching tips on each row) to reach a lower dilution of 10^{-4}. 100µL of each dilution were added to PBS washed confluent MDCK cells in the 12-well plate, allowed to absorb for 1 hour at 37^{o}C and 5% CO_2, and then washed again to remove the inoculum. Each well was then filled with 1mL of overlay media

(50%(v/v) MEM 2X, 50% (v/v) avicel, and 1µg/mL TPCK) and allowed to incubate 37ºC and 5%CO_2 for 3 days. 3 days post infection, the overlay was removed, the cells were washed twice with PBS, and then fixed using 4% Formalin for 10 minutes. The formalin was removed, and the fixed cells were then transferred to the general laboratory where they were washed again with PBS. The PBS was then replaced with Coomassie blue staining (0.1% Coomassie Brilliant Blue R-250, 45% Methanol, 10% acetic acid), and left for 10 minutes to stain. The Coomassie was removed and washed 3 times with water, and then left to dry before counting the plaques.

3.4.4 Experimental infections

E. Derm cells seeded at $1x10^5$ cells per well were added to 12-well plates with or without 13mm coverslips and were infected at MOI 0.1 with the indicated viruses and placed at 37ºC with 5% CO_2. After 1hr incubation, the inoculum was removed, the wells were rinsed with PBS, and then 1mL of maintenance media was added. 24 hours post infection, the media was removed, the wells were washed again, and the coverslips were fixed with 4% formalin for 30 minutes at room temperature. Each experimental infection was conducted three times independently in addition to the three technical repetitions that were done for every infection. Viral titers, as calculated by plaque assay, in MDCK cells were used to calculate the infection MOI used for the E. Derm cell infections.

3.4.5 Viral protein staining for confocal microscopy

Coverslips were washed in PBS and allowed to rock at 100rpm for 10 minutes, and then blocked in 10% normal goat serum (NGS) in PBS at room temperature for an hour. Coverslips were then incubated with anti-HA mouse monoclonal (13g10), anti-NA mouse monoclonal (5.12E), or anti-NP rabbit polyclonal overnight at 4ºC. Coverslips were then washed 3 times and incubated with PBS to rock at 100rpm for 10 minutes, and then incubated with the appropriate secondary antibody. The coverslips were then washed again 4 times with PBS and dried before mounting onto slides with Vector laboratories VECTASHIELD® HardSet mounting media with DAPI and/or Phalloidin-TRITC.

3.4.6 Lectin staining, neuraminidase, and oseltamivir treatment

The three lectins that have been used are all from Vector Laboratories: *Sambucus Nigra* Lectin (SNA) conjugated to Cy5 fluorophore, which preferentially binds sialic acid attached to a terminal galactose in an α-2,6 linkage, a biotinylated *Maackia Amurensis* Lectin II (MAL II), which preferentially binds sialic acid attached to a terminal galactose in an α-2,3 linkage, and Fluorescein labelled *Erythrina Cristagalli* Lectin which binds specifically to the terminal galactose exposed following sialic acid cleavage (Iglesias et al., 1982). Type II neuraminidase from *Vibrio Cholerae* (Sigma-Aldrich #N6514) was used for the neuraminidase experiments, which preferentially hydrolyzes α-2,3 linked sialic acids, but will also hydrolyze α-2,6.

For neuraminidase treatment of cells, 1 mU was added to E. Derm cells in 1mL of maintenance media post absorption and cells were incubated at 37^{o}C, 5% CO_2 for 22 hours.
For Oseltamivir treatment, 100nM of oseltamivir was added to E. Derm cells immediately post absorption and incubated at 37^{o}C, 5% CO_2 for 22 hours.

For the lectin staining, cells were fixed in 80% acetone at room temperature for 10 minutes and stored in PBS at 4^{o}C before staining. They were then blocked in 10% NGS for 30 minutes and 250µL of biotinylated MALII was added to each coverslip. For the SNA coverslips, 250µL of 10mM HEPES was added. The coverslips were then rocked at 100rpm at room temperature for 30 minutes and the liquid was removed and washed 3 times with TPBS (0.05% Tween 20). After the 3rd wash TPBS was left on the coverslips and rocked for 10 minutes. The TPBS was then removed and replaced with 250µL of SNA-Cy5 to SNA coverslips and Avidin-D Fluorescein to MALII coverslips and left at room temperature for one hour. After removing the lectin stains, the washing steps were repeated, and the coverslips were dried and mounted using the Vectashield mounting media.

3.4.7 Neuraminidase activity assay (MUNANA)

Input virus was diluted to 2x10^{4} pfu in MES (2-(N-morpholino)ethanesulfonic acid) Buffer (32.5mM MES (Sigma, 71119-23-8) + 4mM $CaCl_2$+dH_2O, pH to 6.5 with NaOH). Viruses were then incubated with 100µM of MUNANA substrate (Sigma,

M8639) in triplicate for one hour at 37°C in a plate reader, including a negative control sample (MES buffer + MUNANA). The samples were excited in the 355 nanometer (nm) wavelength and emission was read from 460nm wavelength every minute for one hour. The output relative fluorescence units (RFU) data were graphed using GraphPad and a linear regression was fit to each sample. The slope of this line represents catalysis of MUNANA substrate, which is directly related to NA activity. Each NA activity value was normalized to input genome copies, which were calculated by qPCR of M-segments (Section 3.6).

3.4.8 Hemagglutination assay

A Hemagglutination assay is a method used to determine the endpoint dilution of virus HA required to hemagglutinate red blood cells or bind it together in a closely associated lattice. The HA titer readout is directly correlated to HA quantity and virus titer. To determine the HA titer, we used chicken blood (ENVIGO, S.B-0008) that was washed with 45mL of cold PBS and centrifuged at 600g for 5 minutes at 4°C three successive times. After removing the supernatant following the third wash, we diluted the blood cell pellet in PBS to a final concentration of $4x10^7$ cells per mL. In a 96-well V bottom plate, we added 50µL of cold PBS to columns 2-12 and 100µL of virus to column 1 and 100µL of PBS to well H1 (negative control). 50µL was transferred across the plate to make two-fold dilutions, and then 50µL of chicken blood was added to each well. Three plates were prepared in the same fashion and incubated at 4°C, 37°C or room temperature for 30 minutes.

3.4.9 Grid preparation for Cryo-EM

Quantifoil R 2/2 100 holey carbon film grids: Au 200 mesh (Q2515) were first sterilized in 70% ethanol and then placed in 32mm dishes with an embedded 13mm coverslip (Greiner). 250µL of 10% laminin diluted in calcium and magnesium free PBS (CMF-PBS, Gibco) was added to the grid and the dishes stored at 37°C at 5% CO_2 overnight. After incubation, the grids were then washed with 500µL of PBS 4 times, and then a cell suspension of 8×10^4 E. Derm cells was added to the grid and topped up with maintenance media and allowed to incubate for 24 hours. The E. Derm cells were then infected as described above at MOI 1 and plunge frozen 16-24 hours post-infection, as described below in section 3.4.10.

3.4.10 Vitrification and storage of EM grids

Infected EM grids were vitrified in liquid ethane using either a EM GP2 automatic plunge freezer (Leica) or Vitrobot (FEI, ThermoFisher). The vitrification process starts when the liquid ethane dish is slowly brought down to temperature by pouring liquid nitrogen into the outer container, and then ethane gas is added into the inner container until the temperature is low enough for the phase transition. The liquid nitrogen cooled liquid ethane is then placed in the plunge freezer. The grid, held in inverted tweezers, is taken out of the 32mm dish and the inverted tweezers are inserted into the plunge freezer. 20nm colloidal gold bead suspension (Sigma-Aldrich) used for fiducials is added to the grid in a 1/3 dilution in dH_2O. The plunge freezer then blots the grid, and then inserts the grid into the liquid ethane, where it is then transferred over to a grid box for storage. For long term storage, each grid box was numbered and placed into a liquid nitrogen storage dewar.

3.5 Imaging and analysis

In order to characterize virus populations, we needed to utilize microscopy, however the traditional lateral resolution limit of light microscopy, 250nm, prohibits high precision measurement of spherical and bacilliform IAV (Witte et al., 2018). Therefore, we used a combination of super-resolution light microscopy for characterization of populations of filamentous viruses, and electron microscopy for a characterization of budding sites.

3.5.1 Confocal microscopy of infected E. Derm Cells

Confocal microscopy was conducted on a laser scanning microscope: Zeiss LSM 880 with Airyscan. A 63x oil immersion objective with a N.A. of 1.40 was used for all confocal studies. In addition, an Airyscan detector, which together with the GaAsP detector, improves the signal-to-noise ratio (SNR) as well as the resolution, was used. Post-acquisition processing was completed using the Airyscan processing package in Zeiss Zen Blue. Image processing was done using ImageJ (Schneider et al., 2012).

3.5.2 Immunofluorescence image processing

Image processing was done using ImageJ. In order to maintain consistency, windows/levels were not adjusted in the software package, as the equipment configuration at the microscope was kept constant for all experiments. Measurements were conducted manually using the metadata available and the measurement tool of ImageJ. The process by which particle length was determined required a selection of particles that were determined to be not clustered. This was accomplished using a combination of default thresholding and particle analysis. The particle analysis set-up required the selection of the following options in set measurements: Feret's diameter, shape descriptors, and area. The 2D area threshold that was applied was between 0.0144 microns squared and 2 microns squared, which encompassed the smallest and largest IAV 2D projection areas for the camera and microscope used.

Finally, the resulting measurements obtained by the particle analysis plugin in ImageJ were filtered by diameter whereby any particles with diameters greater than 200nm were discarded. The resulting virus particles lengths were then calculated using the Feret's diameter. The Feret's diameter is the longest distance across an object between two parallel tangential lines, which is typically described as the caliper length. In order to calculate the resolution we used an estimate of the optical resolution as described using Abbe's equation multiplied by the resolution improvement of the Airyscan detector (calculated below). Given the resolution limit, IAV particle categories were divided as follows: 100nm-250nm spherical, 250nm-500nm bacilliform, >500nm filamentous.

$$\mathrm{D}_{\mathrm{airyscan}} = \frac{\mathrm{D}}{1.7} = \frac{.61\lambda}{\mathrm{NA}} = \frac{.61 \times 488\mathrm{nm}}{1.41 \times 1.7} = 124\mathrm{nm}$$

$$\lambda = \mathrm{wavelength}$$

$$\mathrm{D} = \mathrm{Resolution}$$

$$\mathrm{NA} = \mathrm{Numerical\ aperture}$$

Given that filamentous influenza virions are usually categorized as viruses longer than 250nm, it was important to create a threshold which limits the inclusion of bacilliform and spherical viruses, while capturing as many of the filamentous

viruses as possible. Due to the resolution limit of 124 nm, there would be overlap with the other virus morphologies for any virus less than 500nm.

3.5.3 Electron microscopy

Cryogenic electron microscopy was conducted at the Scottish Centre for Macromolecular Imaging using a JEOL Cryo-ARM 300 transmission electron microscope coupled with a Direct Electron 64 8K camera. A simple schematic showing the main parts of a TEM setup are shown below in figure 3.1.

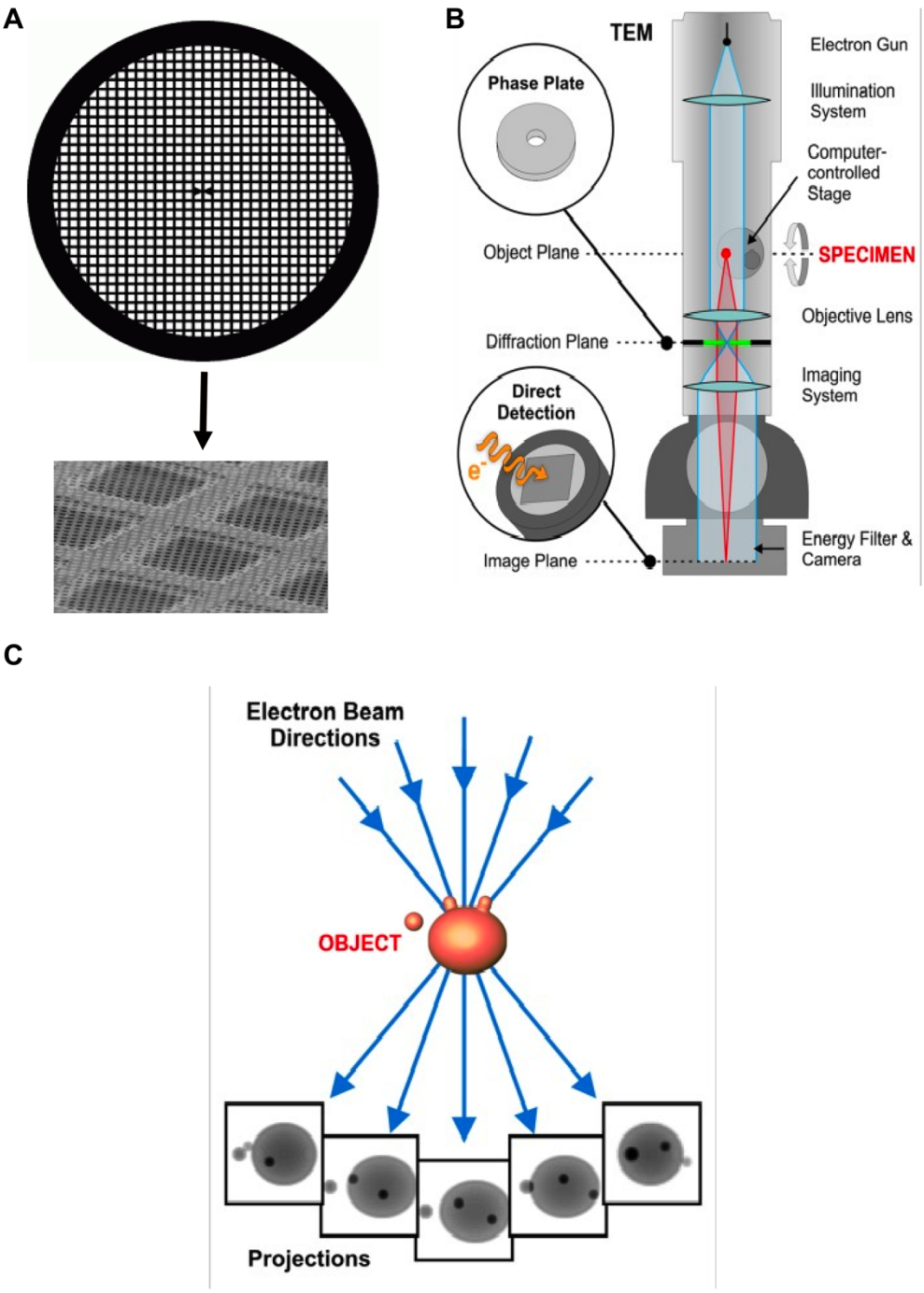

Figure 3.1 Schematic of Cryo-EM setup
A) A depiction of the carbon coated gold grids on which E. Derm cells were grown and infected. The arrow shows the holey carbon film on a magnified grid square. B) A schematic representation of the parts of a transmission electron microscope. The grid shown in (A) would be placed in the area labelled specimen and rotated around an axis in order to generate a series of titled images. C) A representation of a tilt series, with the differences in electron beam directions generating different transmission micrographs. Image adapted from Lucic et al., 2013.

This setup was used throughout its installation, however the collection procedures and the availability of the energy filter and a dose-symmetric tilting scheme varied between sessions.

3.5.4 Cryo-EM data collection

Tilt series were collected at 50,000x dose-symmetrically from -45^{o} to 45^{o} with 2^{o} of tilt per image.

3.5.5 Tomogram processing

Raw frame outputs were concatenated using a script written by James Streetley and dose-weighted using the imod function alignframes. Tilt series alignment, tomogram generation, and non-linear anisotropic diffusion-based denoising was done using IMOD (Kremer et al., 1996). Segmentation was done using a combination of 3dmod (an IMOD package) and Amira (Thermo Fisher Scientific). In the event of a poor fitting alignment, tomograms were generated using EMAN2 (Tang et al., 2007).

3.5.6 Tomogram segmentation

Tomogram segmentation was done using Amira (2020.3.1, ThermoFisher Scientific). All regions were segmented manually using the brush tool, interpolation, and constrained smoothing.

3.6 Quantitative PCR

3.6.1 Viral RNA extraction

Viral RNA (vRNA) was extracted from 140µL of either viral stock or supernatant of infected cells using QIAamp® Viral RNA Mini kit (Qiagen). 560µL of AVL buffer and 5.6µg of carrier RNA was added to each aliquot in a safety cabinet and mixed, and then incubated for 10 minutes before completing the inactivation using 560µL of 100% ethanol. Samples were then loaded into RNeasy spin columns, where the RNA was bound to the membrane using an initial spin of 10,000 RPM for 30 seconds and then washed with 700µL AW1 buffer twice, and 500µL AW2 twice. The RNA was eluted by adding 60µL of AVE buffer to the membrane, incubating for a minute, and then centrifuging at 6,000 RPM for 30 seconds.

3.6.2 Retro-transcription

Reverse transcription of IAV vRNA was done using a combination of Uni12 and Uni12g primers (Table 3.2, Hoffmann et al., 2001), 2µL of RNA, Superscript IV reverse transcriptase (Invitrogen), and the manufacturers protocol.

Table 3.7: Cycling parameters

Steps	Temperature	Duration
Annealing	65^{o}C	5 minutes
Incubation	0^{o}C (ice)	1 minute
First strand cDNA synthesis	55^{ø}C	10 minutes
Inactivation	80^{o}C	10 minutes

3.6.3 Standard quantification

The standards used for quantitative PCR were O/2003 plasmids of the segment amplified. To quantify the amount of plasmid in solution accurately, each plasmid stock was diluted 1/10 and analyzed using a Qubit® dsDNA HS assay (Life Technologies) and a Qubit® Fluorometer. The given concentration of the solution was then turned into copy number by calculating the molecular weight of the plasmid using the available sequence of the insert, as well the number of bases and GC content of the vector. The calculations were done both manually and checked using the ThermoFisher DNA Copy Number calculator. After quantification, each standard was then diluted 1:10 up to 10 times to determine the standard curve and limit of detection for the assay.

3.6.4 Quantitative PCR

Quantitative PCR (qPCR) was done on an Applied Biosciences 7500 qPCR machine, and the plate was setup using the following conditions: 5 standards with 3 technical repeats for each segment M, NP, and PB2 (15 wells x 3= 45 wells) and 3 technical repeats per sample (each done for M, NP, and PB2). This corresponded to 4 samples (x3 technical repeats + x3 segments=36 wells), and additional 3 non-template control wells per segment. Each well contained 10µL of TaqMan master mix II (Applied Biosystems, ThermoFisher), 1µL of 10µM

Forward/Reverse Primer mix (Table 3.2), 1µL of 10µM Probe (Table 3.2), 5.5µL of nuclease-free water, and 2.5µL of template.

Table 3.8: qPCR cycling parameters

Steps	**Temperature**	**Duration**
Holding stage	95°C	10 minutes
Denaturation	95°C	15 seconds
Annealing/Extension	60°C	45 seconds
Denaturation and Annealing/Extension Repeated for 40 cycles		

3.7 Graphing and statistical analysis

All statistical analyses were done using GraphPad Prism 9.2.0. Significance was calculated as stated in the result for each specific type of data.

4 Identification of novel determinants of EIV morphology

Influenza A viruses (IAVs) infect a wide array of species including but not limited to wild and domestic birds, humans, pigs, dogs, and horses (Parrish et al., 2015). Due to this broad host range, IAVs are forced to adapt to a complex series of inter and intra-host environments (Ma et al., 2016, Imai et al., 2012). One mechanism that allows IAVs to adapt to environmental challenges involves that natural pleiomorphy of the virus; IAV virions typically produce a wide distribution of viral particles ranging from 120nm spheres to 20μm filaments (Chu et al., 1949, Badham and Rossman, 2016, Dadonaite et al., 2016). It has been shown that this natural pleiomorphy is advantageous in response to changes in the intercellular environment (Vahey and Fletcher, 2019c, Vahey and Fletcher, 2019a), as certain morphologies are favored when faced with particular challenges. As a result, it is now known that morphological distribution is both genetically encoded by the virus and modulated by the growth environment (Vahey and Fletcher, 2019c). Therefore, it is imperative that to understand the role of IAV structure it is necessary to understand the genetic underpinnings of phenotypic variation.

To understand the role that multiple genomic segments could have on IAV pleiomorphy, we used an EIV as a model system. As mentioned previously, EIVs are an ideal model system to study IAV structure as they are largely filamentous and some of the genetic determinants of EIV morphology have already been identified. Specifically, we used two highly similar EIVs: O/2003 and SA/2003, which despite their genetic similarity display different morphological phenotypes. To this end, we combined *in vitro* experimental infections, confocal microscopy, reverse genetics, and site-directed mutagenesis to unravel the source of this dissimilarity. By experimentally infecting E. Derm cells with these viruses, we were able to characterize differences between multiple reassortant and mutant viruses and identify mutations responsible for observable changes in the filamentous subpopulation.

4.1 O/2003 produces a largely bacilliform population, while SA/2003 produces filaments

To begin investigating the differences between these two EIVs, we first needed to understand what genetic differences there were between SA/2003 and O/2003. As seen below in Table 4.1, O/2003 and SA/2003 are genetically similar viruses that have a total of thirty-two nucleotide differences, nine of which result in an amino acid change. Of the nine amino acid changes, none of them result in a change to the three segment seven proteins (Wise et al., 2012) and therefore there is no observed amino acid changes in the M1 protein.

Table 4.1 A summary of all nucleotide substitutions between SA/2003 and O/2003.

Segment	Nucleotide	O/2003	SA/2003
1(PB2)	171 387 601 634 700 762 2191	T T T A(212Ile) T C A(731Ile)	C C C G(212Val) C T G(731Val)
2(PB1)	300 624 1191 1393 1785 1812 1818 1956	T A T T G G T G	C G C C T A C A
3(PA)	1044 1164 1480 1491 1590 2007	T G G(494Val) G C C	C A A(494Ile) A T A
4(HA)	709 992 1175 1340	A(236Gln) A G G	C(236Pro) G A A
5(NP)	641	G(214Arg)	A(214(Lys)

6(NA)	812	A(271Glu)	G(271Gly)
7(M)	480	G	A
8(NS)	64 354 386 466	T(22Phe) A T(129Ile) G(156Val)	G(22Val) G C(129Thr) A(156Ile)

In order to compare these two viruses, we needed to first generate a method to accurately quantify virus particles. Using super-resolution confocal microscopy coupled with a semi-automated pipeline for analyzing particle lengths, we developed a tool that allowed us to characterize the particle lengths for a whole virus population. A diagram showing the major steps of this pipeline is shown below in figure 4.1. Before inputting the images into the semi-automated pipeline, the channel corresponding to the HA staining was subtracted from the channel containing the actin (phalloidin) staining to remove cell debris. In figure 4.1A, this confocal micrograph is automatically thresholded and then filtered by 2D projection area to give a selection of viral particles. These viral particles are then filtered by width to remove any clustered viruses, and then measured by Feret's diameter (Figure 4.2B). The final lengths can then be analyzed as a full distribution as shown below in figure 4.2C, and compared between viruses.

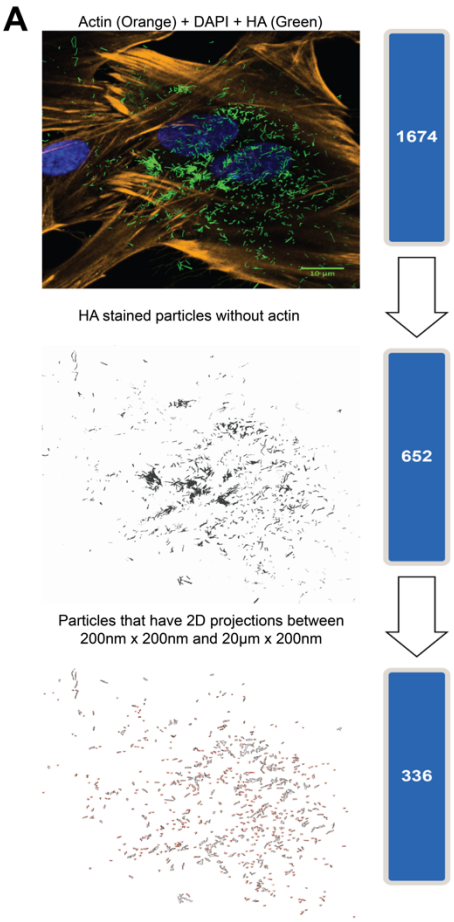

B

Width	Height	Major	Minor	Feret	Threshold Width	Threshold Length	Final Length
0.128	0.17	0.164	0.098	0.19	0.098	0.19	2.975
0.298	0.213	0.316	0.167	0.366	0.167	0.366	2.723
0.213	0.17	0.206	0.145	0.229	0.145	0.229	2.025
0.085	0.085	0.101	0.069	0.12	0.069	0.12	1.771
0.17	0.17	0.177	0.078	0.213	0.078	0.213	1.752
0.043	0.043	0.048	0.048	0.06	0.043	0.06	1.713
0.085	0.085	0.096	0.096	0.12	0.085	0.12	1.713
0.085	0.043	0.096	0.048	0.095	0.043	0.095	1.568
0.043	0.043	0.048	0.048	0.06	0.043	0.06	1.513
0.085	0.043	0.096	0.048	0.095	0.043	0.095	1.309
0.128	0.043	0.144	0.048	0.134	0.043	0.134	1.226

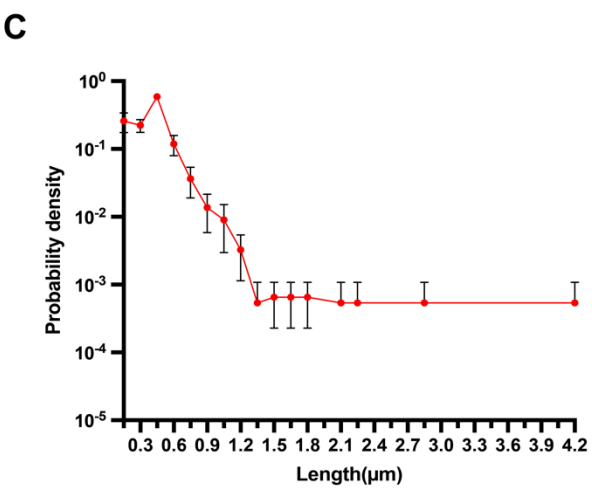

Figure 4.1 Summary of semi-automated measurement pipeline
A) A step-by-step depiction of the automated portion of the pipeline. The top image represents the raw micrograph with the actin in orange, DAPI in blue, HA-stained particles in green, and the number is the total number of particles in the image. The second image is after default thresholding, the remaining particles is halved. The image is then processed through a size filter corresponding to the dimensions and 2D projection area maximum of a filamentous particle (20µm by 200nm), this leaves around 300 particles. B) The results from the pipeline are then brought into Microsoft Excel where they are further thresholded by width (minimum of ellipse/rectangular fit). The headings of the table correspond to the Width and Height of the rectangular fit, the major and minor axis of the fit ellipse, and the Feret's diameter. Threshold width is the minimum width in both fits, and the threshold and final lengths are the lengths of the particle if it passes the width filter. The output length for every virus is the maximum Feret's diameter (caliper length). C) These processed lengths comprise the HA positive objects which are now considered to be viral lengths, and they can now be analyzed. The mean lengths and standard deviation from this image are now shown as probability density curve, which is a histogram but the bins of the histogram are shown as parts of the total population. The bin width is 150nm.

Given the small number of genetic differences between the two viruses, the expectation was that confocal microscopy of infected cells would show little to no differences between the virus morphological populations. However as seen below

in Figure 4.2A, SA/2003 and O/2003 infected E. Derm cells at 24hpi produce viruses that display noticeable differences in the proportion of filamentous particles, as stained by HA. However, when we look at the population as seen in Figure 4.2B there appears to be little difference in the distribution of viral particle lengths apart from a subpopulation of a viruses that are greater than 500nm in length. Despite the appearance of similar distributions, the distributions of SA/2003 and O/2003 are statistically significant ($p<.0001$) as measured by a Kolmogorov-Smirnov test. This difference is likely due to the increased proportion of filaments. In order to test this subpopulation, we looked at the percentage of viruses greater than 500nm, which we class as filaments (Chapter 3.5.2). When looking at this filamentous subpopulation and measuring the proportion present in each virus we find that there is a significant difference ($P=.0097$) between SA/2003 and O/2003 (Figure 4.2C). This difference in the filamentous subset cannot be due to an amino acid change in the matrix protein given that there are no differences between the viruses (Table 4.1), so it must be due to another factor.

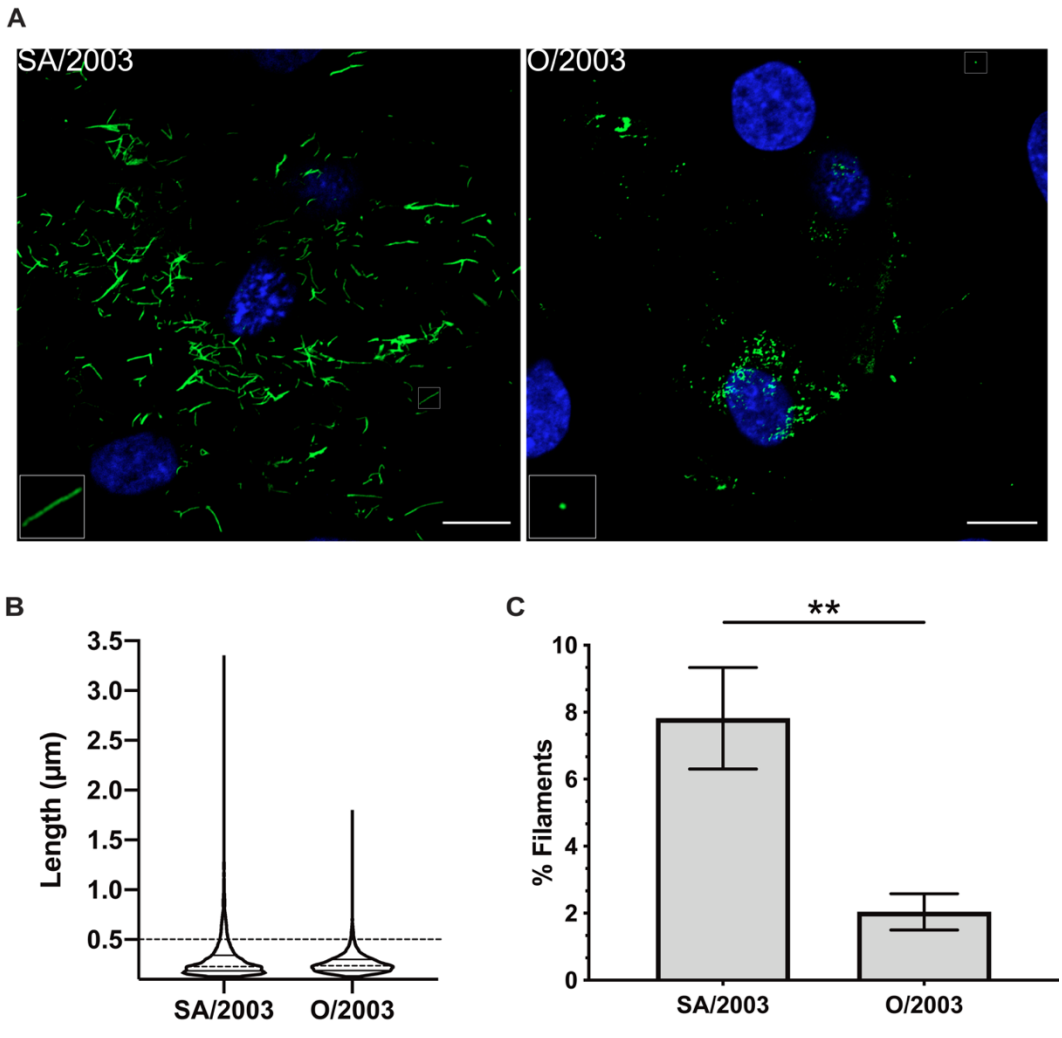

Figure 4.2 Structural characterization of SA/2003 and O/2003.
(A) Super-resolution confocal micrographs of representative SA/2003 and O/2003 infections using an anti-HA antibody. HA in green and nuclei stained with DAPI in blue, scale bar represents 10μm. 3X inset of the region of interest shown in the bottom-left hand corner. (B) Distribution of viral lengths shown as a violin plot. Measurements are representative of three separate infections. Dotted line denotes the 500nm filamentous threshold. Significance measured using a Kolmogorov-Smirnov test(C) Bar graph of the percentage of viral particles that exceed 500nm (filaments). Error bars represent standard error of the mean (SEM), and significance level is ** $p<0.01$ as measured by a Mann-Whitney test.

4.2 Single O/2003 genomic segments are not sufficient to drive a spherical phenotype

To determine which mutation or combination of mutations were responsible for a change in phenotype, we first needed to identify which segments had a role in morphology. In order to interrogate this difference, we had to look at both the gain-of-function (filamentous morphology) and the loss-of-function (spherical morphology). It was hypothesized that the same mutations responsible for the filamentous morphology when reverted would generate spheres.

To identify if any single O/2003 segment could make SA/2003 spherical, we generated isogenic reassortant viruses in a SA/2003 background that contained single segments from O/2003 as shown in Figure 4.3A. Measurements of the percentage of filaments for this set of reassortant viruses shows (Figure 4.3B) that no single O/2003 segment restores O/2003 spherical morphology in a SA/2003 backbone. In fact, out of the eight reassortant viruses tested only one of the viruses has a lower average filament percentage than SA/2003 (SA/2003_ONS), although this is not significantly different. The representative super resolution confocal micrographs shown below in Figure 4.3C support the quantitation, as filamentous viruses are present in every image.

The inability of a single O/2003 segment to revert the phenotype suggests that the hypothesis was incorrect, and multiple segments of O/2003 would be required to revert the morphology. Therefore, to determine the segment(s) responsible for the filamentous morphology it would be necessary to repeat the genetic reassortment in an O/2003 background.

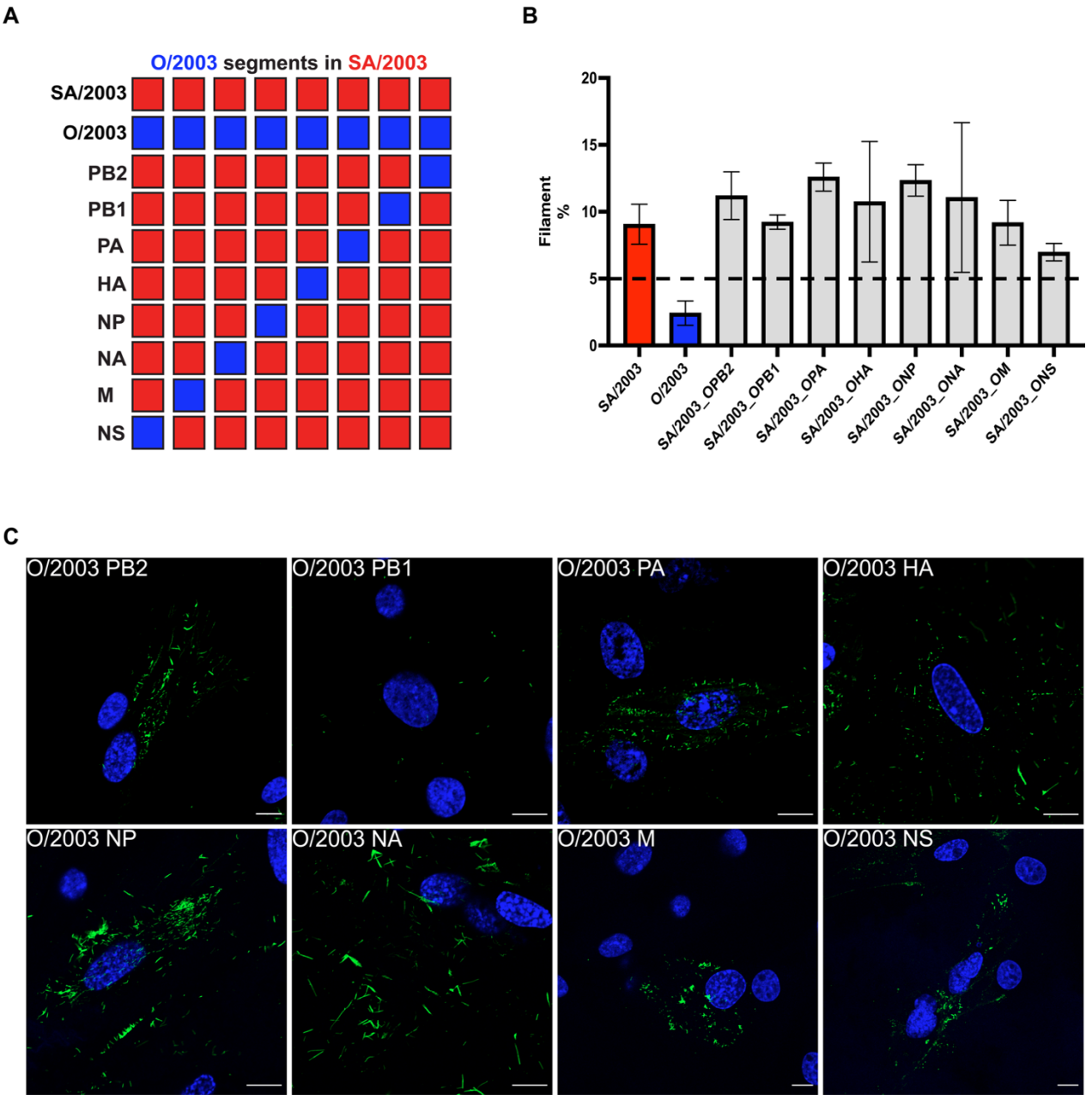

Figure 4.3 Single segment reassortant viruses in a SA/2003 background
(A) Schematic representation of the set of reassortant viruses generated with single O/2003 segments in a SA/2003 background (B) Bar graph showing the filament percentage for each reassortant virus, as well as the two wild-type viruses. There are significant differences as measured by a Mann-Whitney test between some of the reassortant viruses and O/2003. The P values for each is as follows: SA/2003 (p=0.033), SA/2003_OPB2 (p=0.0483), SA/2003_OPB1 (p=0.0233), SA/2003_OPA (p=0.0181), SA/2003_OHA (p=0.260), SA/2003_ONP (p=0.026), SA/2003_ONA (p=0.267), SA/2003_OM (p=0.0422), SA/2003_ONS (p=0.0491). There are no significant differences between the reassortants and SA/2003. (C) Representative super-resolution confocal micrographs showing E. Derm cells infected at 24hpi with each of the single segment reassortant viruses. HA in green and nuclei stained with DAPI in blue. Scale bar represents 10μm.

4.3 SA/2003 genomic segments 1, 4, or 6 are morphological determinants in an O/2003 background

Given that O/2003 segments were insufficient to alter morphology in a SA/2003 background, we needed to identify the effect of SA/2003 segments in the context of O/2003. To interrogate which SA/2003 segments were involved in morphology, we generated a reciprocal set of isogenic viruses that contained a single segment from SA/2003 in an O/2003 background (Figure 4.4A). The percentage of filaments for each reassortant virus varied and only three segments had SA/2003-like filament percentage (Figure 4.4B). To classify the viral populations as filamentous or spherical, we needed to develop a metric that we could apply for all viruses. We therefore decided to divide the viruses into two classes, one bounded by the upper limit of length of O/2003 and one bounded by the lower limit of length of SA/2003. This threshold corresponds roughly to a filament percentage of 5%. Using this metric, we observed that segments 1, 4, or 6 of SA/2003 in an O/2003 background were sufficient to exceed the 5% threshold, and we therefore consider them filamentous (Figure 4.4C).

The presence of three segments that individually impact filament percentage, suggests that we have at least three separate mutations that are morphological determinants. To determine the nature of these mutations it was necessary to locate the specific sites on each segment responsible.

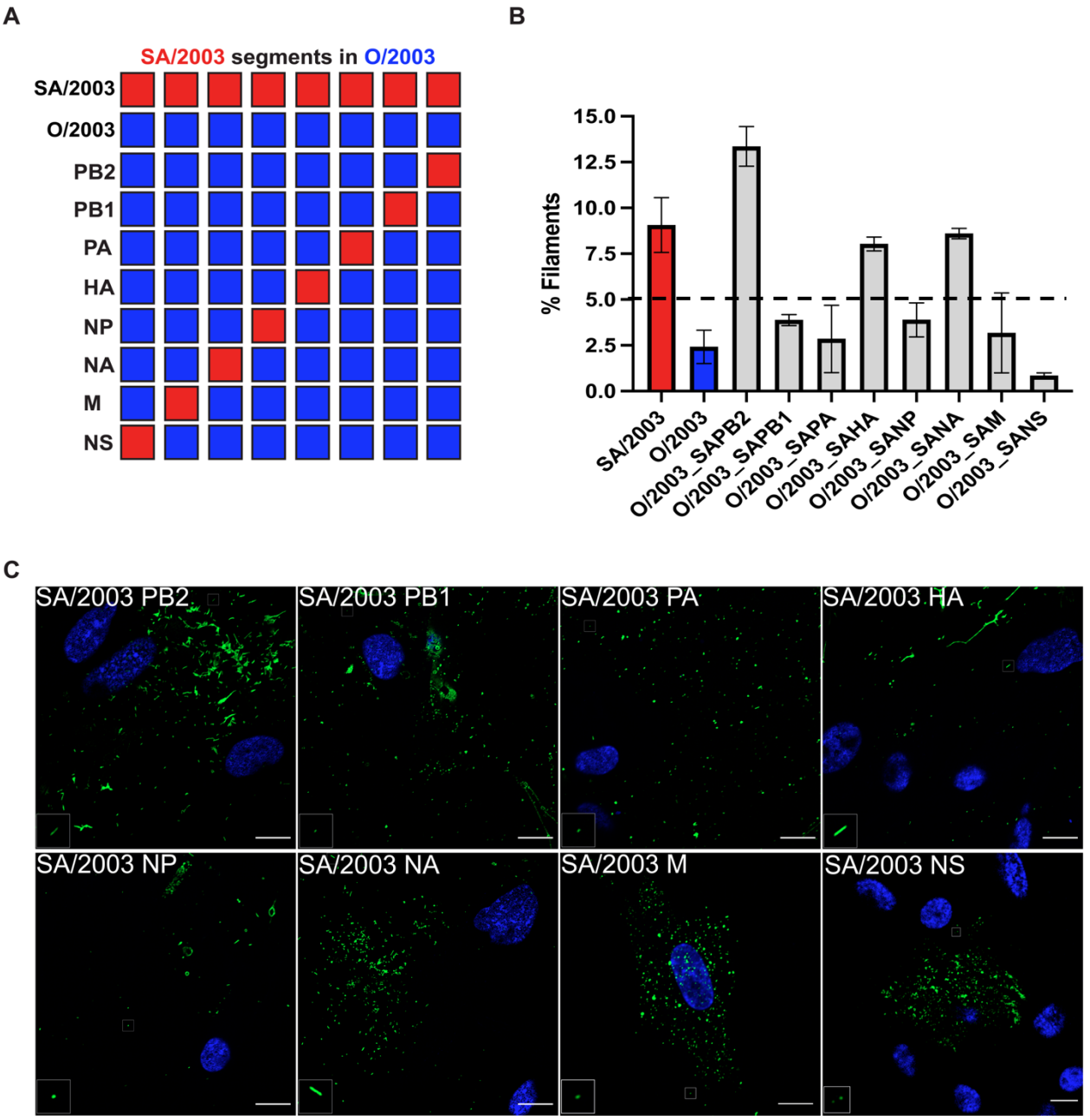

Figure 4.4 Single segment reassortant viruses in a O/2003 background
(A) Schematic representation of the set of reassortant viruses generated with single SA/2003 segments in a O/2003 background (B) Bar graph showing the filament percentage for each reassortant virus, as well as the two wild-type viruses. There are three viruses that are significantly different from O/2003: O/2003_SAPB2 (p=0.0163), O/2003_SAHA (p=0.0294), and O/2003_SANA (p=0.0229), as measured by a unpaired Student's t test.(C) Representative super-resolution confocal micrographs showing E. Derm cells infected with each of the single segment reassortant viruses for 24hpi. HA in green and nuclei stained with DAPI in blue. Scale bar represents 10μm.

4.4 A single mutation in segment 4 is sufficient to make O/2003 filamentous

The results from the reassortant virus infections point to three genomic segments that are involved in morphology: segments 1, 4, and 6, which encode the proteins PB2, HA, and NA. While there is only a single non-synonymous mutation on segment 6 that results in a change morphology, segments 1 and 4 both contain multiple nucleotide differences between O/2003 and SA/2003. In segment 4, there are four nucleotide substitutions and one of them results in a change to the protein (Table 4.1). We therefore sought to understand which of these nucleotide changes was responsible, and if it had to do with a change in the HA protein. To accomplish this, we produced two isogenic viruses in an O/2003 background, one which contained the only non-synonymous change in HA Q236P, from the nucleotide change A812G and one that contained the synonymous substitutions (A992G, G1175A, G1340A) in segment 4 (Figure 4.5A). E. Derm cells were experimentally infected with these mutant viruses, fixed, and imaged under the same conditions as the previous experiments. Figure 4.5B shows that A812G is sufficient to confer filamentous morphology to O/2003 and replicate the filament percentage of the whole SA/2003 segment 4. The synonymous changes on segment 4 on the other hand, did not replicate the filament percentage of SA/2003 or appear to have any effect at all. This is clearly observed in the representative images in Figure 4.5C, as the Q236P (A812G) mutation in an O/2003 background is highly filamentous, while the synonymous changes by themselves result in no observable change. Since changes to the structural proteins have been implicated in morphology, it is not entirely surprising that we have identified two morphological determinants in HA (Q236P) and NA (E271G). However, there are no reported instances of segment 1 being involved in morphology.

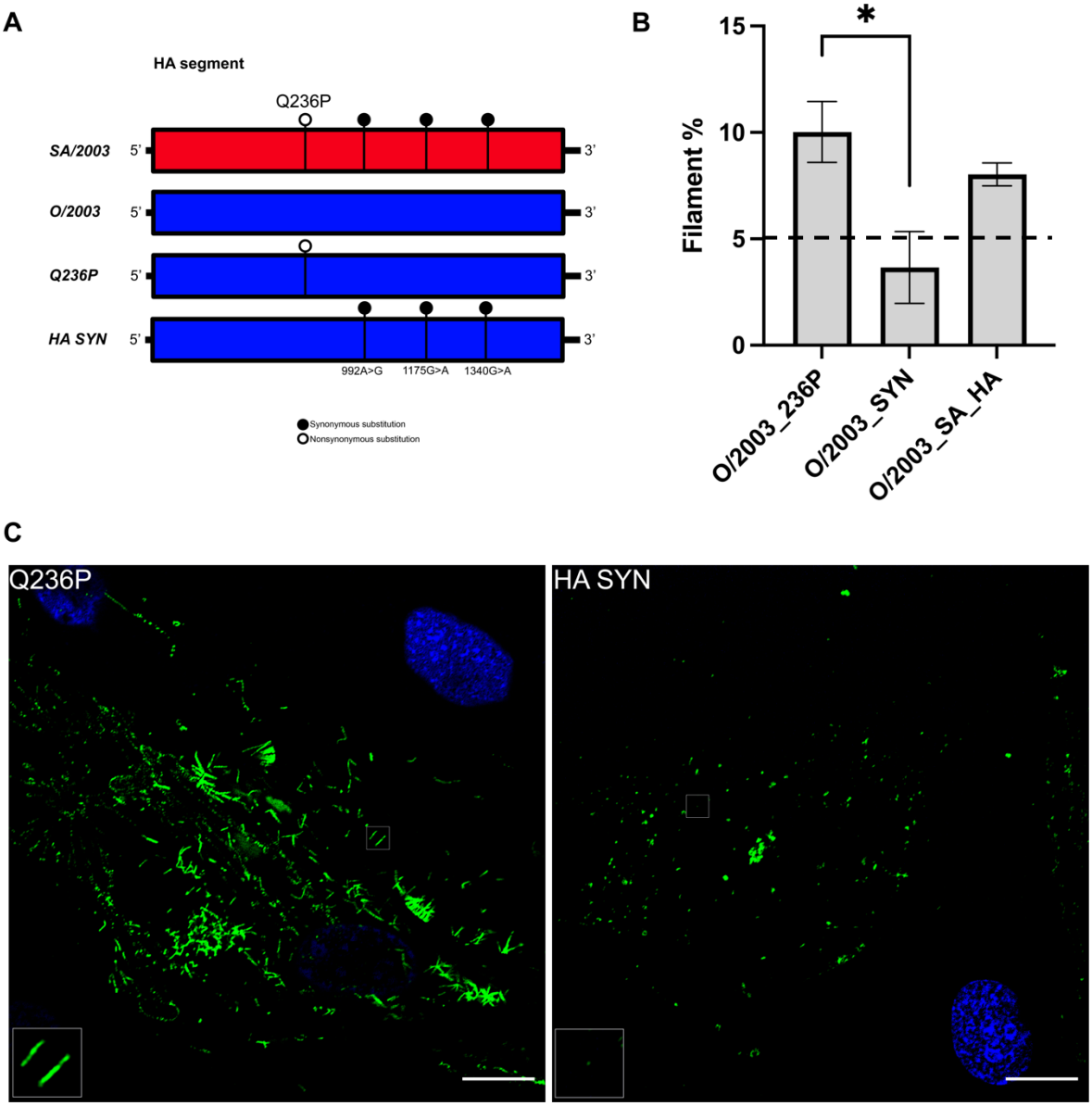

Figure 4.5 Identification of morphological determinant in segment 4
(A) Schematic representation of the viruses shown below relative to the wild-types. Open circle lollipops represent non-synonymous mutations and filled in circles represent synonymous mutations. (B) Bar graph of the percentage of filamentous viral particles, error bars represent SEM and significance was measured using an unpaired t-test. (C) Representative super-resolution confocal micrographs of the Q236P (A812G) mutation in an O/2003 background (Q236P) and the combined synonymous mutations (HA SYN) of SA/2003 in an O/2003 background using an anti-HA antibody. HA in green and nuclei stained with DAPI in blue, scale bar represents 10μm. 3X inset of the region of interest shown in the bottom-left hand corner.

4.5 Three synonymous changes in segment 1 confer O/2003 filamentous morphology

There are five synonymous and two nonsynonymous changes that differentiate segment 1 (PB2) of O/2003 from SA/2003 (Table 4.1). To unravel the mutation(s) responsible for the observed morphological change associated with segment 1, we again generated isogenic viruses carrying different combinations of mutations in an O/2003 background (Figure 4.6A). We began the search for the morphological determinant by constructing a O/2003 background virus with the two non-synonymous changes in segment 1. To this end, we generated three viruses: one that contained both I212V (A634G) and I731V (A2191G) mutations, one that contained only I212V (A634G), and one that contained only I731V (A2191G) (Figure 4.6A). We hypothesized that one of these non-synonymous changes would be required to change the virion structure, but to our surprise we observed that neither of these amino acid changes in PB2, either on their own or in conjunction, generated filaments in an O/2003 background (Figure 4.6B). However, despite the lack of visible filaments, I212V (A634G) produces a high percentage of filamentous virions when quantified using the image analysis pipeline (Figure 4.6C). Given that this morphological determinant straddles the filamentous threshold, we investigated further to see if it was the major morphological determinant that was responsible for the filamentous morphology of SA/2003 segment 1. Although I212V (A634G) represents a minor morphological determinant, when compared to the effect of the entire segment 1 (Figure 4.6D), we found that the mutation did not recapitulate the distribution as measured by a Kolmogorov-Smirnov test.

In order to identify the major determinants of filamentous morphology, we needed to now interrogate synonymous changes. To isolate the morphological determinant residing in the synonymous changes in segment 1, we decided on a top-down approach, meaning we first showed that a PB2SYN construct which had all the silent mutations in segment 1 (T171C, T387C, T601C, T700C, C762T) was filamentous (Figure 4.6B and 4.6C). Once we showed that the synonymous changes in PB2 were responsible for the change we then devised a strategy to map the mutations responsible. To identify the morphological determinant, we separated the five mutations in PB2SYN into two separate constructs: 3’ (T601C,

T700C,C762T) and 5’ (T171C, T387C). Looking at the 3’ and 5’ constructs in Figure 4.6B, we found that the 3’ construct was filamentous and similarly in Figure 4.6C, we found that it closely matched the filament percentage observed in PB2SYN. Thus, we had identified that the major morphological determinant was due to one of the three nucleotide changes in 3’. To further isolate the major morphological determinant, we continued the top-down approach and produced three further constructs that contain the exhaustive set of two mutations combinations in 3’. None of these three constructs produced filaments in an O/2003 background, thus identifying all three nucleotide mutations as the major morphological determinant in segment 1 (Figure 4.6C).

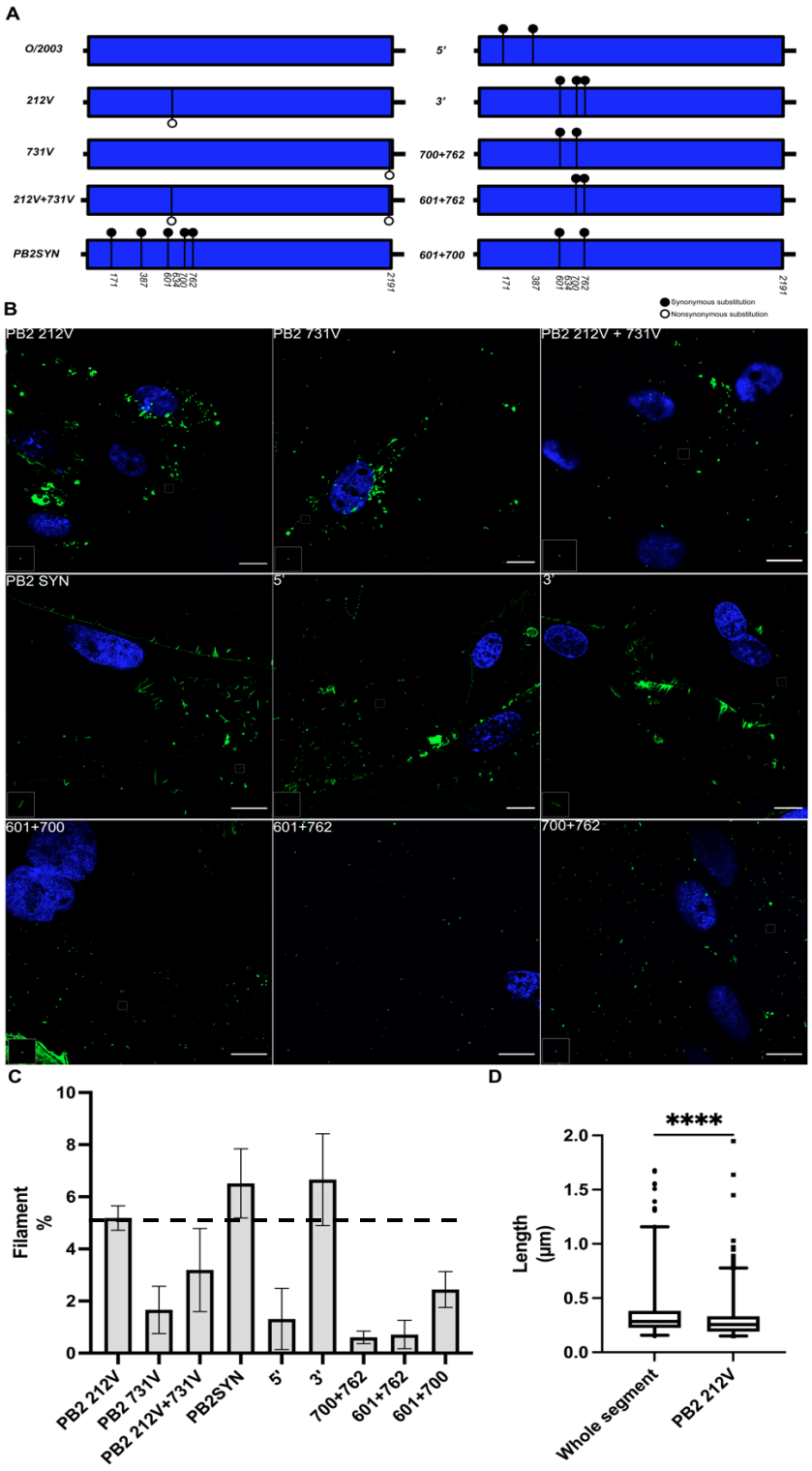

Figure 4.6 Identification of morphological determinants in segment 1. (A) Schematic representation of the segment 1 constructs compared to wild-type. (B) Representative super-resolution confocal microscopy of the segment 1 mutants using an anti-HA antibody, scale bar represents 10µm. 3X inset of the region of interest shown in the bottom-left hand corner. (C) Bar graph of the percentage of filamentous viral particles, error bars represent SEM. (D) Box and whisker plot showing the morphological distributions of the whole SA/2003 segment 1 in an O/2003 background compared to the I212V mutation in an O/2003 background.

4.6 All mutations identified to be morphological determinants in an O/2003 background must be reverted to make SA/2003 spherical

Identification of the major morphological determinants that when added to an O/2003 background made O/2003 filamentous brought forward the question of genetic redundancy with respect to morphology. If morphology is an important aspect of viral fitness *in vivo*, and multiple single mutations in an O/2003 background are sufficient to restore filamentous morphology, it can be hypothesized that O/2003 needs multiple genetic determinants working in concert to block filament formation (Figure 4.4). In order to determine whether multiple mutations are required to make SA/2003 spherical, we reverted the major morphological determinants we identified in segments 1, 4, and 6. This resultant virus in an SA/2003 background (SA/2003-O146), contains the three O/2003-like nucleotide mutations in PB2 3'(C601T, C700T, T762C), the nucleotide mutation in HA 709A (Pro236Gln), and the nucleotide mutation in NA 812A (Gly271Glu). As shown in the representative images in Figure 4.7A, these mutations added into an SA/2003 are sufficient to make SA/2003 spherical. This is shown again in Figure 4.7B, where both O/2003 and SA/2003-O146 have similar average filament percentages. Lastly, to determine whether the major determinants of morphology identified in an O/2003 background were strong enough to recapitulate the morphological distribution of O/2003 wild-type when reverted in a SA/2003 background, we produced a probability density plot of both viruses and SA/2003 wild-type. As shown in Figure 4.7C, the distribution of viral particle lengths between O/2003 and SA/2003-O146 are nearly identical until the probability density reaches 10^{-3}. At that point of divergence, the O146 mutations added actually lower the number of viruses in each histogram bin that contains higher length particles. So, it is clear that the mutations from these three segments when in O/2003-like positions are sufficient for reverting the phenotype in SA/2003.

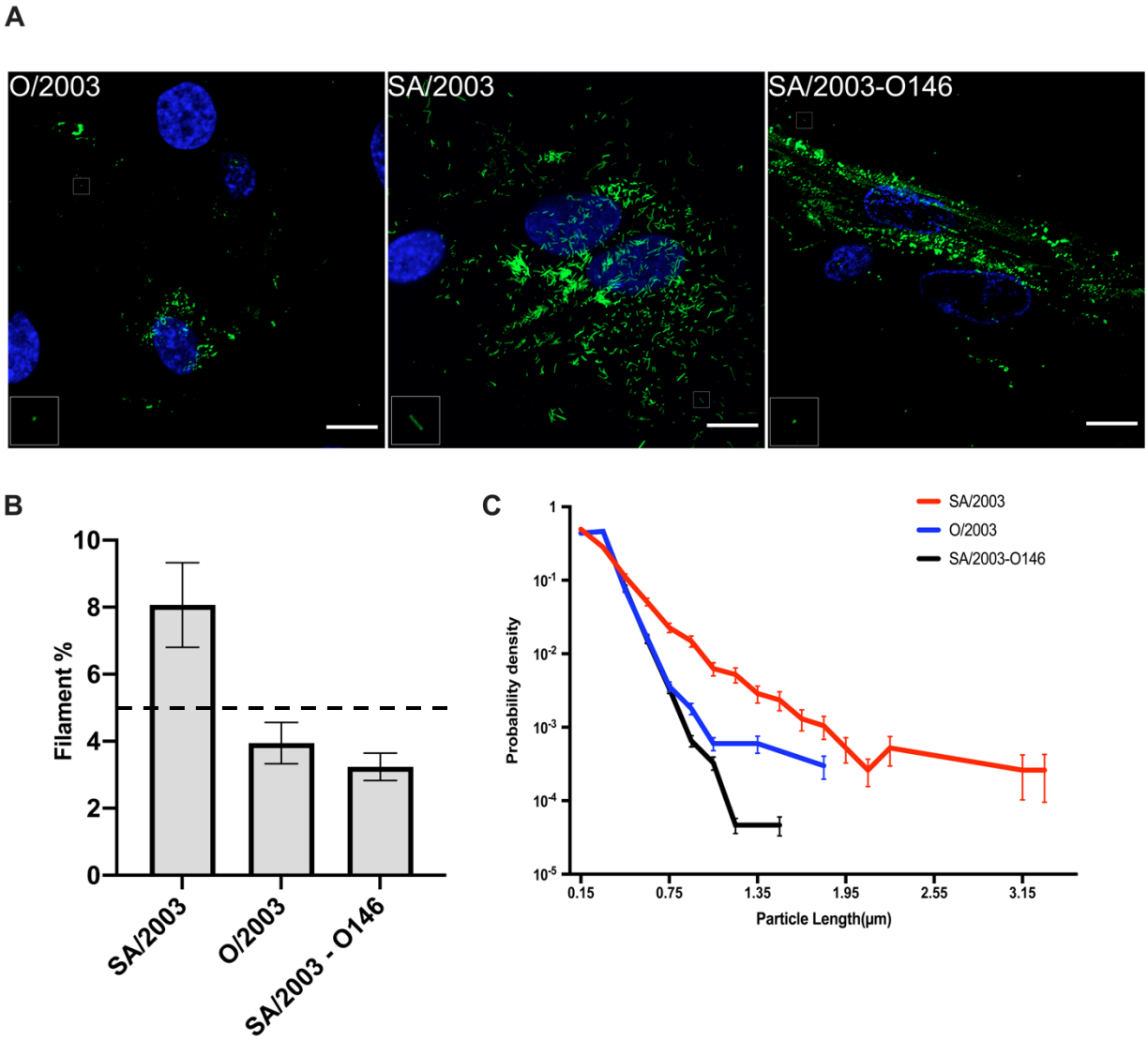

Figure 4.7 Three segments are required to make SA/2003 spherical
(A) Representative super-resolution confocal micrographs of both wild-type viruses and SA/2003 with three mutagenized genomic segments using an anti-HA antibody, scale bar represents 10µm. 3X inset of the region of interest shown in the bottom-left hand corner. (B) Bar graph of the percentage of filamentous viral particles, error bars represent SEM. (C) A probability density graph showing a binned distribution of each of the viruses imaged in (A) bin size 150nm, error bars represent SEM.

4.7 Genetic determinants of EIV morphology are redundant and highly conserved

The relationship between viral fitness and morphology is unknown, but the short evolutionary history of EIV and well mapped morphological determinants, allow us to look at this. By measuring the frequency of genetic determinants of filamentous morphology across this evolutionary history and applying our results which show that filaments are a dominant phenotype, we can predict the phenotype of a virus based on its genotype. To conclude if the mutations that we have identified between SA/2003 and O/2003 are present in other H3N8 EIVs, we aligned, with the help of Jordan Bone who generated the alignment and the raw figure, all available H3N8 EIV complete sequences available (N=138) at both known genetic determinant sites in M1: N85S, N231D (Elton et al., 2013), as well as the novel sites detected in this study (Figure 4.8). Of note, we observed that O/2003 has unique amino acid positions in both HA and NA, as well as a unique combination of PB2 nucleotide changes. Since no other EIV presents with these mutations either individually or in combination, it is clear that the sites described in this study represent a unique mechanism by which O/2003 overcomes the genetic redundancy that ensures structural variation. In contrast, these data show that since the majority of viruses are predicted to be filamentous and these mutations are highly conserved, spherical morphology must come with a fitness cost.

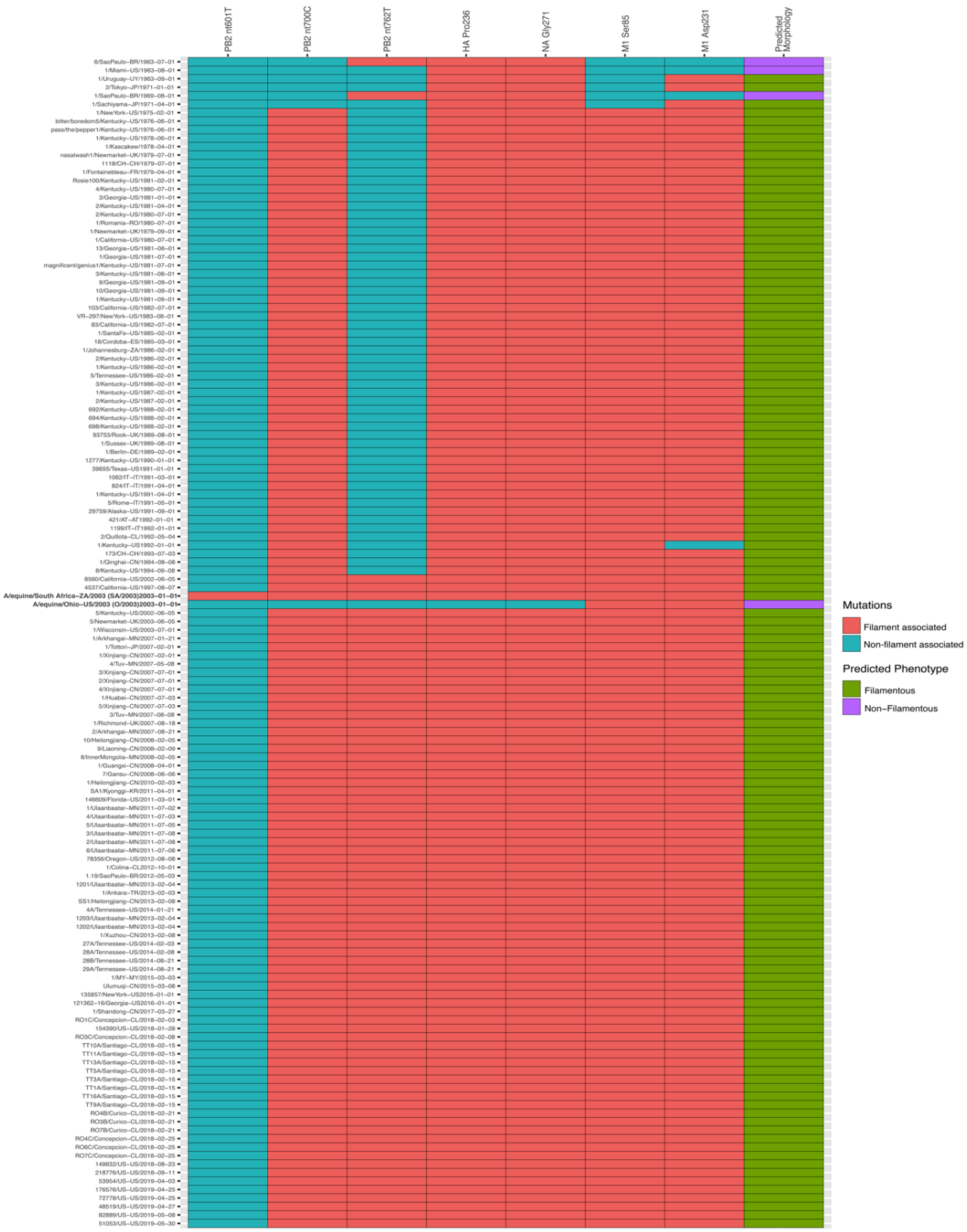

Figure 4.8 O/2003 has multiple unique mutations
Representation of all 138 complete H3N8 EIV sequences at important sites for IAV morphology: amino acid positions 85 and 231 in M1, 236 in HA, and 271 in NA, along with nucleotide positions 601, 700, and 762 in PB2. Given the positions at each of these sites, a predicted phenotype was generated.

4.8 Discussion

Multiple determinants of IAV morphology that result in a change from a spherical to a pleiomorphic population have been identified and mapped to either interactions with the M1 protein or specific residues on the M1 protein (Elleman and Barclay, 2004, Bourmakina and Garcia-Sastre, 2003). What remains unclear however, is the role of other genomic segments in the modulation of morphological distributions. While it has been shown that cell-type and growth environment have a role in temporarily changing the variation in particle size (Vahey and Fletcher, 2019c, Al-Mubarak et al., 2015), it appears that IAV has a genetically encoded heterogeneity that ensures that progeny of individual virions are as variable as the original viral population (Vahey and Fletcher, 2019c). Despite the importance of genetic determinants to the structural characteristics of IAV, as well as the functional importance of morphological distributions, there is little to no information on the role of non-matrix protein interacting factors on morphology.

In order to understand the role of non-matrix protein interacting factors on morphology, we used two H3N8 IAVs that have nearly identical M segments but are structurally distinct. Although both viruses would be predicted to be filamentous according to the sequence of segment 7 (Seladi-Schulman et al., 2013), and both produce some level of viruses greater than 500nm, there is a consistent and quantifiable difference between SA/2003 and O/2003 (Figure 4.2). Given this difference, we sought to develop a strategy to discriminate between complex morphological distributions and identify the determinants of morphology.

Despite the observable differences between SA/2003 and O/2003 in Figure 4.2, it became clear that a qualitative approach was insufficient, as the most filamentous virus measured only produced 15% filaments. Marrying the qualitative observations with quantitative analyses allowed us to simplify the complex size distribution into a single metric, particles greater than 500nm, which allowed us in most cases to identify major determinants of morphology. This conclusion provides a way to couple the power and objectivity of quantitation with the clear but subjective observation of a phenotype.

Using this tool, we were able to first discern the segments and then the mutations in SA/2003 that would make O/2003 filamentous. To this end, we identified three segments in SA/2003 that can individually make O/2003 filamentous, while finding no single segment of O/2003 that can make SA/2003 spherical. Interestingly, of the three segments that are sufficient to make O/2003 filamentous none have any direct association with M1 and in fact the mutations in segment 1 do not even result in changes in the PB2 protein it encodes. The two nucleotide changes that result in a change to the proteins HA Q236P and NA E271G result in a change on the distal portions of the respective H3 and N8 structures, while previously observed morphological determinants on the glycoproteins have only been observed in the proximal, cytoplasmic tail regions of the proteins (Jin et al., 1997). Due to location of these amino acid changes, it is unlikely that these nucleotide mutations alter any interaction with the matrix. Thus, this creates opportunities to understand the complex and coordinated process of enveloped virion formation, as it points to presently unknown mechanisms of IAV filament formation. Thus, modulation of the IAV structural population due to single glycoprotein mutations may suggest that glycoprotein mediated interactions during budding may have an effect on shape, and this effect can be influenced by environmental changes (Vahey and Fletcher, 2019a, Vahey and Fletcher, 2019c).

In addition to the non-synonymous determinants, we also identified 3 nucleotide substitutions on segment 1 that significantly alter the filament population. These changes are especially interesting because they represent the first morphological determinant observed on segment 1, as well as the first synonymous change shown to affect IAV structure. This result and its independence from any amino acid change, suggests that RNA-RNA or RNA-protein interactions may have a role to play in IAV morphogenesis. Whether the phenotype observed is due to changes in intracellular environment or changes that are happening in the viral particle itself, it is clear that alterations to the RNA of segment 1 is sufficient to alter morphology.

O/2003, on the other hand is a pleiomorphic virus that produces predominately spherical and bacilliform viruses although past work on IAV and EIV structure would predict a filamentous morphology (Elleman and Barclay, 2004, Elton et al., 2013). Although it is unclear why O/2003 does not produce filamentous viruses, it

is clear that the addition of 5 nucleotide changes from O/2003 are sufficient to stop filament formation in SA/2003. The combined action of these nucleotide changes to alter the morphological distribution of SA/2003 provides insight into the varied and unknown factors that are involved in IAV budding. It also clearly shows that the genetic determinants underpinning virus shape are highly conserved and redundant, highlighting the evolutionary significance of filaments (Figure 4.8). While this work helps us understand the complex nature of IAV filament formation, it clearly highlights the need for further research into the mechanisms underlying these novel determinants.

5 Mechanisms underlying morphological shift

Virus assembly is a highly coordinated process in which all components of a viral particle (proteins and nucleic acids) are directed to specific cellular compartments and arranged to make a viral particle. This chapter aims to understand the role of the mutations of HA, NA, and PB2 in this process. The segments involved in a change in morphology act in different ways, as the changes in segments 4 and 6 alter the amino acid sequence and thus the proteins HA and NA, while the change observed when porting the segment 1 nucleotide changes into an O/2003 background is independent of any changes to the PB2 protein. Therefore, the goal of this chapter is to understand how each of these mutations modulate morphology.

HA and NA have been implicated in morphology before (Jin et al., 1997), however the mutations altered a specific region of the HA and NA cytoplasmic tails. Our mutations that affect HA and NA are present at amino acid positions 236 and 271 in HA and NA respectively, which suggests that neither mutation is located near the cytoplasmic tail or TMD of the protein (Figure 5.1). Given the locations of the amino acid changes, we are looking at a new mechanism underlying the morphological change observed. It has been observed that HA and NA are involved in the ability for the virus to move in directed motion (Vahey and Fletcher, 2019a), and this motility has shown to be dependent on protein distribution (Vahey and Fletcher, 2019a). Likewise, it has been shown that NA inhibition can cause changes in the morphology of the virus particle population (Vahey and Fletcher, 2019b). To this end, we have performed a series of experiments to test whether there is a differential action of HA and NA in our viruses, and whether they respond differently to inhibition. The segment 1 determinant on the other hand, does not result in a change to the protein so it is unclear at which stage in the viral life cycle the segment 1 mutations are acting. While it is known that M1-vRNP interactions can influence particle shape (Liu et al., 2002) and that RNA interactions between segments mediate formation of the 7+1 vRNP formation (Dadonaite et al., 2019, Noda et al., 2006, Noda et al., 2012), it is not known how a synonymous mutation could affect morphology. Here we attempt to address the most likely mechanistic explanations for the change in morphology for the HA, NA, and segment 1 determinants by using a combination of isogenic viruses.

5.1 Spatial location of amino acids involved in morphological change

Before we can delve into the HA and NA mechanism(s) that alter morphology it is important to understand where the residues are on each glycoprotein and whether that region is associated with a known function. As shown below in figure 5.1A, E271G is located on the head domain of the NA protein.

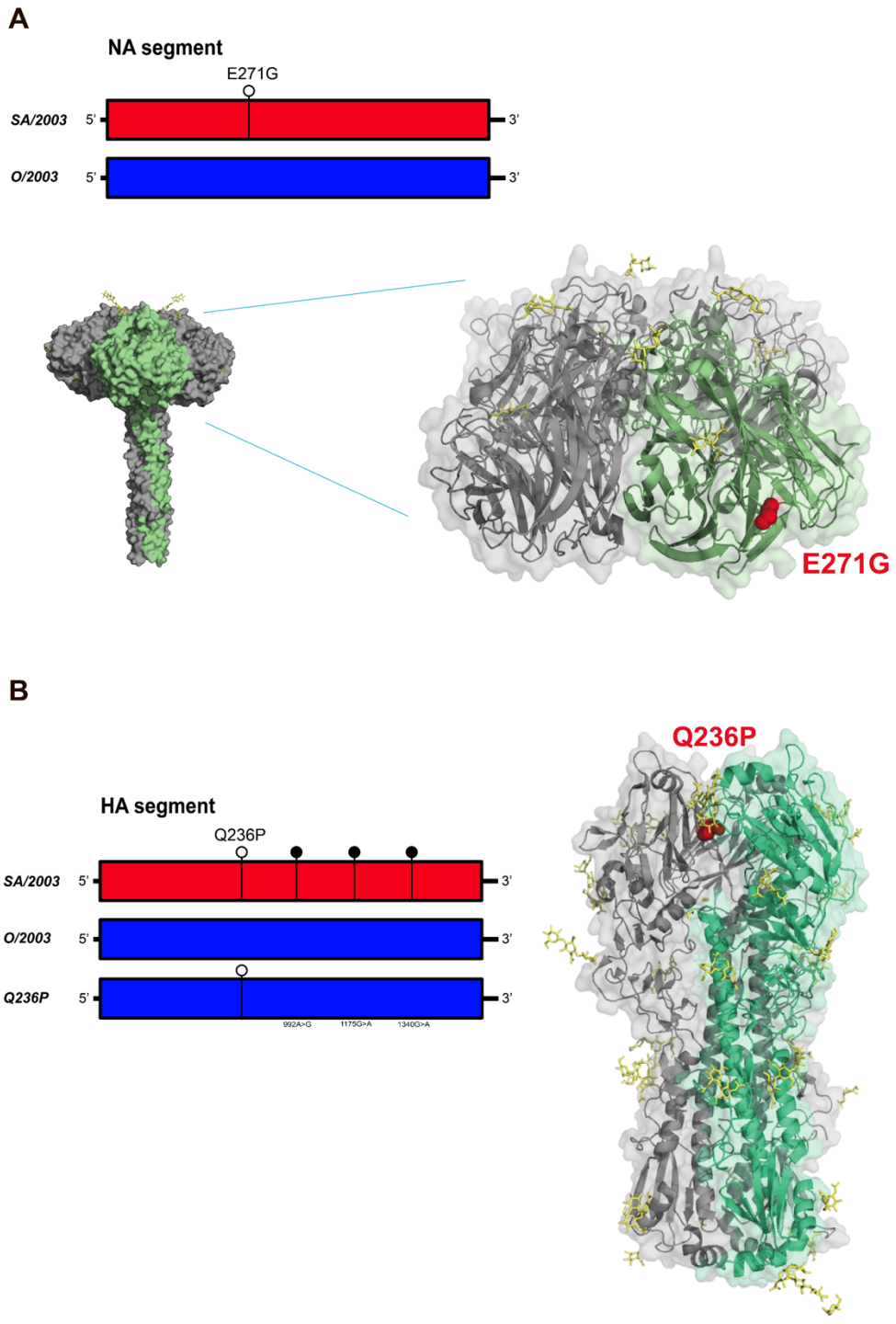

Figure 5.1 The amino acid determinants of morphology are located in the head domains of HA and NA.
A) E271G, the determinant of the change in morphology is the only mutation and only non-synonymous mutation on segment 6. The amino acid change alters a region on the outer shell of the NA head region, as shown on a N8 structure of A/harbor seal/Massachusetts/1/2011 (PDB 4WA5, protein structure visualizations courtesy of Dr. Ed Hutchinson). B) A709C is one of four mutations on segment 4 and the only that results in a non-synonymous change Q236P. The location of the residue on the head domain of a H3 structure from A/equine/Richmond/2007 (PDB 4UO0 is depicted).

The known functional sites of NA are divided into three categories: the inner shell that interacts directly with sialic acids, the outer shell which do not interact directly with the sialic acid but provide a structural framework, and the three arginine residues which interact with the sialic acid substrate carboxylate (McAuley et al., 2019). The E271G mutation is not part of any of these known residues, however its location is adjacent to both the outer shell and inner shell regions. Given that the only available N8 neuraminidase structure is from an unrelated strain of IAV that has 87% amino acid identity with SA/2003, it is difficult to determine whether the position investigated would directly interact with either of these regions. Furthermore, as this position is highly conserved amongst H3N8 EIVs (Figure 4.8) and it has been already shown to affect morphology, there is likely some functional difference associated with this change.

Likewise, the positions in HA are also highly conserved amongst all H3N8 EIVs, although the structure shown above in Figure 5.1B is from a related EIV, A/equine/Richmond/2007(Collins et al., 2014). The receptor binding domain (RBD) of the H3 HA which is located in a cleft that is surrounded by loops and helices at positions 130, 159, 189, 190, 220, 226, and 227 (Matrosovich et al., 1993), is adjacent to position 236 investigated here. While position 236 has not been reported to have an effect on binding, it has been shown previously that mutations in RBD adjacent regions can have significant effects on HA titers (Woodward et al., 2015). Given, that the mutation in HA affects morphology, it is important to identify if this is a secondary effect of a change in activity.

5.2 Removal of sialic acids decreases filament proportion

To determine if the change in morphology is due to differences in HA activity/binding, we first wanted to determine if this change in morphology was due to the presence of differential sialic acid binding during budding. It has been demonstrated that the uneven distribution of glycoproteins can lead to directed motion of IAV filaments (Vahey and Fletcher, 2019a), as well as suggested that virus morphology can be affected by virus-receptor contacts (Guo et al., 2018). Therefore, our hypothesis, as shown below in figure 5.2A, is that a difference in HA binding affinity/avidity would affect the balancing of binding forces, and that imbalance could lead to an elongation of the IAV filament by a mechanism similar to that of directed motion. If for example the morphological determinant HA Q236P modulates morphology by this mechanism, then the removal of sialic acids should disproportionately affect the filamentous population, as the filamentous population will be formed in part through the help of virus-receptor interactions.

To test the role of virus-receptor interactions on morphology, we infected cells on coverslips with SA/2003 and O/2003, and after 2 hours post-inoculation we treated them with bacterial neuraminidase at a concentration of 100mU/mL. At 24 hours post-infection, we fixed and stained these coverslips and measured released virus size using an anti-HA antibody.

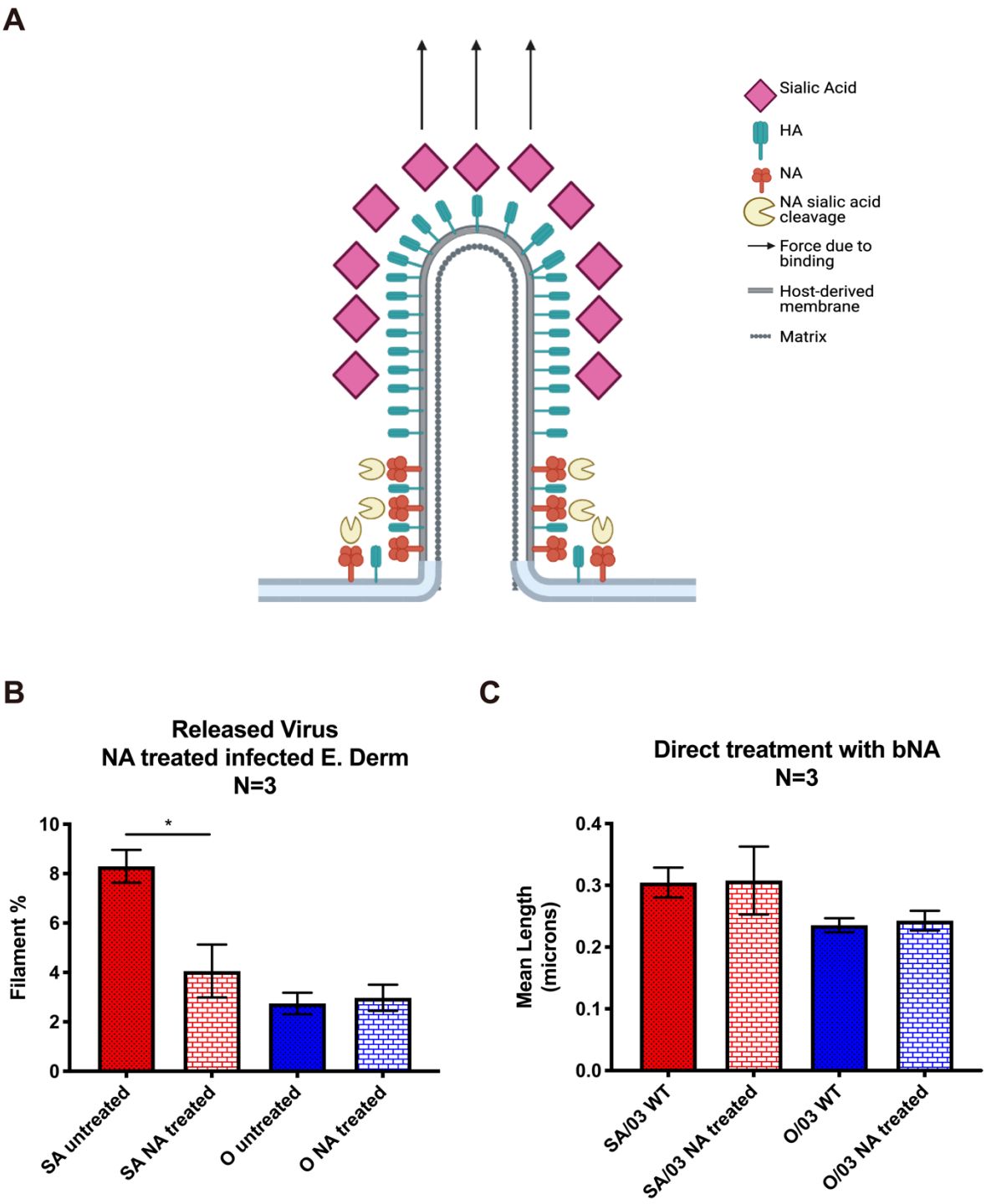

Figure 5.2 HA-Sia binding may affect virus morphology
A) Hypothesized mechanism for filament elongation which involves differences in HA binding affinity/avidity between viruses. P=.048 between SA untreated and SA NA treated as measured by a Kolmogorov-Smirnov test. B) Removal of sialic acids by bacterial neuraminidase (bNA) results in a decrease of filament proportion for SA/2003, with no change for O/2003. C) Direct treatment with bNA has no effect on either viral population.

As shown above in figure 5.2A, the removal of sialic acids by bacterial neuraminidase (bNA) results in a significant difference in the proportion of filaments produced by SA/2003, while not affecting the filament percentage of

O/2003. With regards to the filamentous percentage of O/2003, this is not entirely unexpected as there are very few filaments to begin with, however with SA/2003 this treatment appears to abrogate filament production. This observed change in filament proportion can be ascribed to either a change to the extracellular environment or a direct effect of bNA, however, as shown in figure 5.2C, there is no change in morphology due to direct treatment with bNA. For the direct treatment, we added the same concentration of bNA to viral supernatants from the 24hpi control infection and spun the virus supernatants down onto coverslips. We then measured the virus by anti-HA staining and compared the mean lengths. Thus, the difference in filament proportion must be due to differences in the extracellular environment, as there is no observed difference in the directly treated virus.

In order to determine that the lack of sialic acids is responsible for a change in filament proportion, it is necessary to show that the sialic acids are being removed. To accomplish this, we set up a lectin staining system to verify the sialic acid linkages that are present, and then tested our bacterial neuraminidase at the concentration used in our experiments to see if we were indeed removing the sialic acids. As described in chapter 3.1, we used two lectins (MALII and SNA) to label the sialic acid linkages present in E. Derm cells. As shown below in figure 5.3A, we optimized the lectin staining for MALII and the secondary Avidin D-fluorescein by using three different concentrations of each. MALII preferentially binds α2,3 linked sialic acids, while SNA preferentially binds α2,6 sialic acids. The amount of background for the lectin staining meant that it was preferable to choose a point where there was probably a loss of signal, but a higher signal to noise ratio. To this end, we selected 15µg/mL of avidin D, and 10µg/mL of MALII as our preferred combination of primary and secondary lectin stains. Likewise, for the SNA-cy5 staining in figure 5.3B, we only had access to a conjugated primary lectin rather than a primary and secondary so we only needed to optimize the initial concentration of lectin. Given the staining of the three concentrations (Figure 5.3B), we opted for 10µg/mL of SNA because it was much cleaner than 15µg/mL and had a higher signal than 5µg/mL. The results of figure 5.3A and 5.3B show that this cell line expresses both of the major linkages of sialic acid, as we have positive staining for both lectins, although for the purposes of this study we were solely concerned with the α2,3 linked sialic acids, as it is the primary receptor for H3N8 EIVs (Collins et al., 2014, Shinya et al., 2006). Most importantly, we wanted

to test that introduction of bNA at a concentration of 100mU/mL was sufficient to remove the available sialic acid linkages. As shown below in figure 5.3C, 100mU of bNA removed nearly all the available α2,3 linked sialic acids.

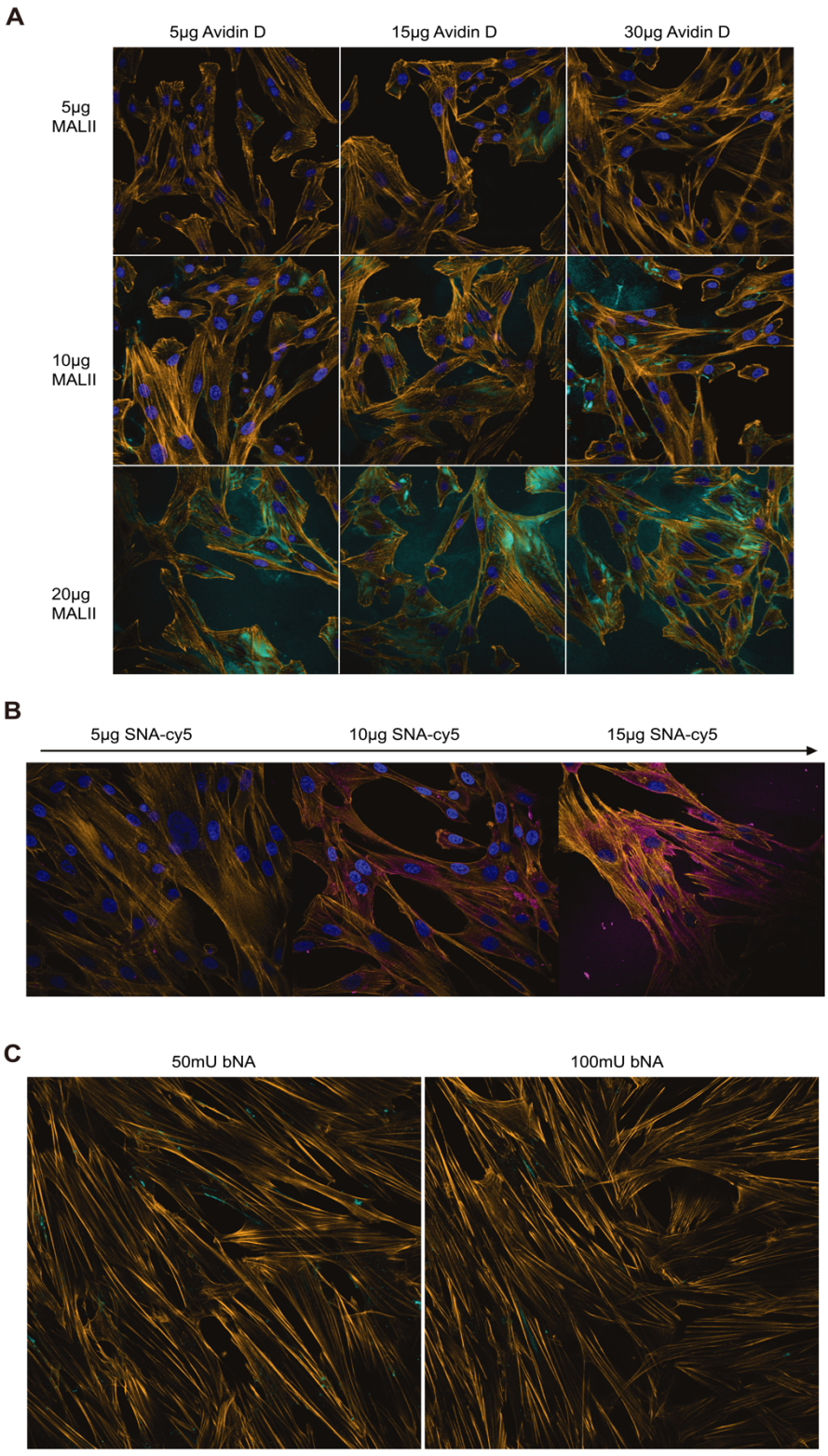

Figure 5.3 Optimization of sialic acid staining
A) Optimization panel with confocal microscopy showing concentrations of MALII and Avidin D shown as µg/mL. Avidin staining shown in cyan, DAPI, and phalloidin stained actin in orange. B) Confocal optimization of SNA-cy5 staining,

concentrations are μg/mL. Actin in orange, nuclei in blue, and SNA staining in magenta. C) Treatment of MALII stained cells with bNA at either 50mU/mL or 100mU/mL. Actin shown in orange, and MALII staining shown in cyan.

5.3 HA titer is independent of morphology and HA position 236

The decrease in proportion of filaments upon bNA treatment suggests that sialic acid interactions play a role in morphogenesis, however it is unclear if this change is due to a difference in HA distribution or HA activity. In order to determine whether or not there was a difference in hemagglutination between the viruses, we tested the HA titers for viruses grown in E. Derm for 24 hours. To interrogate the differences in HA, we titrated the virus in a plaque assay, HA assay, and ran a qPCR for the M segment. The purpose of this was to identify if any of the differences observed were due to difference in particle count (M segment qPCR was a proxy for this), difference in the infectious titer (plaque assay), or a difference in hemagglutination (HA assay). As shown below in figure 5.4, there are no obvious differences between the two viruses with regards to HA titer. In figure 5.4A, a hemagglutination assay was done for both viruses at three different temperatures to control for any unwanted NA binding, and there were no significant differences between the viruses at any temperature tested. In order to normalize to the amount of virus/viral particles added in to the assay, we compared the HA assay results after normalization by both infectious particles (Figure 5.4B) and M segments (5.4C). While again there was no statistically significant difference between the 24 hour timepoint virus (Figure 5.4B, $p=0.30$, and Figure 5.4C, $p=0.40$), there appears to be a trend where O/2003 has a higher HA titer per particle and per infectious unit. Given this trend, it is important to consider the NA activity of either virus, as the proposed mechanism rests on an unbalanced binding force, whereby a decrease or increase in NA activity or distribution can alter the magnitude of the imbalance despite no significant differences identified due to HA.

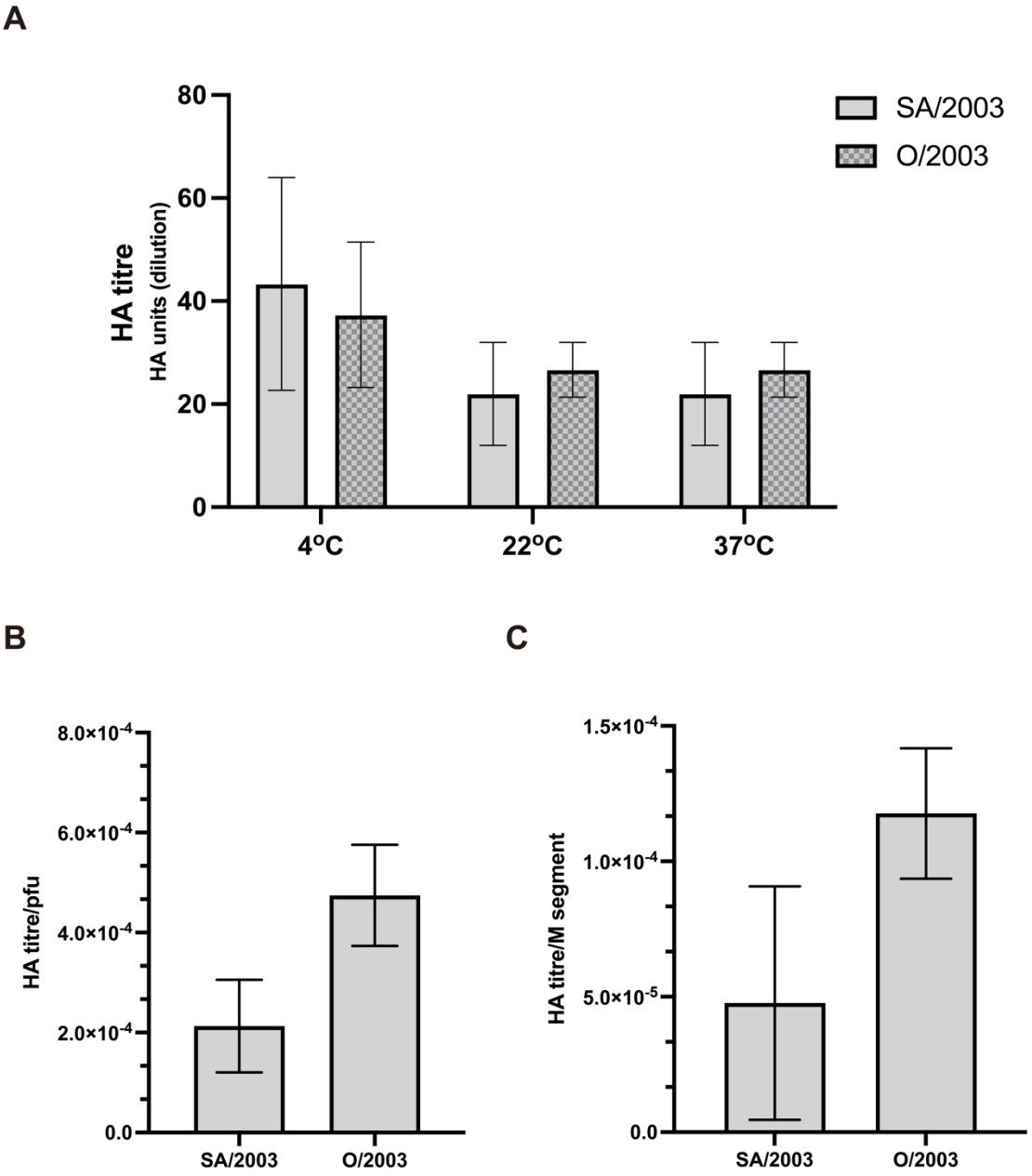

Figure 5.4 There is no significant difference in HA titers between supernatant viruses when normalized to genomes
A) HA titer is unchanged by temperature of incubation. B) O/2003 has a higher average HA titer/PFU than SA/2003 although it is not significantly different, as measured by a Mann-Whitney test p=0.30. C) O/2003 has a higher average HA titer/genome than SA/2003, but again it is not significant.

5.4 NA inhibition has specific effects on attached virus lengths and global effects on released virus lengths

To determine the specific role of HA in morphogenesis, we designed a further experiment where we could test HA dependent elongation in the absence of NA activity through the use of a neuraminidase inhibitor (NAi, oseltamivir). The

hypothesis being that SA/2003 with its unbalanced binding force would continue to elongate if you further abrogated NA function using a NAi, while O/2003 on the other hand should have no difference in attached virus length. Although, O/2003 would have no difference in virus length if there was something else abrogating filament production further complicating the analysis. As shown below in Figure 5.5A, it was observed in both the confocal micrographs and the scanning electron micrographs (SEM) that oseltamivir treatment resulted in elongation of attached viral particles for both viruses. There is an inherent difficulty in quantifying attached filaments, as they are easily mistaken for cellular projections covered in HA. Therefore, in order to quantify the attached filaments we opted for a previously described method that utilizes bNA to release attached filaments (Vahey and Fletcher, 2019b). However, when we attempted to quantify this difference in figure 5.5B using bNA to release the attached viruses, we found a significant difference in the distribution of viral particle lengths for SA/2003 ($p<0.0001$), but no significant difference for O/2003 ($p=0.8450$). The change observed in the SA/2003 population mirrors what was seen in the confocal and SEM images, as there is a decrease in the smaller virus particles attached and an increase in the largest particles, although the shape of the distribution in figure 5.5B also shows a loss of bacilliform particles.

In addition to attached virus particle length, this assay allows us to assess NA inhibition and see if there are any differences between our viruses, as we are able to analyze the distributions of the released virus populations. It has been observed that NAi treatment results in a morphological change to the released virus population, as only viruses with sufficient NA activity/concentration are able to bud in the presence of NAi (Vahey and Fletcher, 2019b). In-keeping-with our hypothesis we expected a decrease in the viral particle lengths of released SA/2003 viral particles upon NAi treatment, as longer viral particles should have a larger HA/NA imbalance and therefore less NA activity, while we expected no/minimal decrease with O/2003. As shown below in figure 5.5C, we found differences in released viral particle size in the treated condition compared to the untreated for both viruses tested. Although the magnitude of difference is much smaller for O/2003 ($p=0.0249$) vs SA/2003 ($p<0.0001$) there still is a significant difference in the overall distributions for both populations. The difference in SA/2003 however, may be explained by the other glycoprotein determinant

E271G, which may alter the neuraminidase activity. These results suggest that the glycoproteins are involved in the modulation of filament length, and this can be due to a combined effect of HA/NA balance, or changes to a single glycoprotein. In order to identify the role of NA in the differences between released and attached viruses in Figure 5.5, we needed to assess the NA activity of each virus.

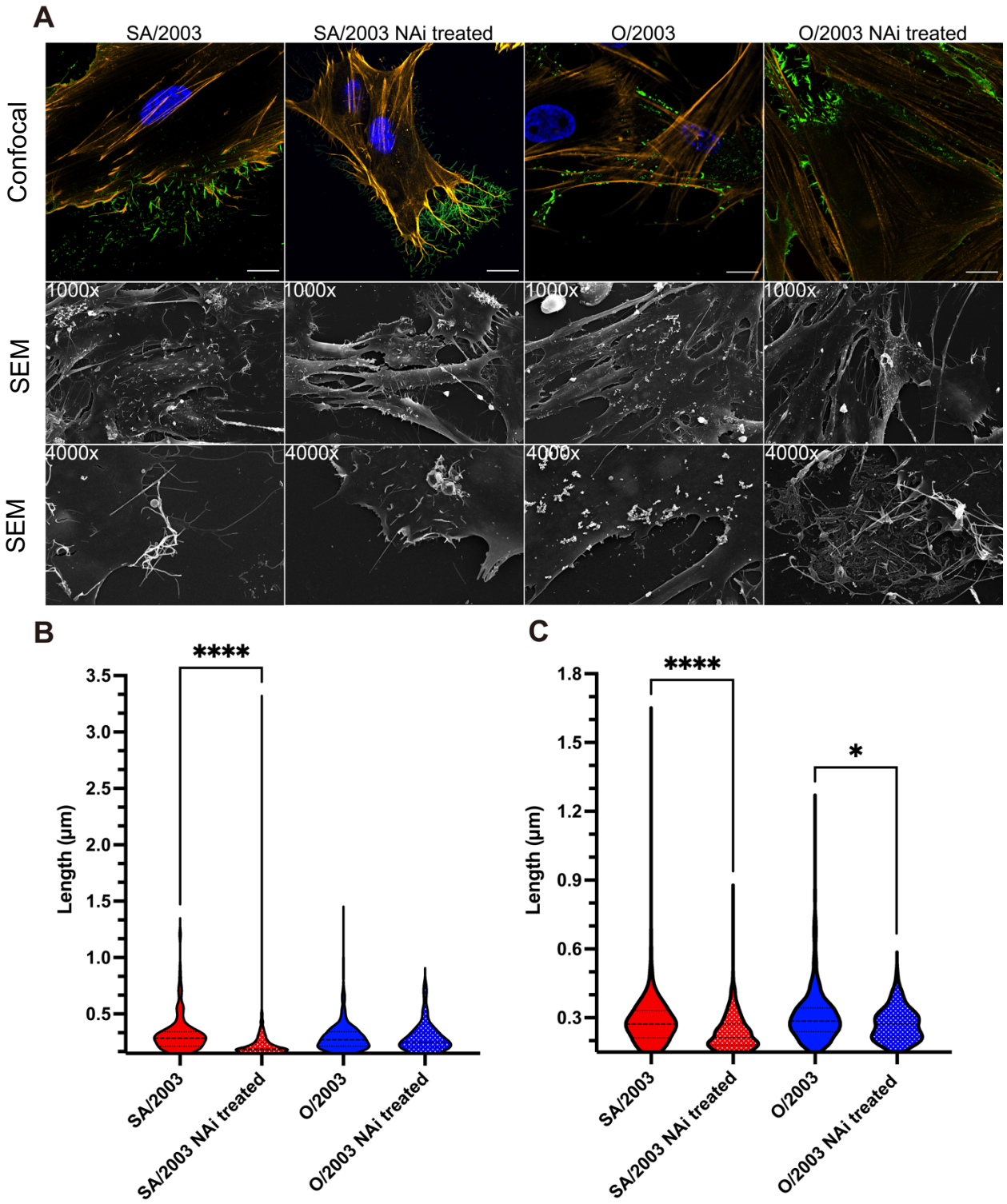

Figure 5.5 NAi treatment alters attached SA/2003 virus size, while globally altering released virus size

A) Confocal and scanning electron microscopy (SEM) show an increase in attached filamentous virus particles with NAi treatment. B) bNA treatment to

remove the attached filamentous particles shows a significant difference in particle length following NAi treatment for SA/2003 but not for O/2003. C) Released viruses following NAi treatment results in a significant decrease in virus size for both viruses. Kolmogorov-Smirnov tests comparing treated and untreated were done in both violin plots.

5.5 NA activity is independent of morphology

To determine the role of NA in morphogenesis, we first wanted to characterize the functional characteristics of each NA. To accomplish this, we ran a MUNANA assay which measured the relative fluorescence units (RFU) at every minute for a 60-minute experiment at 37^{o}C. The slope of the curve in the MUNANA assay directly relates to the NA activity of the virus. To analyze the E271G mutation in NA, we used four viruses: SA/2003, O/2003, SA/2003_ONA, and O/2003_SANA. Shown below in figure 5.6A is the activity of each virus in catalyzing the MUNANA substrate, as well as a negative control measuring any autofluorescence. Although equal amounts of infectious units were added to each well, the differences observed could be due to a variety of factors including particle morphology, particle count, and differences in NA activity. Therefore, the slope calculated from the linear regression (Figure 5.6B) is dependent on multiple variables. To remove the unwanted variables from the experiment, we normalized the activity rate by genome count (M segment) as a proxy for particle count, and we included the NA swap viruses that are both filamentous to normalize for morphology. The NA activity per genome was consistent amongst three of the viruses tested, however the E271G in an O/2003 background (O/2003_SANA) had a significantly higher NA activity per genome (Figure 5.6C). Given that SA/2003, O/2003_SANA, and SA/2003_ONA are all filamentous and SA/2003 and O/2003_SANA have the same amino acid at position 271, we can isolate changes due to the genetic background, amino acid at position 271, and morphology. The E271G mutation in a O/2003 background (O/2003_SANA) has the highest NA activity per virion, and the other three viruses have similar levels of NA activity per virion (Figure 5.6C). This suggests that the combination of these mutations plus the O/2003 background yields the highest NA activity, suggesting a difference in NA activity that is likely due to differing incorporation/distribution of NA molecules considering that it shares the same protein with SA/2003, and the same background as O/2003.

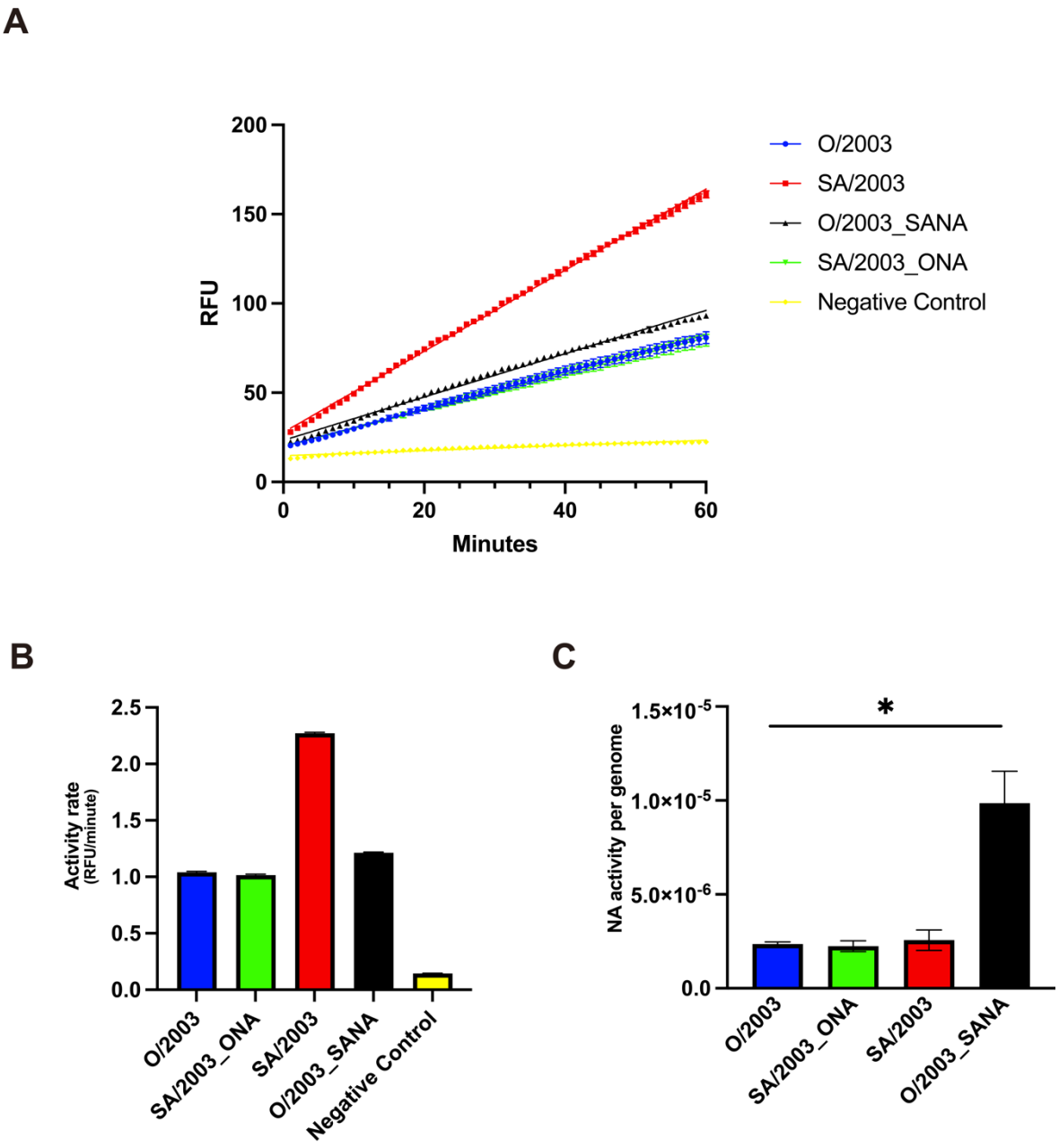

Figure 5.6 NA activity as measured using MUNANA assay shows no shape or NA dependent changes

A) The result of three independent MUNANA assays over 60 minutes at 37°C shows different RFU/time for each virus, as normalized by input pfu. B) The slope of the RFU graph represents the NA activity rate as it pertains to catalyzing MUNANA substrate. C) Normalizing NA activity per genome, shows that only one virus has a higher NA activity rate per genome. Significance between O/2003_SANA and the other viruses in panel C was calculated using a Mann-Whitney test.

5.6 NA distribution is different between SA/2003 and O/2003

The NA morphological determinant and the result in the MUNANA assay with respect to NA or morphology driven activity differences, suggests that there may be a difference in NA distribution in the viruses that causes the change. The reasoning being that normalizing NA activity per genome will give an approximate NA activity per virus particle but will not account for the amount of NA present along the length of a virus. So, if there is a significant difference in virus size there might also be a significant difference in NA incorporation into viral particles. To test whether or not the NA distribution was different in each virus, we infected E. Derm cells at the same MOI (0.1) for 24 hours and measured the NA incorporation in released viruses by NA staining. Strikingly, the differences in attached viruses by NA staining mirror that seen in the HA staining between SA/2003 and O/2003 (Figure 5.7A). Similarly, when comparing the length of NA staining, using the same method used for HA staining, between released viruses, we found a significantly different distribution of NA lengths, corresponding to a difference in NA incorporation. SA/2003 has a significantly increased mean particle length as measured by NA staining, which corresponds to a more even distribution of NA down the length of a SA/2003 filament (Figure 5.7B). When comparing the raw counts of released viral particles binned into a histogram, we found that SA/2003 has significantly higher proportions of viruses greater than 450nm in NA length (Figure 5.7C). These results suggest that while there is an equal NA activity per particle between SA/2003 and O/2003, there are differences in the distribution of NA along the viruses, which may have an affect on morphology. The reasoning follows that if there is equal NA activity per particle and the particles have differing distributions of NA, there should be differences in the balancing of binding force given the difference in glycoprotein organization. Thus, we propose that the mechanism of glycoprotein involvement in morphology hinges on a balance between HA binding and NA activity.

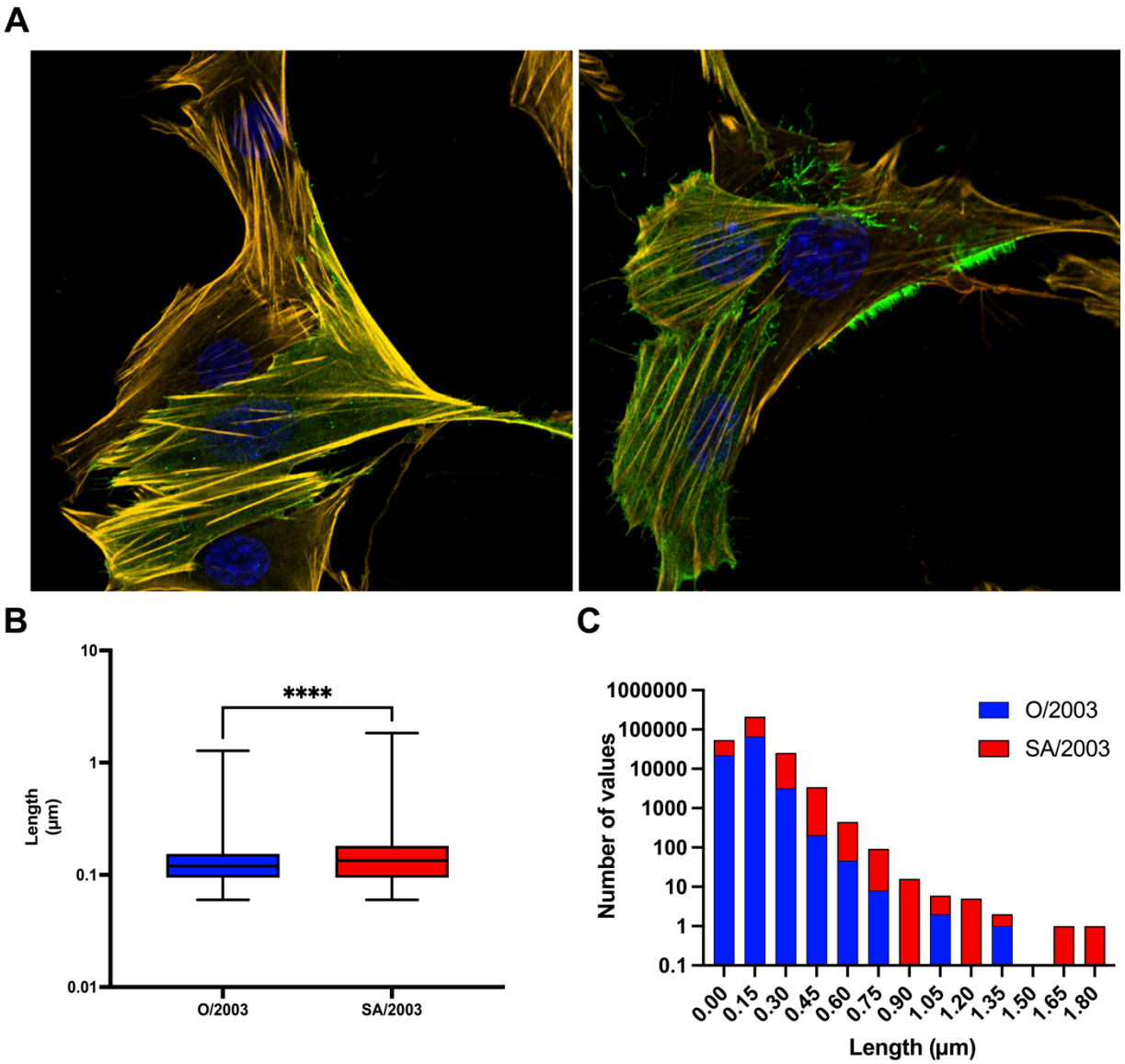

Figure 5.7 SA/2003 virus particles are significantly larger when measuring NA length.
A) Confocal micrographs of E. Derm cells infected with O/2003 (left) and SA/2003 (right) stained with anti-Neuraminidase antibody (green), show large differences in attached virus sizes. B) Significant increase in the lengths of released virus stained for NA shown between SA/2003 and O/2003. Significance determined by Kolmogorov Smirnov test. C) The length histograms for both viruses with the number of values representing absolute counts.

5.7 The ratio of HA to NA activity is independent of NA

As none of the differences in HA and NA support the initial proposed mechanism of virus elongation, we wanted to confirm if the hypothesis that HA/NA balance was a factor in the differences in morphology held any merit. To accomplish this we combined the results from the HA titer experiments (Figure 5.8A) with the NA activity data (5.8B) to produce a measure which estimates the balance of binding

to cleaving (HA to NA) per particle. Surprisingly, we found that O/2003 has the highest HA to NA ratio amongst the viruses which is contrary to the proposed mechanism. We also statistically analyzed these differences and found that the largest difference between O/2003 and O/2003_SANA was not statistically significant (p=0.10) as measured by a Mann-Whitney test. Thus, while it is clear that the changes to HA and NA are responsible for a morphological change, the mechanism by which they act is unknown.

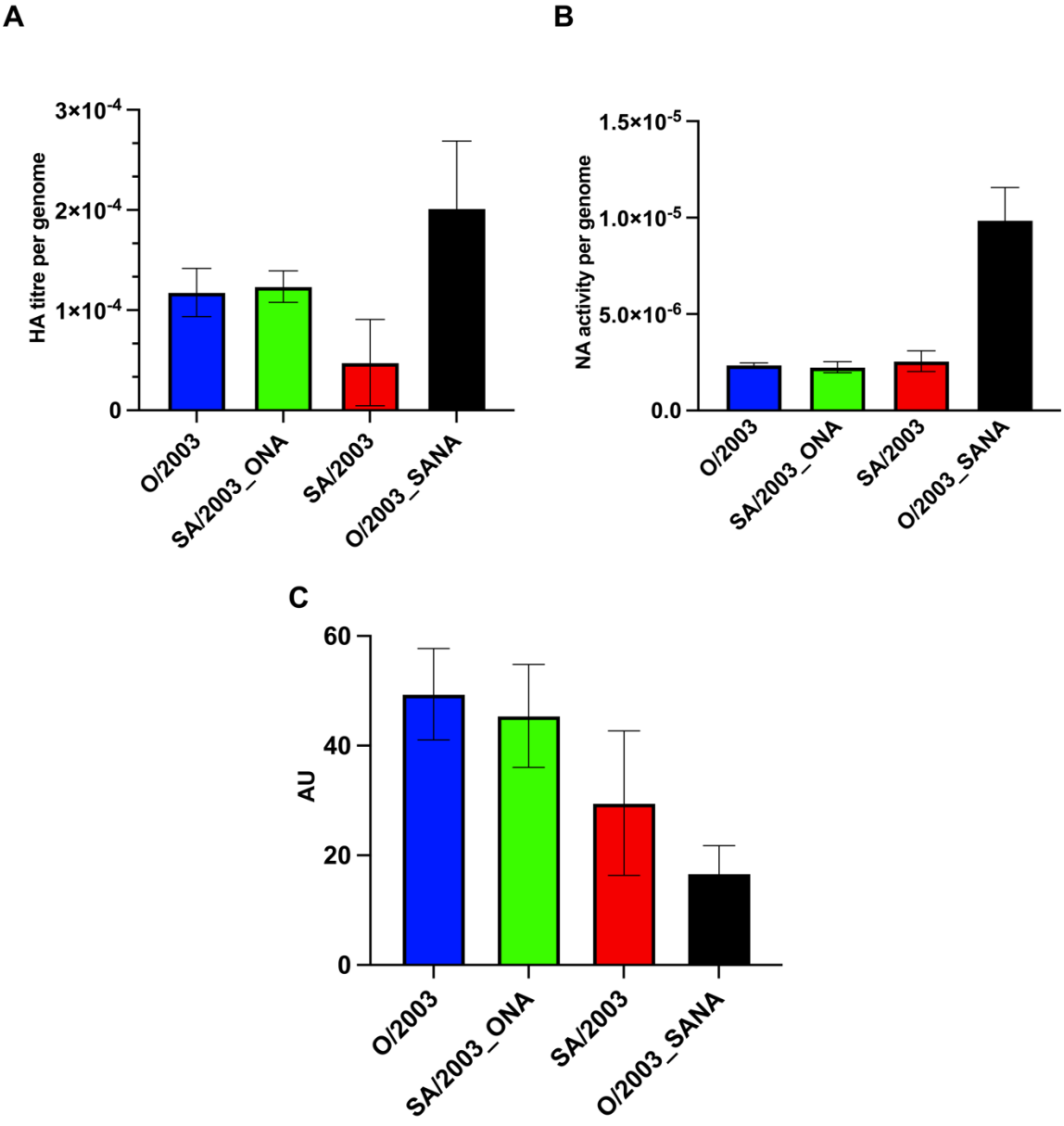

Figure 5.8 The HA/NA balance does not correlate with shape or NA
A) The HA titer per genome shows differences between O/2003_SANA and SA/2003, while there is no difference between O/2003 and SA/2003_ONA. B) The NA activity per genome is the same across O/2003, SA/2003_ONA, and SA/2003, but different when compared to O/2003_SANA. C) Combining these two metrics into a single value gives a descriptive value in arbitrary units (AU) representing HA/NA ratio, and there are no significant differences between viruses as determined by a Mann-Whitney test.

5.8 Changes to segment 1 RNA may affect RNA structure

Without a change to underlying protein, it is difficult to understand how three nucleotide changes (Figure 5.9A) are responsible for a dramatic difference in virus morphology. To this end, we attempted to understand how changes to the RNA structure could or does impact morphogenesis. The first avenue that was explored was the analysis of the underlying RNA structure, and whether the changes observed were likely to disrupt any known or predicted highly structured areas. In order to do this, we entered the complete sequence of segment 1 of SA/2003 and O/2003 into the RNAFold ViennaRNA package 2.0, which calculates the minimum free energy (MFE) prediction for each RNA sequence (Schuster et al., 1994, Lorenz et al., 2011). The RNA structure predictions generated between SA/2003 (Figure 5.9B) and O/2003 (Figure 5.9C) show large differences, while the optimal alignment of both RNA structures, which is the structure that has the lowest total free energy (Figure 5.9D) exactly matches that of O/2003 segment 1. Despite the limitations of this method with regards to predicting RNA structure for RNP associated vRNA (Hofacker and Lorenz, 2014), certain aspects of the predictions such as the short hairpin loops are plausible as they have been shown before (Dadonaite et al., 2019). Thus, the large differences between the structural predictions necessitate further investigation.

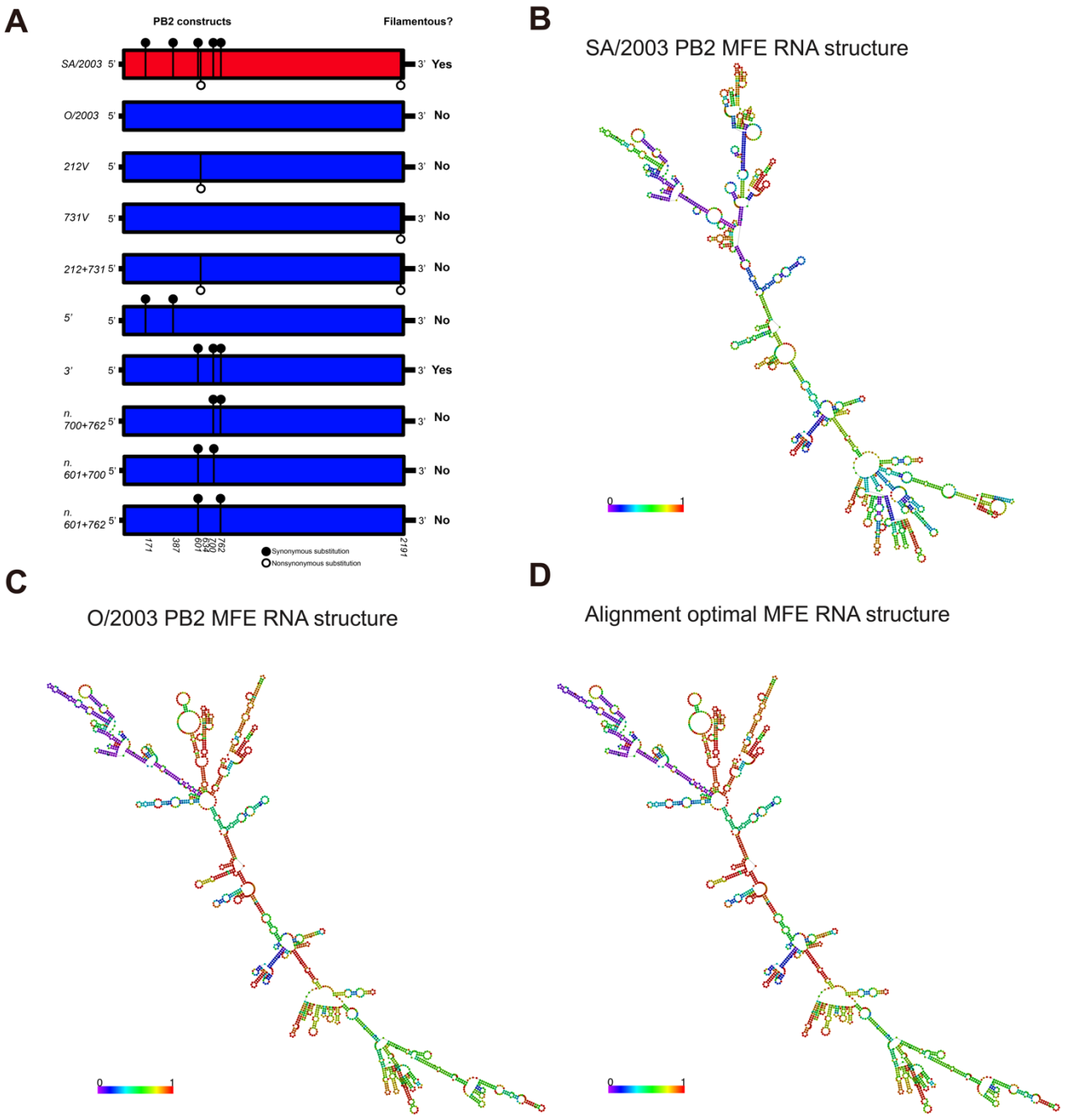

Figure 5.9 SA/2003 and O/2003 have large differences in predicted RNA structure of segment 1

A) All of the mutations and PB2 constructs between the two viruses. B) The MFE predicted structure for SA/2003 PB2. C) The predicted structure for O/2003 PB2. D) The optimal structure between SA/2003 and O/2003 PB2s. Red representing high base-pairing probabilities (closer to 100% chance, depicted by 1) and purple representing low base-pairing probabilities (closer to 0% chance depicted by 0).

5.9 No differences in genome packaging efficiency due to morphology or segment 1 changes

Given the predicted change in RNA structure and the recently studied relationship between RNA-RNA and RNA-protein interactions and genome packaging (Shafiuddin and Boon, 2019, Williams et al., 2018, Dadonaite et al., 2019), we hypothesized that the changes on segment 1 result in a genome packaging defect which could alter morphology. Although, there has not been any published research to suggest that genome packaging defects can alter morphology, it has been shown that filamentous viral particles contain fewer genomes than spherical/bacilliform particles (Vijayakrishnan et al., 2013) and that disruption of stable RNA-RNA or RNA-vRNP interactions (Le Sage et al., 2020) can decrease stability of the RNP complex. Thus, it follows that a disruption of one of these sites could affect morphology and result in a genome packaging defect.

To test the genome packaging efficiency of the viruses used we generated a multiplex qPCR assay where we infected E. Derm cells at our predefined MOI and timepoint and measured the quantities of three genomic segments of each virus. We then normalized this genome copy calculation by infectious units (PFU) to determine if we have an increase in defective particles or specific genomic segment copies. To do this we generated two primer/probe sets that amplify a conserved portion of segment 1 and segment 5 sequences (Figure 5.10A), as well as using a set of universal M segment primers and probes (Singanayagam et al., 2019). Using the reverse genetics O/2003 plasmids for each segment and Qubit measurements, we were able to accurately quantify copy number in our samples (Figure 5.10B). In addition, by titrating the supernatant at 24 hours post-infection we could quantify infectious virus (Figure 5.10C). Since we infected the cells at an MOI of 0.1 for all viruses, we expected similar amounts of virus in the supernatant after 24 hours. However, as shown in figure 5.10C, there was nearly a 100-fold increase in the titer at this timepoint. Despite the differences in infectious particle titer between the viruses, the supernatant contained similar amounts of each genomic segment measured, suggesting an increase in defective particles for SA/2003 (Figure 5.10C and 5.10D).

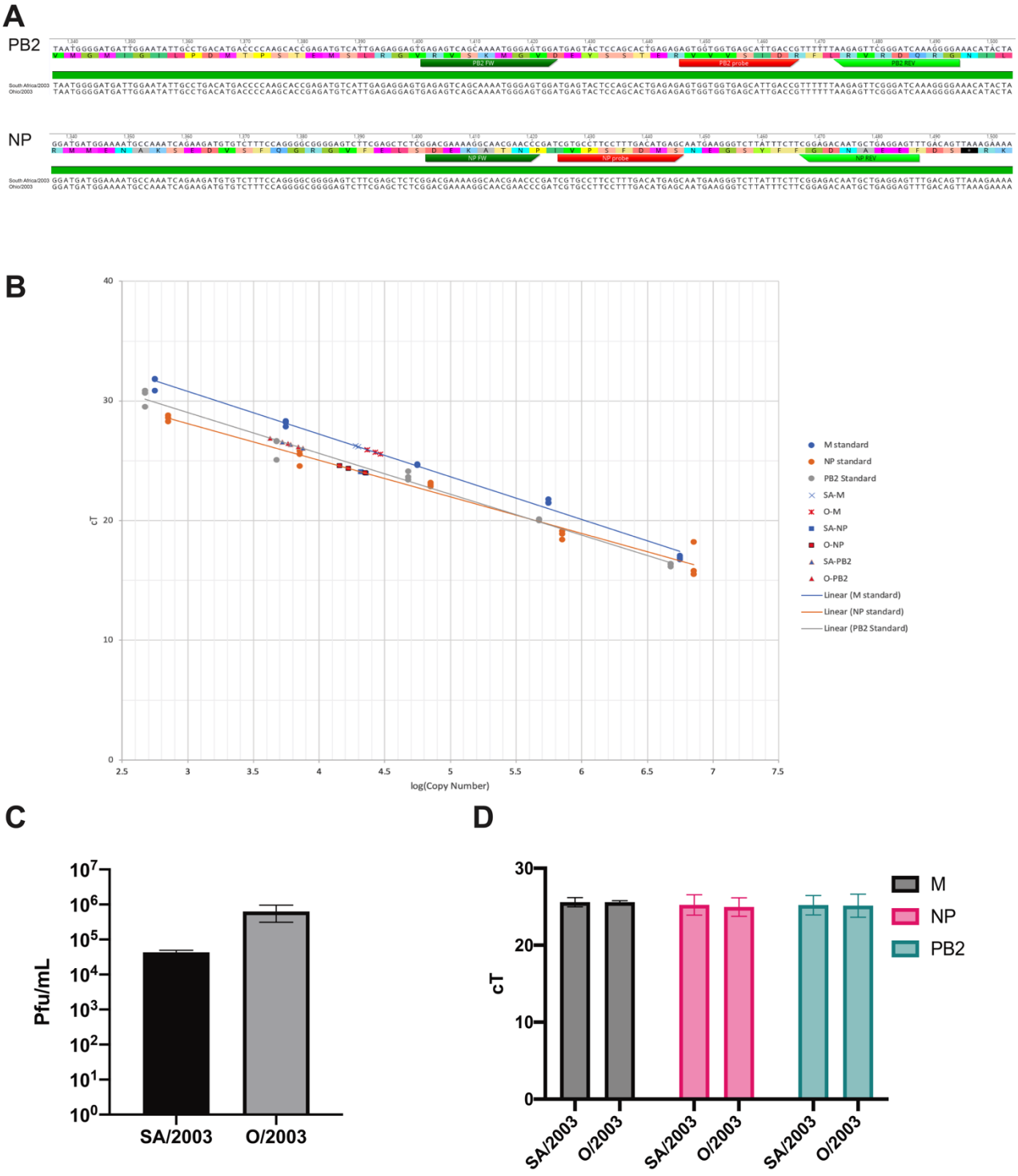

Figure 5.10 qPCR assay for the analysis of genome packaging efficiency
A) The primer (green) and probe (red) location and alignment for segments 1 and 5. B) The standard curve and sample location across the standard curve for a single experiment. C) Viral titers 24 hours post-infection. P=0.10 as measured by a Mann-Whitney test. D) The Ct values for all three experiments show no difference per run across genomic segments of viruses.

To test whether the observed change in infectious viruses was due to a change in PB2, we added two viruses to our panel: SA/2003_OPB2 and O/2003_SAPB2. The addition of these viruses allows us to identify any variable that is responsible

for a change in genome packaging efficiency, as we have three filamentous viruses, two viruses with the same PB2, and two viruses with the same background. As shown below in figure 5.11A, the packaging efficiency is variable between all of the viruses tested, however the trend observed appears to suggest that the background is the most important variable in genome packaging. While the differences between O/2003 and O/2003_SAPB2 and SA/2003 and SA/2003_OPB2 are mostly insignificant, it appears that changing the background causes highly significant differences in packaging (Figure 5.11B). Despite this, there are some differences between viruses with the same background and different PB2's, so the lack of a clear result with respect to the PB2 swaps may be due to a lack of sensitivity in the assay. In summary, this assay shows that background is of higher importance than PB2 origin and morphology (Figure 5.11C).

A

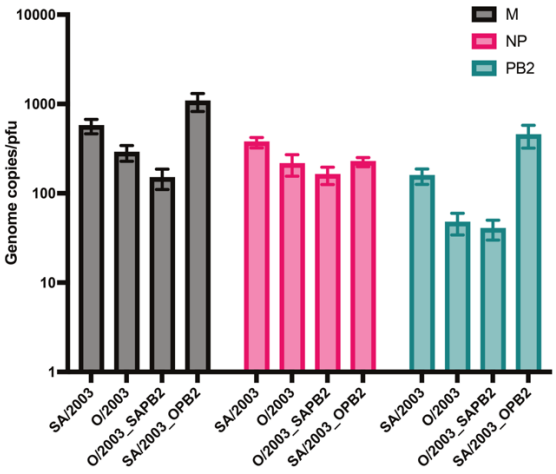

B

M	SA/2003	O/2003	SA/2003_OPB2	O/2003_SAPB2
SA/2003		*	ns	*
O/2003	*		*	ns
SA/2003_OPB2	ns	*		**
O/2003_SAPB2	*	ns	**	
NP	**SA/2003**	**O/2003**	**SA/2003_OPB2**	**O/2003_SAPB2**
SA/2003		*	ns	***
O/2003	*		ns	**
SA/2003_OPB2	ns	**		***
O/2003_SAPB2	***	ns	***	
PB2	**SA/2003**	**O/2003**	**SA/2003_OPB2**	**O/2003_SAPB2**
SA/2003		**	*	**
O/2003	**		**	ns
SA/2003_OPB2	*	**		***
O/2003_SAPB2	**	ns	***	

C

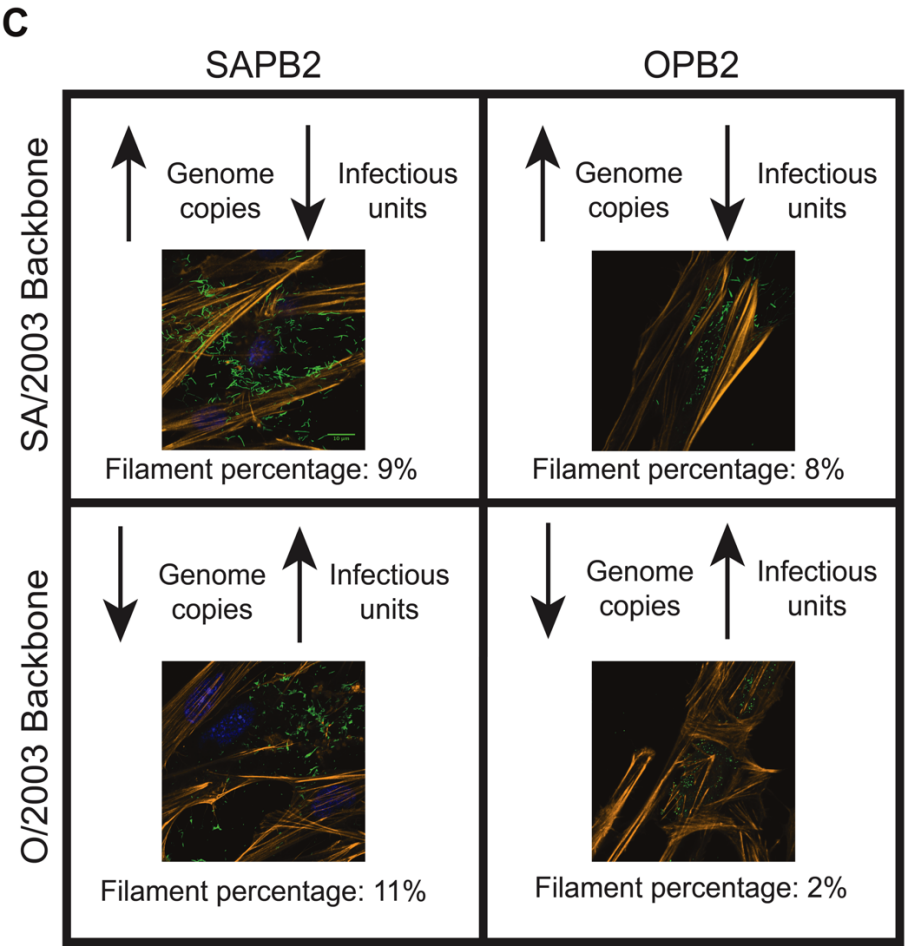

Figure 5.11 The genetic background is the most important factor in packaging efficiency

A) The genome copies per pfu for each virus and each genomic segment tested. B) The significance between each virus for each genomic condition as measured by a Mann-Whitney test shows large differences between viruses with different backgrounds and small to no differences between viruses with the same background and different PB2. C) A summary of the viruses tested displays aforementioned results.

5.10 Discussion

In an attempt to understand the mechanistic underpinnings of the observed morphological shift, we encountered some interesting and contradictory results. For our segment 1 mutations, we were able to show differences in the predicted RNA structure and a slight effect of segment 1 on genome packaging efficiency. Although, the effect of the segment 1 swap was much less than that of the other seven segments, suggesting the mutations in segment 1 are acting in a different way then was hypothesized.

With regards to the role of the amino acid changes on morphology we were able to show that sialic acid removal can hamper filament formation, while being unable to demonstrate a HA or NA specific effect. In an attempt to identify changes in NA activity we used a MUNANA assay that gives an approximation of NA activity, although the MUNANA substrate is a α2,6 analog. So, the lack of differences in NA activity per particle may be substrate dependent, however it has been shown previously that the MUNANA was sufficient to identify distinctions between two avian neuraminidases (Blumenkrantz et al., 2013). Despite the lack of differences on a per particle basis, we did find highly significant disparities in NA distribution between the viruses. So further research into NA's role in morphogenesis may focus on both activity of individual NA tetramers, as well as the role of distribution of NA molecules and how this can affect budding and morphology. Although none of the NA or HA experiments converge to the hypothesized mechanisms, some of the results represent novel findings. For example, the sialic acid experiment (Figure 5.2) clearly shows that the extracellular environment has a large role to play in IAV morphology. In addition, the NA distribution experiment and NA activity experiment challenge some of the existing research on NA distribution and activity in filamentous virions. NA has been shown to be highly polarized in Udorn and Victoria filaments (Vahey and Fletcher, 2019b, Vijayakrishnan et al., 2013), but our data suggest that this is not a universal phenotype of filamentous virions, as SA/2003 virions appear to have a more diffuse NA distribution down the length of the virus. Likewise, the data on NA activity and its relationship to morphology clearly state that NA activity is directly correlated with virus size (Campbell et al., 2014, Seladi-Schulman et al., 2014), however our data show that NA activity is morphology independent. This difference could be due to a change in strain but

can also be due to differing methods. While both of these papers report NA activity differences, they cannot ascertain the NA activity per virion, as they do not normalize by genome. This highlights the importance of normalizing by genome copies, as it allows us to identify alterations that are likely due to either differing NA activity or differing distributions between viruses.

Together our data on HA and NA involvement in morphogenesis and its relationship to current filament research suggests a difference in the organization of budding sites between Udorn/Victoria, spherical viruses, and H3N8 EIVs. While polarized and concentrated NA in a Udorn filament requires an ordered array of glycoproteins on the budding membrane in order to have a portion of the filament that is rich in NA, a diffuse distribution of HA and NA in our EIVs suggests a more disordered budding site, more similar to that which has been observed for spherical viruses (Vahey and Fletcher, 2019b). To this end, in order to understand the mechanisms underlying the M-independent morphological determinants identified herein, we need to have a greater understanding of the ultrastructure of the IAV budding site.

6 Ultrastructure of IAV budding sites

The role of multiple segments in morphology and specifically the role of novel morphological determinants in the head regions of HA and NA and the RNA structure of segment 1 suggest that there are a variety of factors that are involved in IAV morphogenesis. Given that there are no clear convergent or even divergent mechanisms underlying the identified determinants and no clear avenue to proceed for each segment/protein individually it is necessary to have a global structural understanding of the process of IAV morphogenesis. A lot is known about the latter stages of the IAV replicative cycle, as is summarized below, although there are highly relevant gaps that need to be addressed. Of these unknowns, the ones that are most relevant to the scope of this project are RNP organization and trafficking to the budding site, organization of the membrane proteins at the budding site, and the cellular factors that are associated with filament formation.

Once fully formed vRNPs exit the nucleus they accumulate around the MTOC and are then distributed around the cytoplasm into puncta that grow as the infection progresses (Amorim et al., 2011, Chou et al., 2013, Eisfeld et al., 2011, Vale-Costa et al., 2016). It has been shown that these puncta contain diversity amongst the different IAV segment RNPs and this diversity increases with proximity to the plasma membrane (Lakdawala et al., 2014). This observation led to the hypothesis that these vRNP puncta are viral inclusions that are responsible for the sorting and formation of RNP complexes (Vale-Costa and Amorim, 2017). More recent studies have shown these puncta require Rab11 to form and are in fact liquid organelles that concentrate RNPs to allow for RNP-RNP binding and the formation of assembled or partially assembled genomes that can then be trafficked to the site of budding (Alenquer et al., 2019). These viral inclusions/liquid organelles are associated with ER exit sites and thus move around the cell with ER membranes (Alenquer et al., 2019). What is unknown however, is how the RNP complexes that form in these liquid organelles are then transported to the site of budding. It has already been shown that the last stages of RNP transport do not take place in rab11 positive vesicles, and also are not helped by microtubules that can be disrupted by nocodazole despite RNPs having been recorded moving at a speed consistent with microtubular transport (Avilov et al., 2012, Momose et al., 2007).

These results together seem to suggest a microtubular transport that it is not affected by nocodazole (Friedman et al., 2010), which points toward vRNPs sliding on ER membranes (Alenquer et al., 2019). The association between vRNPs and the ER and the mechanism of ER sliding, while microtubule dependent, is resistant to nocodazole treatment, suggests a possibility for the latter stages of vRNP transport. Despite this hypothesized model for genome trafficking to the site of budding, the specifics of sensing and transport of IAV genomes is unclear.

The architecture of the IAV budding site is important because it modulates differences between non-infectious, semi-infectious, and infectious particles, as well as the structural changes between large filaments with no genomes and spherical viruses with a 7+1 genome organization. Likewise, the distributions of membrane proteins that are incorporated into the viral envelope are important for functions that are specific to certain morphologies, as it has been shown the filamentous IAV have polarized NA, while spherical viruses have a more uniform glycoprotein distribution (Vahey and Fletcher, 2019b, Vahey and Fletcher, 2019a, Vijayakrishnan et al., 2013, Dadonaite et al., 2016). Despite these findings, we have observed differences in distribution of glycoproteins between our viruses, suggesting a difference in protein organization on the membrane. The lateral organization of the IAV proteins in the budding site as described in a cell transfected with WSN RNA segments suggest that HA and M2 form co-clusters in lipid raft domains (Calder et al., 2010), with HA being at higher concentration in the raft domain and M2 located on the periphery of the raft possibly binding cholesterols present in these regions (Calder et al., 2010, Leser and Lamb, 2017). NA, on the other hand, has been shown to cluster in discrete homogeneous patches on separate domains in the plasma membrane (Leser and Lamb, 2017). These data suggest a highly regulated system of membrane organization that allows for proportional incorporation of each glycoprotein; however, it is unclear whether this organization is morphologically dependent. Given that HA and NA have been shown to be the main drivers of IAV budding and their concentration has a direct effect on local alterations to membrane curvature (Chlanda et al., 2015), it follows that distributional changes of these proteins may alter virus shape.

In addition to vRNP transport and budding site organization, an unknown component of IAV morphogenesis is the incorporation and role of cellular proteins.

It has been hypothesized that actin in particular has a role in driving filament formation and possibly some role in the structural stability of fully formed viruses (Vijayakrishnan et al., 2013), however this has not been shown in a conclusive manner.

To attempt to resolve these unanswered questions in IAV morphogenesis and genome packaging, it is necessary to have a clear picture of the cytoplasmic site of budding. To investigate the pleiomorphic structural details of the budding of enveloped viruses such as IAV, it is necessary to use cryogenic electron tomography (Cryo-ET). Cryo-ET is a method whereby you plunge-freeze in liquid ethane to embed samples in vitreous ice and image them in a transmission electron microscope, as shown on figure 3.1B. A series of two-dimensional projection images are collected at various angles around an axis to generate a tilt-series, these angles are produced by a tilting of the image stage (Figure 3.1C). From this tilt-series, you can computationally create a three-dimensional volume called a tomogram. Tomography can yield resolutions of less than 10nm making it well suited to the study of enveloped virus morphogenesis (Ghosal et al., 2019). Recent developments in cryo-EM hardware such as direct detection devices, Volta phase plates, and energy filters have enabled the improvement of both the contrast gleaned from samples, as well as the resolution (Tegunov et al., 2021, Bammes et al., 2012, Danev et al., 2014). Despite the recent advances in Cryo-ET, there are still limits of thickness that have prohibited the imaging of the interiors of vitrified cells. These barriers have necessitated the use of other imaging modalities such as focused ion beam scanning electron microscopy (FIB-SEM) and plastic sectioned transmission electron microscopy (TEM) (Zachs et al., 2020, Winey et al., 2014). Although both techniques can provide answers to these questions, they both come with major drawbacks. For example, while FIB-SEM can provide detailed ultrastructure of the area of interest, the production of the lamella and the identification of the area of interest is extremely complicated and time consuming (Polilov et al., 2021). Likewise, while traditional TEM methods may be relatively straightforward in execution, plastic sectioning can lead to artifacts due to both the resin and the compression during and after microtomy (Winey et al., 2014). To this end, we attempted to do cryo-ET of vitrified cells and image the thin edges of infected cells without excess manipulation. While this would require large amounts of optimization to ensure the cells were thin enough,

there was ample virus present, and the ice was sufficiently thin, it would provide a native state budding site description that would shed light on these gaps in the IAV replicative cycle.

To this end, there are a few determinations that need to be made with regards to imaging setup that have a large downstream effect on the quality of the tomograms produced. The first of these determinations is tilting scheme, or the method by which the tilt series is operated. There are two main options: unidirectional, where you start at a high tilt angle and tilt through all the angles until you get to the high negative tilt angle (-60^{o}->+60^{o}) and dose-symmetric, where you start at 0^{o} and work your way up to the high tilt angles by a bidirectional tilt scheme. An example of this with a 3^{o} spacing would be as follows: 0^{o}, 3^{o}, -3^{o}, 6^{o}, -6^{o}, etc. The benefit of a unidirectional tilt is mechanical, as smaller degree differences between tilts results is smaller lateral movements of the stage, and thus smaller differences for the software to account for. The benefit of the dose-symmetric tilt scheme is primarily data retention, as the dose through the sample increases throughout collection and the last tilts collected are at the highest tilts (the tilts with the least information). Although it puts the most pressure on the software and stage stability, we opted for a dose-symmetric tilting scheme to have the highest possible resolution in our reconstruction. The second of these determinations is objective lens defocus, which is the distance beyond the specimen corresponding to the focal length. For example, 0 µm defocus would correspond to a focal plane at the specimen, while a defocus of -12µm corresponds to a focal plane 12µm closer to the lens. It has been shown that, in the absence of phase plates, a higher defocus allows for easier segmentation while a focused sample is more ideal for sub-tomogram averaging (Hagen et al., 2017). Given that this is a mostly qualitative description of the IAV budding site, we opted for a higher defocus collection of -12µm. In addition to the defocus, we used gold colloid solution for fiducial markers, and we used a concentration of 2 x 10^{11} particles/mL and a size of 20nm per particle.

6.1 Optimization of cryo-ET in E. Derm cells

To generate a high-resolution description of the IAV budding site it was first necessary to optimize a system for cryo-ET of infected cells. Given that all of the work thus far has been done in E. Derm cells, it follows that E. Derm cells would be the first cell line that we would use in these experiments. Before transitioning to EM, it was important to determine the thickness of E. Derm cells to see if they would be suitable for cryo-EM. In order to determine suitability, we infected E. Derm cells at a higher MOI than the previous experiment (MOI=1) for 24 hours to see how the cells would respond to the increased stress. The rationale behind changing the infection conditions were two-fold: firstly, in order to image at high magnification, it would be necessary to have more virus present and secondly, by testing a higher MOI and timepoint we would be able to identify if E. Derm cells would round-up and therefore become impenetrable to the electron beam. Luckily as shown below in figure 6.1, E. Derm cells are resilient to high levels of infection and are very flat. Figure 6.1A is a z-stack confocal micrograph showing a heavily infected E. Derm cell, while figure 6.1B shows a 3D plot of the depths of the cell at various points along the xy plane shown in figure 6.1A. As you can see in figure 6.1B, there were areas of the cell where the thickness reached nearly 70μm, however most cell edges and in fact part of the interior of the cell was well below 10μm in thickness. Given that a 300KeV microscope is able to penetrate thick samples on this scale (Martynowycz et al., 2021) and the areas of budding are located on cell edges, E. Derm cells should be well suited to analysis by cryo-ET.

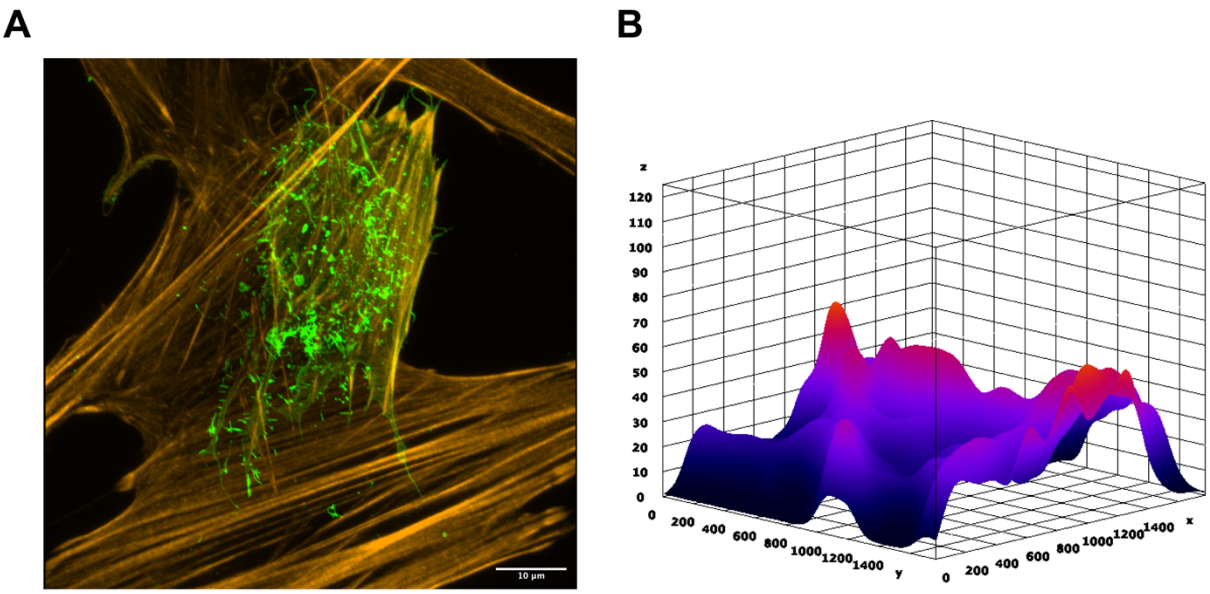

Figure 6.1 E. Derm cells are sufficiently thin for cryo-ET analysis
A) A confocal micrograph showing a z-stack slice of an infected E. Derm cell (SA/2003, MOI=1, 24hpi). Actin in orange, HA in green. B) A 3D plot of the thickness of the cell imaged in (A) shows that various portions of the infected cell are sufficiently thin to be imaged using cryo-ET.

The physical characteristics of the cell type are one piece of the optimization puzzle, as it is also necessary to optimize the growth and infection of E. Derm cells on a holey carbon film coated gold EM grid. In order to propagate E. Derm cells on grids it is necessary to coat the grids in laminin, a main component of the extracellular matrix, and choose a seeding density that would allow for two things: the correct ratio of a single cell per grid square, as well as giving enough time for the E. Derm cells to stretch themselves in order to have them be as thin as possible. As far as optimization of growth conditions, a laminin concentration of 50µg/mL and 24 hours of incubation time at 37^{o}C was sufficient to provide a stable matrix for E. Derm growth (Vijayakrishnan et al., 2013). Cell density, on the other hand, was slightly more complicated as E. Derm cells were never used in cryo-ET before. Previous virological studies using fibroblast cell lines in cryo-ET, have determined that an ideal seeding density should be between $5x10^4$ and $1.5x10^5$ cells per a 35mm MatTek dish (Hampton et al., 2017). Initially, we tried three cell densities ($5x10^4$, $8x10^4$, and $1.1x10^5$), and found that $5x10^4$ was the most suitable. After propagating this number of cells on a grid for two days prior to infection, we found that we reached a uniform distribution of thin cells that grow in the center of the squares (Figure 6.2A). The next optimization step was the infection conditions. For the confocal images shown in previous chapters, we infected cells at low MOI

in order to not saturate the system. However, in cryo-ET without any correlative microscopy it would be necessary to infect with a higher MOI, not only to increase the amount of virus present to image, but also increase the frequency of budding events. This higher MOI can come with drawbacks, as the increased stress on the cells can cause rounding which reduces the chances of finding an area thin enough to penetrate with an electron beam. Therefore, we first attempted to go in with a MOI of 1 as we were confident based on that data in figure 6.1 that the cell would be sufficiently thin for imaging. Holding MOI constant allowed for us to only alter time of infection. It has been shown that EIV infection of E. Derm cells results in virus from the initial infection being released at 6-8 hours post-infection and subsequent cycles of infections occurring at roughly 6 hour intervals (Crispell and University of Glasgow). Thus, in attempting to find the ideal time where we would expect to see budding events, it would follow that at the beginning of those intervals: 6 hpi, 12 hpi, 18hpi, and 24 hpi, we should expect to see a high frequency of budding events. To this end, we tested two of these timepoints 6hpi and 18 hpi, as we already had confirmation of high levels of infection at 24hpi. Firstly, we looked at 6hpi as shown below in figure 6.2B, we were able to visualize the cytoplasm of E. Derm cells, although the cellular projections as denoted by the red dotted line are not certainly virus budding events. This lack of certainty suggests that we need a later time point to positively identify infected cells. However, what is clear at this timepoint is the ability to discern cellular compartments (Figure 6.2B, green arrow), actin networks (Figure 6.2B, yellow arrow), and microtubules (Figure 6.2B, blue arrow). The second incubation time, 18hpi, was found to provide high levels of infection and thin cell edges and was the timepoint that was used for the remainder of the experiments.

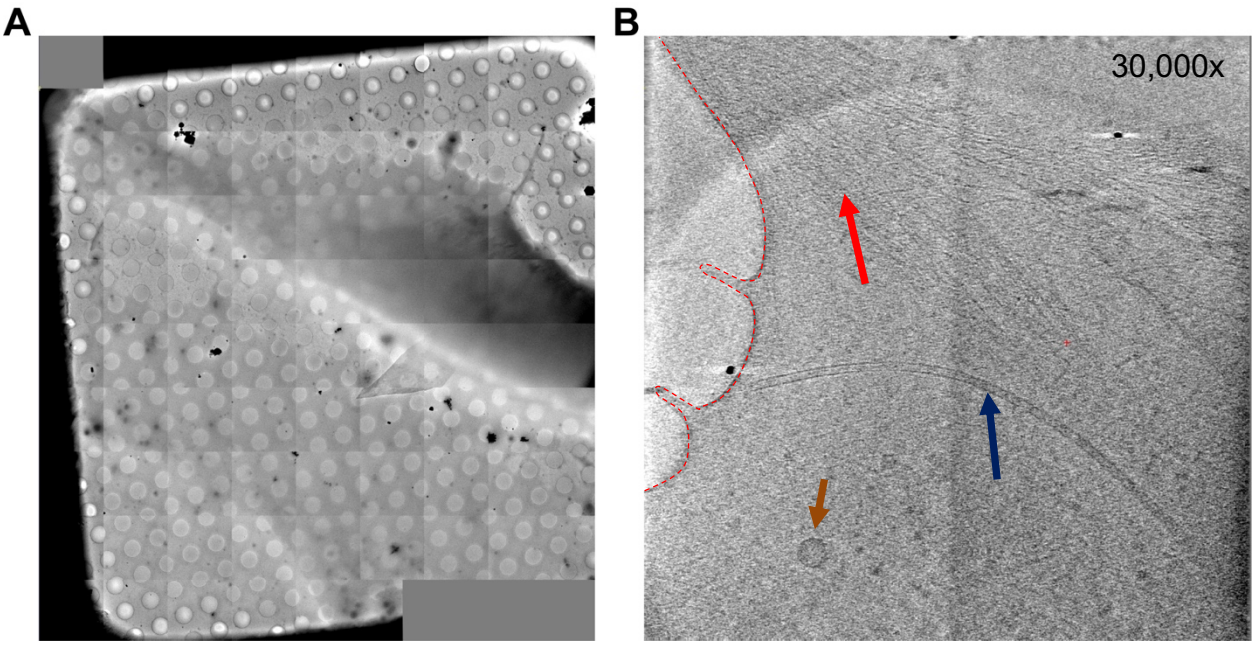

Figure 6.2 E. Derm cells can grow on laminin coated EM grids and are sufficiently thin to image through
A) A 2µm grid square showing the optimal cell density for imaging, one cell per grid square, 2/2 µm. B) A 2D slice of a tomogram showing that E. derm cells are thin enough to image by TEM at 6hpi. Various cellular features are visible at this magnification: cell edge and cellular protrusions (red dotted line), actin (red arrow), vesicle (brown arrow), and microtubule (blue arrow).

6.2 Imaging strategies for optimal budding sites

Given the optimization of cellular conditions and infection time at MOI of 1, the only thing remaining to optimize was the imaging strategy. Although the imaging of the budding sites from heavily infected cells appears straightforward, the process of discerning productive areas of membrane from the low magnification map (3,000x) as seen in figure 6.2A is not facile.

We found primarily through trial and error that the areas we should target were large cellular projections, as they were areas that had a combination of thin edges and high frequency of virus budding (Figure 6.3A). These areas as seen in the figure below, which was infected at MOI 1 for 18 hours, have an ideal combination of these traits and are easily discernible from the lower magnification maps. From the lower magnification maps we were able to generate higher magnification maps of these projections (3,000x, Figure 6.3B), which gave us an idea of what areas we wanted to collect data. Once we identified the higher magnification area that we wanted to collect data (Figure 6.3C), it then became a matter of deciding the specific microscope settings that were ideal for qualitative analysis.

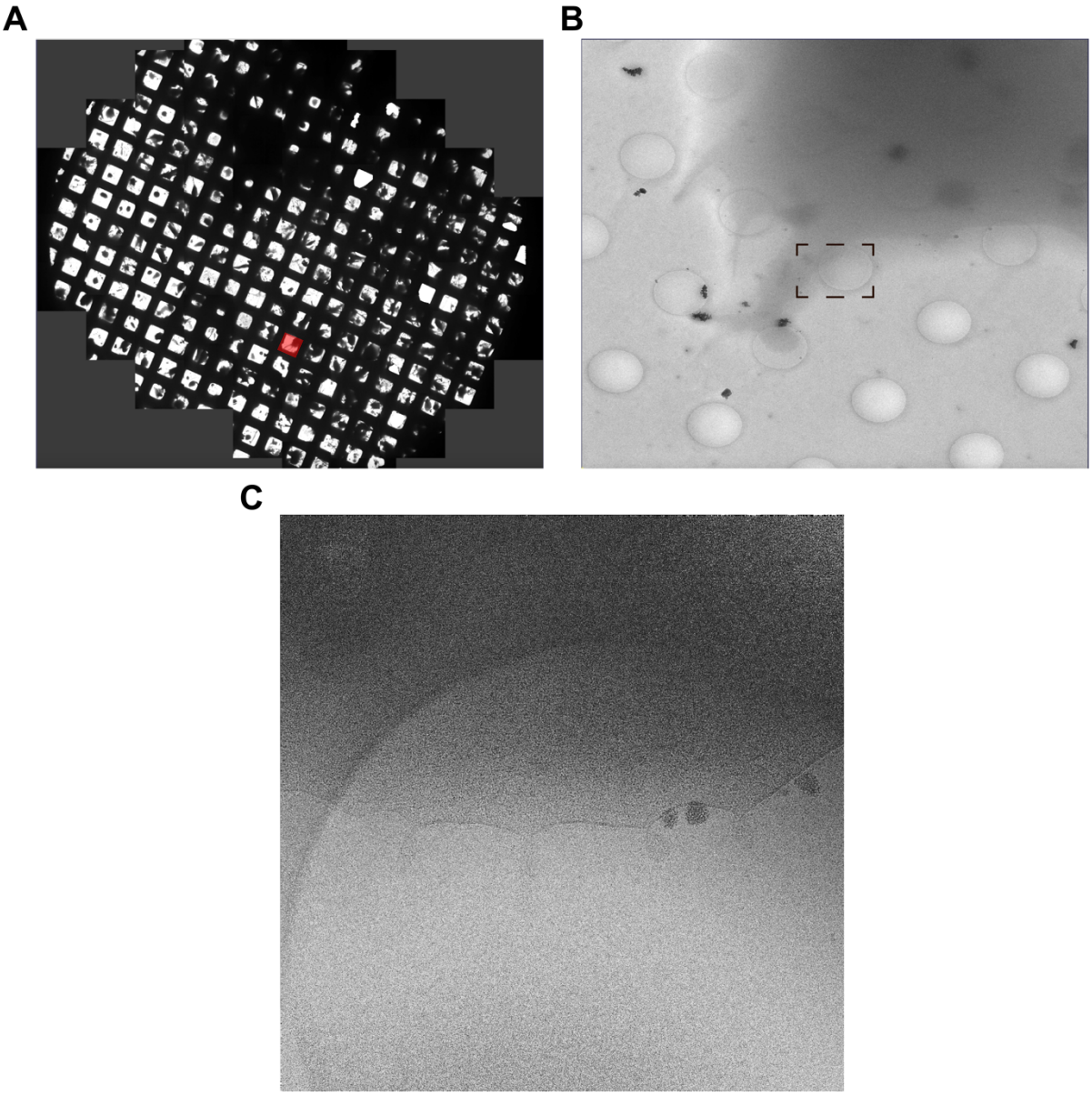

Figure 6.3 Low magnification maps to high magnification region of interest
A) A low magnification map (200x) of the entire grid allows for the picking of cells that are infected. Through trial and error, it was determined that cells that have large projections are the most ideal candidates as they have more regions that are sufficiently thin. The cell imaged is shown in red. B) The map of the cell of interest was then produced and areas of cell edge that were over a hole, thin enough to image, and near a projection, chosen for further examination (dashed box). C) An anchor map of this region showing an area of cell membrane that appears to contain budding or membrane pearling.

6.3 Observation of filamentous particles and budding sites

Having determined the collection strategy and tilt scheme, we could now identify and capture regions of interest. As previously mentioned, the goal was to image active budding sites in order to provide a high-resolution description of the cytoplasmic side of budding. As shown below in figure 6.4, we could capture various stages before, during, and after budding. Likewise, we could clearly show the increased proportion of filamentous particles which matched the observations and quantitation seen in the previous chapters. These observations are highlighted by the various colored arrows, with the red arrow on figure 6.4A showing a budding bacilliform virus, the yellow arrow on figure 6.4B showing a budding filament, and the blue dashed line on figure 6.4C highlighting the cellular periphery that has produced a large number of filamentous virions.

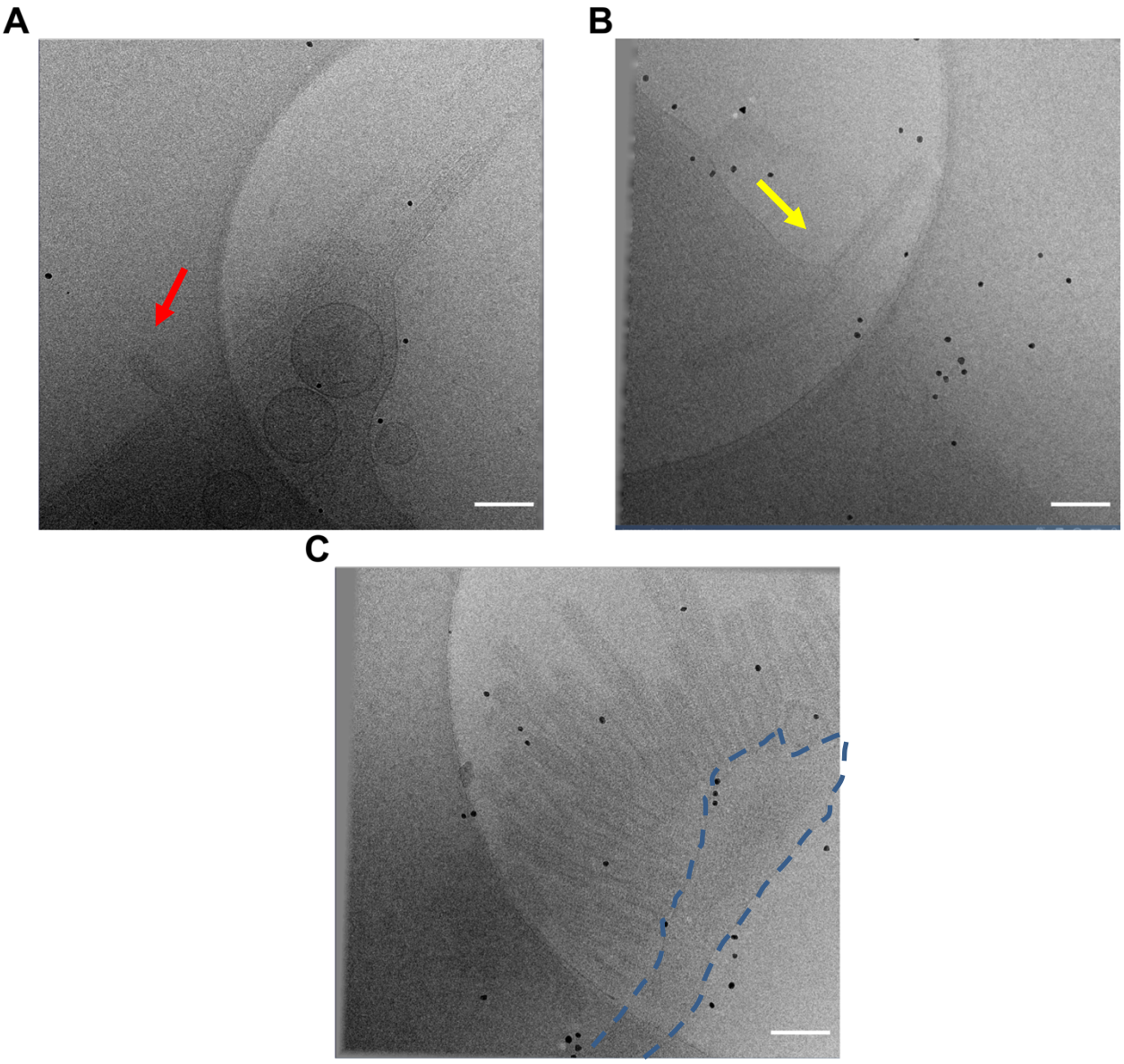

Figure 6.4 Raw tilt series show IAV budding sites at various stages
A) Early stages of budding shown on a cellular projection, budding bacilliform virus denoted by red arrow. B) Filamentous virus completely budded away from the membrane indicated by the yellow arrow. C) An irregular cellular projection outlined in blue with many budding IAV filaments.

6.4 Tomogram generation and comparison between pipelines

Now that we have collected raw data from the microscope, the next step in producing final data for downstream analysis is tomogram generation. Tomograms, as mentioned in the introduction, are three-dimensional volumes that are produced from a series of tilted images. There are two main software programs that we applied to this analysis: etomo (Kremer et al., 1996) and EMAN2

(Tang et al., 2007). The main differences between these two software packages for the purposes of this project are twofold: reliance on fiducials and automation of the pipeline. Etomo is a graphical user interface (GUI) based software that requires manual input for registration of gold fiducials, adjustment of image tilt, and tomogram generation method. To this end, it allows for the optimization of poorly aligned tomograms and more user input on the specifics of tilt-series alignment. EMAN2 on the other hand is a mostly automated system, which only requires the input of specifications that are not gathered from the image metadata. It aligns the tomograms using patch-tracking and a Fourier reconstruction algorithm, which is different from either SIRT or back-projection used in etomo. Therefore, it has allowed us to generate tomograms when it has not been possible in etomo. However, of these tilt-series that were able to be analyzed in both etomo and EMAN2, we found that etomo produced better results (Table 6.1). More specifically, we found that while EMAN2 produced higher contrast tomograms due to the increased binning required for the patch tracking algorithm, the alignment was less precise (Figure 6.5A). In addition, we found that there were some tomograms that were unable to be reconstructed in one or the other software package. As shown below in figure 6.5B, we have one tomogram on the left that was reconstructed only in etomo and one tomogram on the right that was only reconstructed in EMAN2. Together these data suggest that the time investment required for tomogram reconstruction in etomo is most likely worth the effort, and might be useful to quickly generate tomograms that may contain sufficient detail and resolution to be used for downstream analysis such as, segmentation or sub-tomogram averaging. Likewise, either pipeline is well suited to analysis, and etomo in particular is well suited to high contrast tomograms for segmentation analysis (Figure 6.5B, left). The decision on tomogram reconstruction software now allows us to move to the next stage of the data analysis pipeline, observations of areas of interest and segmentation of these areas.

Table 6.1 Summary of tomogram generation by software package.

	etomo	EMAN2	Better Result
Tilt10_July2019	✓	✓	etomo
Tilt11_July2019	✓		etomo
Tilt12_July2019	✓	✓	etomo
Tilt1_Dec2019	✓		etomo
Tilt2_Dec2019	✓		etomo
Tilt4_Nov2020	✓	✓	etomo
Tilt5_Nov2020	✓	✓	etomo
Tilt7_Nov2020		✓	EMAN2
Tilt8_Nov2020		✓	EMAN2
Tilt9_Nov2020		✓	EMAN2
Tilt16_Nov2020	✓	✓	etomo
Tilt18_Nov2020		✓	EMAN2

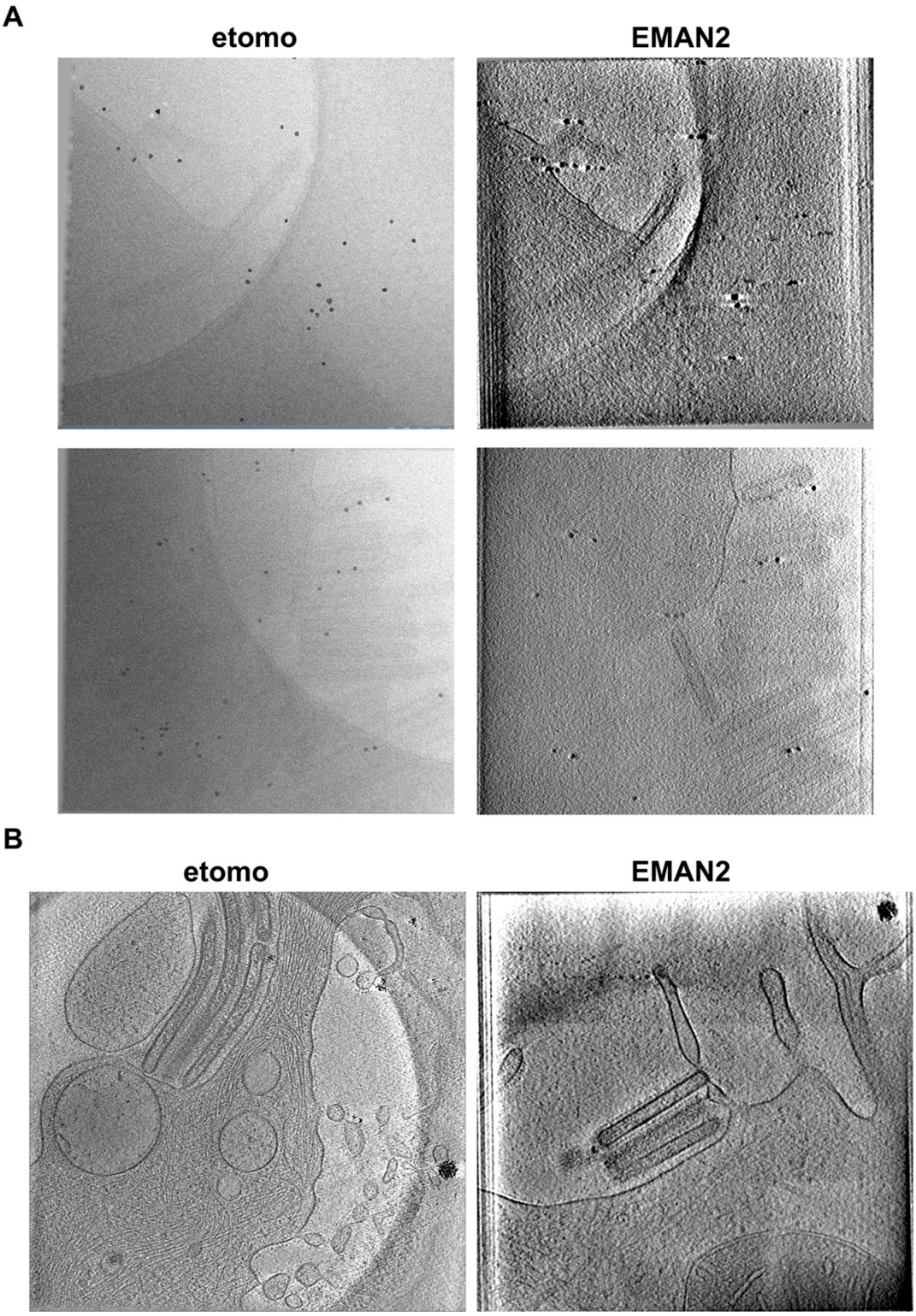

Figure 6.5 Comparisons between etomo and EMAN2 reconstructions
A) Two tilt-series reconstructed using etomo (Left) and EMAN2 (Right) show differing alignment precision and contrast. B) Two tomograms that were only reconstructed well using one software package.

6.5 Interesting observations

In order to identify areas for further analysis we looked for repeating structures in each tomogram and tried to match these areas to the existing literature. To do this, we used data from all twelve tomograms generated and combined these data to increase the statistical power of these observations. Three main observations were gleaned from this dataset and are visible in three tomograms. As shown in figure 6.6A, there are three tomograms that we produced that highlight important features. All three of these tomograms have active budding sites, on figure 6.6A (left) we see a budding site over the carbon film on the left side of the cell projection denoted by the orange arrow. On figure 6.6A (center), we see two budding sites: one which appears to have produced a large number of filaments (purple arrow), and membrane curvature that is starting to form (green arrow). Lastly, on figure 6.6A (right), we see an active budding site (yellow arrow) that has produced and appears to be still producing virions. One commonality between all these tomograms was the presence of ribosome-like particles in high abundance near the budding site, and in fact this was also observed in every one of the twelve tomograms reconstructed. While this should come as no surprise, as ribosomes are ubiquitous parts of the cellular architecture and their ubiquity has been shown in detail in cell-lines (Mahamid et al., 2016), it appeared that they weren't uniform in size. In figure 6.6B, we show close-up summed slices of the tomograms showing regions containing these ribosome-like structures, however it is important to note that the pixel size and the magnification of these areas are not the same. What is interesting, however, is the organization of these structures as figure 6.6B (Left and center) show small numbers of these structures either in no visible organization (Left), or around an isolated membranous structure (center). Figure 6.6B (Right) however, shows a large amount of these structures that more closely match that seen in previous research (Mahamid et al., 2016). In order to determine the identity of these ribosome-like structures, we measured the diameter of 74 structures across twelve tomograms (Figure 6.6C). The summary of these measurements exhibited in figure 6.6C shows a median diameter of less than 20nm, although the average eukaryotic ribosome is between 25-30nm (Yusupova and Yusupov, 2017).

Another feature of interest that was observed in one-third of the twelve tomograms were the vesicle/compartments that are shown in figure 6.6D. These vesicles in both cases are located near the putative budding site and contain similar densities and evaginations (Figure 6.6D, red arrows). It is unknown what these compartments and the densities inside them are, however, their location and frequency suggest some role. In addition to the observations in the cytoplasmic site of budding, another observation gleaned from this dataset is the presence of many well-resolved filaments, as well as other IAV morphologies (Figure 6.6E). Of the 62 filaments observed, we found that over 90% of them had identifiable genomes (Figure 6.6F), which is a higher percentage than that was found in Udorn filaments in previous studies (Vijayakrishnan et al., 2013). Together these data raise interesting questions about both the architecture of the filamentous IAV budding site, as well as differences in genome incorporation between divergent pleiomorphic strains. To further probe this architecture, we set out to create a three-dimensional model of one of the infected cells and the various areas of interest therein.

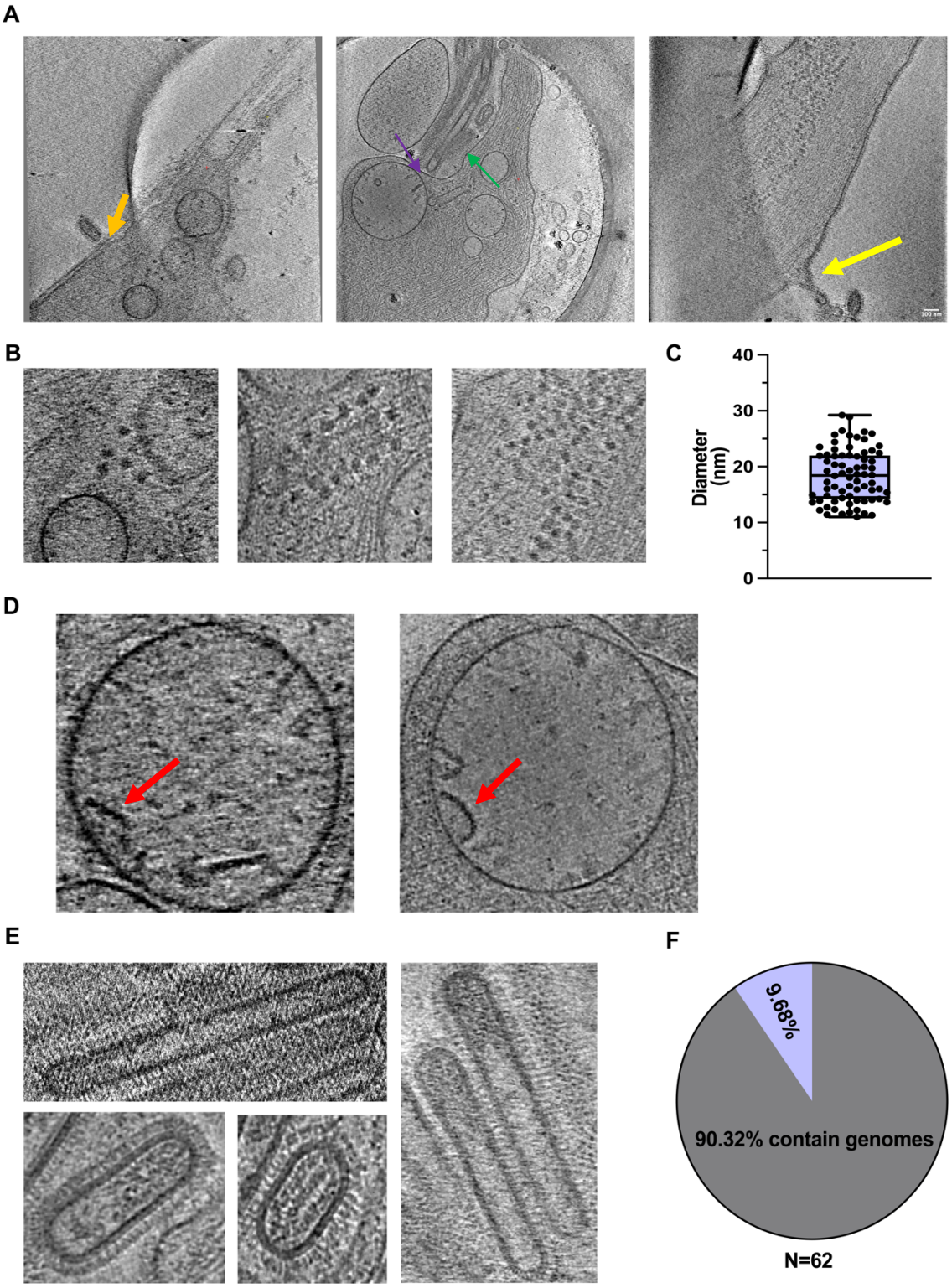

Figure 6.6 Selected observations from reconstructed tomograms
A) Summed slices from 3 tomograms with budding events show the global architecture of the cytoplasmic site of budding. Orange, purple, green, and yellow arrows show budding sites at various stages. B) Zoomed view of the ribosome-like structures in the above tomograms. C) Diameter of 74 of these structures shown in a min-to-max box and whiskers plot. D) Membrane compartments underlying budding sites have unidentified densities (red arrows). E) A collection of filaments and other IAV morphologies observed across the tomogram dataset. F) Pie-chart showing the distribution of genome containing filaments to empty filaments across 62 measured virus particles.

6.6 Segmentation of cytoplasmic site of budding

In order to generate this three-dimensional model, we used Amira (ThermoFisher) for segmentation. Only one of the 12 tomograms generated was of sufficient quality for meaningful segmentation and had multiple areas of interest worth segmenting. As shown below, we were able to produce a three-dimensional model of this tomogram. Specifically, we focused on the membranous structure surrounded by the ribosome-like particles, the membrane compartment with the unknown densities and the interactions between them (Figure 6.7A, left). Our first attempt in segmentation as shown in the right panel of figure 6.7A was based on automated thresholding of membranes and provided a useful starting point, although it was highly unspecific and highlighted membranes as well as cortical actin. To provide a more detailed model of this infected cell, we resorted to manual segmentation of these areas, as well as the cell as a whole. Using the brush tool complemented with interpolation, we were able to produce a model which included all of the areas of interest (Figure 6.7B). To this end, we generated a model of the cell membrane (Figure 6.7B, yellow), viral membranes (Figure 6.7B, light blue), vesicles/intracellular compartments (Figure 6.7B, red), densities inside one of these compartments (Figure 6.7B, magenta), membrane/ribosome-like structure compartments (Figure 6.7B, green and purple), and the glycoproteins studding an area of high membrane curvature (Figure 6.7B, dark blue). In addition, we have focused on a subset of these areas: the unknown ribosome-like complex (Figure 6.7C, top-left), a putative budding site with glycoproteins (Figure 6.7C, top-right), and membrane compartment with densities (Figure 6.7C, bottom).

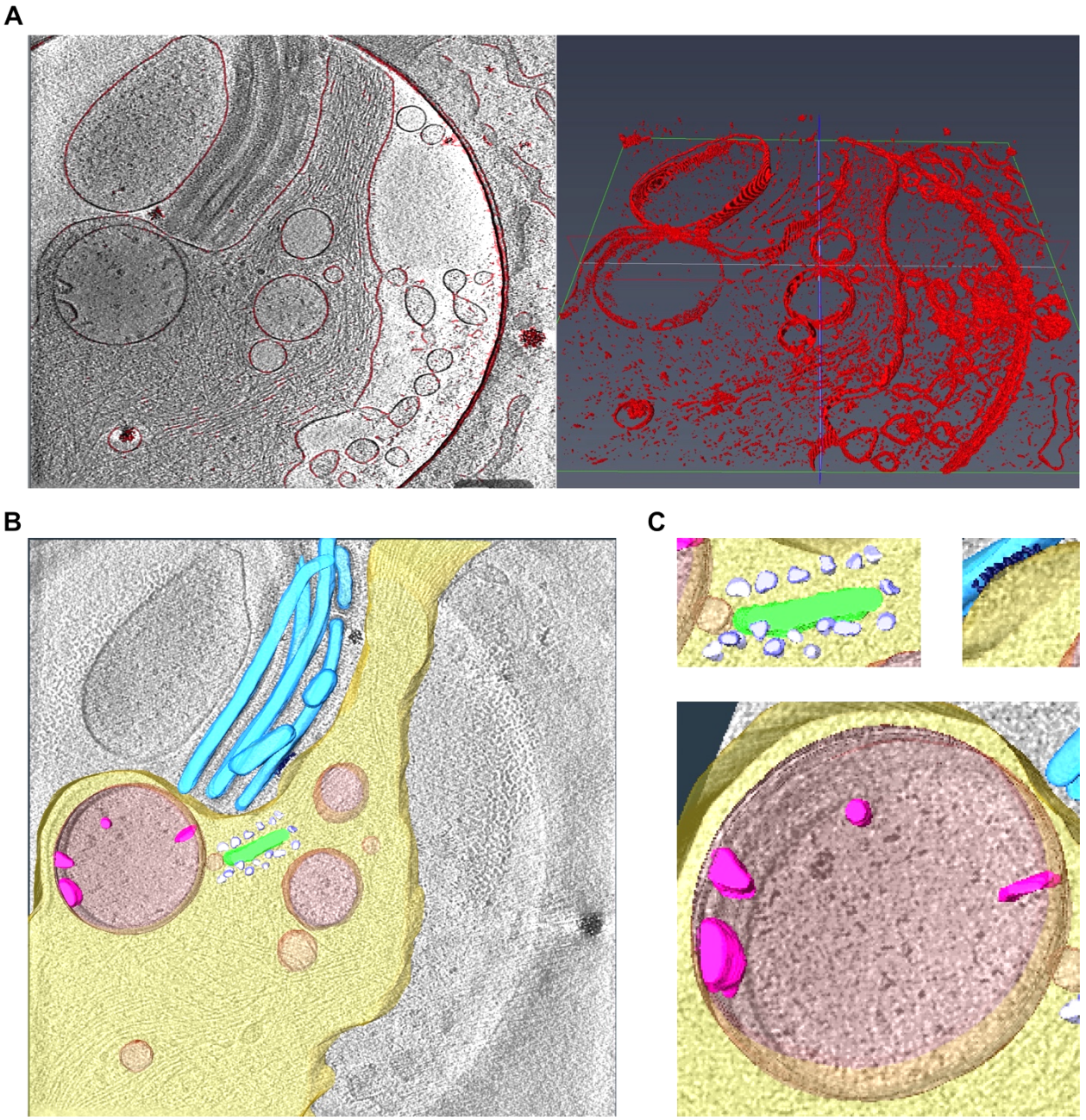

Figure 6.7 Segmentation of an infected cell highlights areas of interest
A) Threshold segmentation (right) of a tomogram (left) resulted in precise highlighting of membranes at the expense of specificity. B) Manual segmentation leads to a less precise, but specific representation of an infected cell. Each area of interest was segmented as a different material with a different color. C) Zoomed-in regions of interest from (B) including: ribosome-like complexes and an associated vesicle (Top-left), glycoprotein studded curved membrane (Top-Right), and large cellular compartment with unknown densities (Center).

6.7 Discussion

The overarching goals of this chapter were two-fold: produce a method that enabled investigations of the unknown latter stages of IAV budding in a near-native state and provide some of the answers to these unknown questions. To the first point, we were able to provide a clear methodology from the culturing and infection conditions of E. Derm cells on quantifoil grids, to the collection and processing strategies that yield the best results. Although, we were unable to definitively answer any of the unknowns with relation to membrane organization, genome trafficking, or involvement of host factors, we were able to show interesting and likely relevant observations.

Specifically with regards to genome trafficking, it has been shown previously that the latter stages of genome trafficking and vRNP clustering must occur in a Rab11 independent manner, as Rab11 has not been shown to be present near budding sites, as well as a microtubule independent manner, although ER transport was unaffected. To this end, we have observed multiple ribosome-like structures which differ in size to ribosomes and could possibly be clustered RNPs. The median size of these unknown structures 19nm, corresponding to the diameter of a fully formed RNP bundle and in fact these structures, or at least a subset of them, are plausibly fully formed RNP bundles (Noda and Kawaoka, 2010). The organization of these structures at least in the complex shown above in Figure 6.7C, are plausibly an isolated ER extension or RNP organizational center for plasma membrane transport. Unfortunately, the most important missing piece to this observation is the lack of control samples, as this result could simply be a section of migrated rough ER and these ribosome-like structures may in fact be ribosomes. The role of the membrane compartment that is attached to this ER-like structure is unknown, but it is possible that the densities inside this compartment are also related to the trafficking of viral proteins or genomes to the site of budding. However, the presence of this complex and the adjacent vesicle and membranous compartment at least suggest that this methodology if followed may allow for the answering of these lingering questions.

To this end, reasonable next steps for following this line of investigation would be both continuing with the current methodology and simply collecting more data, as well as improving the methods to achieve a higher success rate in finding these

areas. On the subject of improvements, the most obvious improvement would be the inclusion of correlative imaging. Ideal correlative targets for future work would include RNA probes to multiple IAV genome segments, labelled ER proteins, or labelled Rab11. Addition of any one of these markers would greatly improve both the simplicity associated with finding these regions, as well as the confidence in correctly identifying parts of the ultrastructure. Although one of the aims of this section was not fulfilled, we were able to show a proof-of-concept for cryo-ET of thin edges of cells that could lead to a renewed focus on imaging vitrified cells on grids. The two main alternatives to this type of approach: FIB-SEM and plastic sectioned TEM, both have drawbacks whether it’s difficulty and cost (FIB-SEM), or compression artifacts (TEM).

7 General Discussion

The primary aims of this project were to identify and understand the mechanisms underlying IAV morphology, and how they relate to the generalized process of morphogenesis. To aid with this investigation we used a combination of molecular techniques coupled with high resolution light and electron microscopy.

It is known that the main determinant in morphology amongst all IAVs is the main protein product of segment 7, M1 (Peukes et al., 2020, Elton et al., 2013). It is also known that the amino acid positions that are key to morphological change are highly conserved (Elton et al., 2013). As well, it has been shown that alterations to these positions are linked to changes in stability to the native structure of the M1 protein when it is in its filamentous helical arrangement (Peukes et al., 2020). Other proteins that have been shown to be implicated in morphological change are M2, NP, HA, and NA (Bialas et al., 2014, Jin et al., 1997, Beale et al., 2014), but specifically the regions that interact with M1. It has been hypothesized that changes to the cytoplasmic tail regions of these glycoproteins and M1 interacting regions of NP destabilizes the M1 interactions that are necessary for filamentous budding (Rossman and Lamb, 2011). Therefore, it is known that four proteins that all interact with the main structural protein M1 are important for filament formation. What has not been known however is whether M1 independent mutations could have a role in morphology. To this end, we showed that alterations to the head domains of HA and NA were sufficient to increase filament proportion. This challenges the notion that all IAV structural determination was done either through direct alterations to the M1 protein or destabilizing interactions with M1. In addition, there is no precedent for synonymous changes affecting IAV structure, yet we found three synonymous changes that act in conjunction to alter virus shape. Lastly, while genetic redundancy has been shown for some positions in M1 (Elton et al., 2013), no one has shown the role of multiple segments acting in concert to produce a bacilliform virus population.

Starting with the non-synonymous mutation identified on segment 4 (HA), it is clear that alterations to the protein are in some way affecting the proportion of filaments in the released virus population. Unlike the morphological determinants

previously shown in HA (Jin et al., 1997), the identified position HA Q236P is located on the globular head of the HA protein. We hypothesized that changes to the head region of HA would have an effect on binding, and this change to binding avidity/affinity would act as a pulling force during filament formation. This idea is based primarily on the experiments which show that HA/NA balance can lead to directed motion on a coverslip coated with sialic acid analogs (Guo et al., 2018, Sakai et al., 2018) or air liquid interface culture systems with naturally generated sialic acid linkages (Vahey and Fletcher, 2019a). What is not known however, is whether these forces, which must act during budding, are significant enough to alter morphology. While the attempts to explain the phenomenon in the context of filament elongation during budding proved unsuccessful, it is clear that the residue change Q236P alters the function of the protein in some way. We attempted to identify any functional differences between HA proteins by doing multiple experiments looking at the role of sialic acid binding in filament proportion, as well as looking at virus elongation changes in the absence of NA activity. In addition, we looked at the hemagglutination titers at various temperatures, in order to determine if there was a temperature, background, or HA dependent difference in HA titer. These experiments were unsuccessful in supporting the hypothesized mechanism, although we had some positive albeit contradictory results. However, these experiments did not provide a direct look at any of the functional characteristics of HA. Thus, future work to interrogate the differences in HA in a more direct fashion. To this end, we suggest an in-depth structural characterization of this amino acid change that would probably yield a more concrete answer on the mechanism underlying this mutation. Although it was not possible during the time period allotted for this work, it would be interesting to look at a comparison of HA binding force between the two HA proteins using soluble HA preparations and biolayer interferometry (BLI), which allows you to measure the lengths of interactions between HA and sialic acids.

To this end, we also observed a non-synonymous change (A812G, encoding E271G) in segment 6 (NA) that results in a morphological change between the two viruses, which we attempted to address in a similar manner to the that for HA. However, in contrast to the methods that we used to characterize HA, we were able to directly address the role of NA activity using a MUNANA assay. While we could have opted for a MUNANA assay of the protein expressed in transfected

cells, we chose to proceed with the protein in context of the viral particle because we wanted to parse differences between NA activity, NA incorporation, and morphology. When comparing the activities of the NA protein in the context of different genetic backgrounds we found there was no significant difference between the wild-type viruses. Although this lack of change was observed in a substrate that mimics α2,6 and this is not representative of the natural tropism of EIV, it has been shown that MUNANA catalyzation is valid for neuraminidase activity comparison as verified by an erythrocyte elution assay (Blumenkrantz et al., 2013). That being said the development of an assay using fetuin (Couzens et al., 2014), an α2,3 analogue, would provide another avenue to assess functional differences between the two viral NAs. Likewise, given the lack of differences between the wild-type viruses despite the effect on morphology, it is reasonable to suggest that future work should focus on producing a EIV N8 structure, as the current harbor seal structure, which is a H3N8 IAV as well (Yang et al., 2015) has a 87.7% amino acid identity so is likely to be different from an equine H3N8. In a similar vein to the studies done on HA, we also analyzed the activity or resistance to inhibition of NA using an indirect approach. We treated infected cells with a neuraminidase inhibitor, Oseltamivir acid, to determine if there were any differential effects based on the NA positional change E271G. While we found attached filaments increased regardless of the NA or backbone, we did not see any differences in filament percentage between viruses for either attached or released virus particles. This is unsurprising, as the NA amino acid change is unlikely to affect the active site of the protein, however the result that NA inhibition increases the length of viral particles clearly shows a role for NA activity in morphogenesis.

The synonymous changes that we observed in segment 1 (PB2) however, required a different kind of analysis, as there was no change to the protein product. While we attempted to address the role of these mutations in genome packaging, it is unclear where in the replicative process they would act. Although outside the scope of this project, it suggests that these nucleotide changes have some effect on either the RNA structure or RNA-RNA/RNA-protein interactions, as there is no other plausible explanation. Although, a control experiment comparing the polymerase activity using a minireplicon assay would have shown this directly. Future work should focus on two types of analysis: selective 2’-hydroxyl acylation

analyzed by primer extension and mutational profiling (SHAPE-MaP)(Smola et al., 2015), and psoralen-cross-linked, ligated and selected hybrids (SPLASH)(Aw et al., 2016). SHAPE-MaP is a technique which utilizes the flexible and accessible regions of RNA and acylates them. Given that the unpaired regions are more accessible they are more likely to be acylated, so one can analyze the acylation pattern by reverse transcription, amplification, qPCR, and sequencing. SPLASH on the other hand is a technique by which you cross-link base-paired RNAs, in order to analyze RNA-RNA interactions. SPLASH has been used previously in IAV research to probe the network of intersegment interactions for WSN (Dadonaite et al., 2019), and it was found that specific loci are important for stable interactions between segments. Thus, a combination of these techniques would allow for both a high accuracy RNA secondary structure, as well as an analysis of the network of RNA-RNA interactions that are possibly modulated by the synonymous change in segment 1.

Due to our inability to identify the mechanisms underlying the morphological change, we opted to analyze, and attempt to understand how such a change might occur by looking at morphogenesis and the structure of the IAV budding site. To this end, we were able to create a system whereby we could seed, infect, and vitrify E. Derm cells on a carbon coated EM grid, and observe them in a near native state. We were able to identify and image budding sites on thin cell edges without any undue manipulation and characterize the cellular ultrastructure. Despite the advances we were able to achieve in cryo-ET of un-milled cells, we were lacking the ability to accurately identify multiple structures of interest. To this end, future work should focus on optimizing our current pipeline for the inclusion of correlative markers whether it be fluorescently tagged IAV genomic segments or gold-labelled antibodies against a glycoprotein. The ability to discern the densities present in the identified membrane compartments, or the true nature of the ribosome-like structures, would only be possible with the addition of a correlative marker. To this end, other imaging modalities may also be appropriate for these questions, as preliminary work using soft x-ray cryo-tomography was attempted and resulted in similar pitfalls.

The various factors that result in a change from a spherical morphology to a pleiomorphic morphology together with the observation that among all 138 EIV genomes the three loci identified are unique, suggest an importance for filaments. While this has been covered and shown with respect to IAV morphology, the preponderance of evidence points to filaments as important in other viruses such as respiratory syncytial virus (RSV), Ebola Virus, tobacco mosaic, bacteriophages, and others (Zanotti and Grinzato, 2021) and other pathogens such as, filamentous bacteria and fungi (Pfeffer et al., 2012, Grimm et al., 2005). Filamentous viruses have varied ways to produce filaments, for example, it is matrix-dependent for most enveloped viruses (VP40 for Ebola Virus (Noda et al., 2002), matrix protein based for RSV (Ke et al., 2018)), and capsid protein for tobacco mosaic virus (Caspar, 1963). Despite these differences, the undoubted evolutionary fitness of this morphology has caused convergence. This parallel evolution highlights the importance of IAV filament research as a topic worth exploring further, as it is extremely clear that filaments are not artefactual and are in fact present across multiple taxonomic kingdoms.

References

AL-MUBARAK, F., DALY, J., CHRISTIE, D., FOUNTAIN, D. & DUNHAM, S. P. 2015. Identification of morphological differences between avian influenza A viruses grown in chicken and duck cells. *Virus Res,* 199**,** 9-19.

ALENQUER, M., VALE-COSTA, S., ETIBOR, T. A., FERREIRA, F., SOUSA, A. L. & AMORIM, M. J. 2019. Influenza A virus ribonucleoproteins form liquid organelles at endoplasmic reticulum exit sites. *Nat Commun,* 10**,** 1629.

ALNAJI, F. G. & BROOKE, C. B. 2020. Influenza virus DI particles: Defective interfering or delightfully interesting? *PLoS Pathog,* 16**,** e1008436.

AMORIM, M. J., BRUCE, E. A., READ, E. K., FOEGLEIN, A., MAHEN, R., STUART, A. D. & DIGARD, P. 2011. A Rab11- and microtubule-dependent mechanism for cytoplasmic transport of influenza A virus viral RNA. *J Virol,* 85**,** 4143-56.

ARTHUR, R. J. & SUANN, C. J. 2011. Biosecurity and vaccination strategies to minimise the effect of an equine influenza outbreak on racing and breeding. *Aust Vet J,* 89 Suppl 1**,** 109-13.

AVILOV, S. V., MOISY, D., NAFFAKH, N. & CUSACK, S. 2012. Influenza A virus progeny vRNP trafficking in live infected cells studied with the virus-encoded fluorescently tagged PB2 protein. *Vaccine,* 30**,** 7411-7.

AW, J. G., SHEN, Y., WILM, A., SUN, M., LIM, X. N., BOON, K. L., TAPSIN, S., CHAN, Y. S., TAN, C. P., SIM, A. Y., ZHANG, T., SUSANTO, T. T., FU, Z., NAGARAJAN, N. & WAN, Y. 2016. In Vivo Mapping of Eukaryotic RNA Interactomes Reveals Principles of Higher-Order Organization and Regulation. *Mol Cell,* 62**,** 603-17.

AYLLON, J. & GARCIA-SASTRE, A. 2015. The NS1 protein: a multitasking virulence factor. *Curr Top Microbiol Immunol,* 386**,** 73-107.

BADHAM, M. D. & ROSSMAN, J. S. 2016. Filamentous Influenza Viruses. *Curr Clin Microbiol Rep,* 3**,** 155-161.

BAJIMAYA, S., FRANKL, T., HAYASHI, T. & TAKIMOTO, T. 2017. Cholesterol is required for stability and infectivity of influenza A and respiratory syncytial viruses. *Virology,* 510**,** 234-241.

BAMMES, B. E., ROCHAT, R. H., JAKANA, J., CHEN, D. H. & CHIU, W. 2012. Direct electron detection yields cryo-EM reconstructions at resolutions beyond 3/4 Nyquist frequency. *J Struct Biol,* 177**,** 589-601.

BARMAN, S., ALI, A., HUI, E. K., ADHIKARY, L. & NAYAK, D. P. 2001. Transport of viral proteins to the apical membranes and interaction of matrix protein with glycoproteins in the assembly of influenza viruses. *Virus Res,* 77**,** 61-9.

BARMAN, S. & NAYAK, D. P. 2007. Lipid raft disruption by cholesterol depletion enhances influenza A virus budding from MDCK cells. *J Virol,* 81**,** 12169-78.

BARNARD, K. N., WASIK, B. R., LACLAIR, J. R., BUCHHOLZ, D. W., WEICHERT, W. S., ALFORD-LAWRENCE, B. K., AGUILAR, H. C. & PARRISH, C. R. 2019. Expression of 9-O- and 7,9-O-Acetyl Modified Sialic Acid in Cells and Their Effects on Influenza Viruses. *mBio,* 10.

BAUDIN, F., PETIT, I., WEISSENHORN, W. & RUIGROK, R. W. 2001. In vitro dissection of the membrane and RNP binding activities of influenza virus M1 protein. *Virology,* 281**,** 102-8.

BEALE, R., WISE, H., STUART, A., RAVENHILL, B. J., DIGARD, P. & RANDOW, F. 2014. A LC3-interacting motif in the influenza A virus M2 protein is required to subvert autophagy and maintain virion stability. *Cell Host Microbe,* 15**,** 239-47.

BIALAS, K. M., BUSSEY, K. A., STONE, R. L. & TAKIMOTO, T. 2014. Specific nucleoprotein residues affect influenza virus morphology. *J Virol,* 88**,** 2227-34.

BIALAS, K. M., DESMET, E. A. & TAKIMOTO, T. 2012. Specific residues in the 2009 H1N1 swine-origin influenza matrix protein influence virion morphology and efficiency of viral spread in vitro. *PLoS One,* 7**,** e50595.

BLUMENKRANTZ, D., ROBERTS, K. L., SHELTON, H., LYCETT, S. & BARCLAY, W. S. 2013. The short stalk length of highly pathogenic avian influenza H5N1 virus neuraminidase limits transmission of pandemic H1N1 virus in ferrets. *J Virol,* 87**,** 10539-51.

BOS, T. J., DAVIS, A. R. & NAYAK, D. P. 1984. NH2-terminal hydrophobic region of influenza virus neuraminidase provides the signal function in translocation. *Proc Natl Acad Sci U S A,* 81**,** 2327-31.

BOULO, S., AKARSU, H., RUIGROK, R. W. & BAUDIN, F. 2007. Nuclear traffic of influenza virus proteins and ribonucleoprotein complexes. *Virus Res,* 124**,** 12-21.

BOURMAKINA, S. V. & GARCIA-SASTRE, A. 2003. Reverse genetics studies on the filamentous morphology of influenza A virus. *J Gen Virol,* 84**,** 517-527.
BROOKE, C. B. 2014. Biological activities of 'noninfectious' influenza A virus particles. *Future Virol,* 9**,** 41-51.
BROOKE, C. B., INCE, W. L., WRAMMERT, J., AHMED, R., WILSON, P. C., BENNINK, J. R. & YEWDELL, J. W. 2013. Most influenza a virions fail to express at least one essential viral protein. *J Virol,* 87**,** 3155-62.
BRUCE, E. A., DIGARD, P. & STUART, A. D. 2010. The Rab11 pathway is required for influenza A virus budding and filament formation. *J Virol,* 84**,** 5848-59.
BRYANT, N. A., RASH, A. S., RUSSELL, C. A., ROSS, J., COOKE, A., BOWMAN, S., MACRAE, S., LEWIS, N. S., PAILLOT, R., ZANONI, R., MEIER, H., GRIFFITHS, L. A., DALY, J. M., TIWARI, A., CHAMBERS, T. M., NEWTON, J. R. & ELTON, D. M. 2009. Antigenic and genetic variations in European and North American equine influenza virus strains (H3N8) isolated from 2006 to 2007. *Vet Microbiol,* 138**,** 41-52.
BRYANT, N. A., RASH, A. S., WOODWARD, A. L., MEDCALF, E., HELWEGEN, M., WOHLFENDER, F., CRUZ, F., HERRMANN, C., BORCHERS, K., TIWARI, A., CHAMBERS, T. M., NEWTON, J. R., MUMFORD, J. A. & ELTON, D. M. 2011. Isolation and characterisation of equine influenza viruses (H3N8) from Europe and North America from 2008 to 2009. *Vet Microbiol,* 147**,** 19-27.
BUI, M., WHITTAKER, G. & HELENIUS, A. 1996. Effect of M1 protein and low pH on nuclear transport of influenza virus ribonucleoproteins. *J Virol,* 70**,** 8391-401.
BURLEIGH, L. M., CALDER, L. J., SKEHEL, J. J. & STEINHAUER, D. A. 2005. Influenza a viruses with mutations in the m1 helix six domain display a wide variety of morphological phenotypes. *J Virol,* 79**,** 1262-70.
CALDER, L. J., WASILEWSKI, S., BERRIMAN, J. A. & ROSENTHAL, P. B. 2010. Structural organization of a filamentous influenza A virus. *Proc Natl Acad Sci U S A,* 107**,** 10685-90.
CAMPBELL, P. J., DANZY, S., KYRIAKIS, C. S., DEYMIER, M. J., LOWEN, A. C. & STEEL, J. 2014. The M segment of the 2009 pandemic influenza virus confers increased neuraminidase activity, filamentous morphology, and efficient contact transmissibility to A/Puerto Rico/8/1934-based reassortant viruses. *J Virol,* 88**,** 3802-14.
CASPAR, D. L. 1963. Assembly and Stability of the Tobacco Mosaic Virus Particle. *Adv Protein Chem,* 18**,** 37-121.
CENTERS FOR DISEASE CONTROL AND PREVENTION, N. C. F. I. A. R. D. N. 2019. *Types of Influenza Viruses* [Online]. [Accessed 11/1/2021 2021].
CHANDRASEKARAN, A., SRINIVASAN, A., RAMAN, R., VISWANATHAN, K., RAGURAM, S., TUMPEY, T. M., SASISEKHARAN, V. & SASISEKHARAN, R. 2008. Glycan topology determines human adaptation of avian H5N1 virus hemagglutinin. *Nat Biotechnol,* 26**,** 107-13.
CHAUCHE, C., NOGALES, A., ZHU, H., GOLDFARB, D., AHMAD SHANIZZA, A. I., GU, Q., PARRISH, C. R., MARTINEZ-SOBRIDO, L., MARSHALL, J. F. & MURCIA, P. R. 2018. Mammalian Adaptation of an Avian Influenza A Virus Involves Stepwise Changes in NS1. *J Virol,* 92.
CHEN, B. J., LESER, G. P., JACKSON, D. & LAMB, R. A. 2008. The influenza virus M2 protein cytoplasmic tail interacts with the M1 protein and influences virus assembly at the site of virus budding. *J Virol,* 82**,** 10059-70.
CHEN, B. J., LESER, G. P., MORITA, E. & LAMB, R. A. 2007. Influenza virus hemagglutinin and neuraminidase, but not the matrix protein, are required for assembly and budding of plasmid-derived virus-like particles. *J Virol,* 81**,** 7111-23.
CHEN, W., CALVO, P. A., MALIDE, D., GIBBS, J., SCHUBERT, U., BACIK, I., BASTA, S., O'NEILL, R., SCHICKLI, J., PALESE, P., HENKLEIN, P., BENNINK, J. R. & YEWDELL, J. W. 2001. A novel influenza A virus mitochondrial protein that induces cell death. *Nat Med,* 7**,** 1306-12.
CHLANDA, P., SCHRAIDT, O., KUMMER, S., RICHES, J., OBERWINKLER, H., PRINZ, S., KRAUSSLICH, H. G. & BRIGGS, J. A. 2015. Structural Analysis of the Roles of Influenza A Virus Membrane-Associated Proteins in Assembly and Morphology. *J Virol,* 89**,** 8957-66.
CHOU, Y. Y., HEATON, N. S., GAO, Q., PALESE, P., SINGER, R. H. & LIONNET, T. 2013. Colocalization of different influenza viral RNA segments in the cytoplasm before viral budding as shown by single-molecule sensitivity FISH analysis. *PLoS Pathog,* 9**,** e1003358.
CHU, C. M., DAWSON, I. M. & ELFORD, W. J. 1949. Filamentous forms associated with newly isolated influenza virus. *Lancet,* 1**,** 602.
COLLINS, P. J., VACHIERI, S. G., HAIRE, L. F., OGRODOWICZ, R. W., MARTIN, S. R., WALKER, P. A., XIONG, X., GAMBLIN, S. J. & SKEHEL, J. J. 2014. Recent evolution of

equine influenza and the origin of canine influenza. *Proc Natl Acad Sci U S A,* 111**,** 11175-80.
COUZENS, L., GAO, J., WESTGEEST, K., SANDBULTE, M., LUGOVTSEV, V., FOUCHIER, R. & EICHELBERGER, M. 2014. An optimized enzyme-linked lectin assay to measure influenza A virus neuraminidase inhibition antibody titers in human sera. *J Virol Methods,* 210**,** 7-14.
CRISPELL, J. L. & UNIVERSITY OF GLASGOW *Investigating equine host barriers to infection with influenza A viruses*.
CROS, J. F., GARCIA-SASTRE, A. & PALESE, P. 2005. An unconventional NLS is critical for the nuclear import of the influenza A virus nucleoprotein and ribonucleoprotein. *Traffic,* 6**,** 205-13.
DADONAITE, B., GILBERTSON, B., KNIGHT, M. L., TRIFKOVIC, S., ROCKMAN, S., LAEDERACH, A., BROWN, L. E., FODOR, E. & BAUER, D. L. V. 2019. The structure of the influenza A virus genome. *Nat Microbiol,* 4**,** 1781-1789.
DADONAITE, B., VIJAYAKRISHNAN, S., FODOR, E., BHELLA, D. & HUTCHINSON, E. C. 2016. Filamentous influenza viruses. *J Gen Virol,* 97**,** 1755-1764.
DALY, J. M., LAI, A. C., BINNS, M. M., CHAMBERS, T. M., BARRANDEGUY, M. & MUMFORD, J. A. 1996. Antigenic and genetic evolution of equine H3N8 influenza A viruses. *J Gen Virol,* 77 (Pt 4)**,** 661-71.
DALY, J. M., MACRAE, S., NEWTON, J. R., WATTRANG, E. & ELTON, D. M. 2011. Equine influenza: a review of an unpredictable virus. *Vet J,* 189**,** 7-14.
DAMIANI, A. M., SCICLUNA, M. T., CIABATTI, I., CARDETI, G., SALA, M., VULCANO, G., CORDIOLI, P., MARTELLA, V., AMADDEO, D. & AUTORINO, G. L. 2008. Genetic characterization of equine influenza viruses isolated in Italy between 1999 and 2005. *Virus Res,* 131**,** 100-5.
DANEV, R., BUIJSSE, B., KHOSHOUEI, M., PLITZKO, J. M. & BAUMEISTER, W. 2014. Volta potential phase plate for in-focus phase contrast transmission electron microscopy. *Proc Natl Acad Sci U S A,* 111**,** 15635-40.
DANIELS, R., KUROWSKI, B., JOHNSON, A. E. & HEBERT, D. N. 2003. N-linked glycans direct the cotranslational folding pathway of influenza hemagglutinin. *Mol Cell,* 11**,** 79-90.
DE CASTRO MARTIN, I. F., FOURNIER, G., SACHSE, M., PIZARRO-CERDA, J., RISCO, C. & NAFFAKH, N. 2017. Influenza virus genome reaches the plasma membrane via a modified endoplasmic reticulum and Rab11-dependent vesicles. *Nat Commun,* 8**,** 1396.
DE VLUGT, C., SIKORA, D. & PELCHAT, M. 2018. Insight into Influenza: A Virus Cap-Snatching. *Viruses,* 10.
DIAS, A., BOUVIER, D., CREPIN, T., MCCARTHY, A. A., HART, D. J., BAUDIN, F., CUSACK, S. & RUIGROK, R. W. 2009. The cap-snatching endonuclease of influenza virus polymerase resides in the PA subunit. *Nature,* 458**,** 914-8.
DIONISIO, L., MEDEIROS, F., PEQUITO, M. & FAUSTINO-ROCHA, A. I. 2021. Equine influenza: a comprehensive review from etiology to treatment. *Anim Health Res Rev,* 22**,** 56-71.
DOU, D., DA SILVA, D. V., NORDHOLM, J., WANG, H. & DANIELS, R. 2014. Type II transmembrane domain hydrophobicity dictates the cotranslational dependence for inversion. *Mol Biol Cell,* 25**,** 3363-74.
DUBOIS, J., TERRIER, O. & ROSA-CALATRAVA, M. 2014. Influenza viruses and mRNA splicing: doing more with less. *mBio,* 5**,** e00070-14.
EISFELD, A. J., KAWAKAMI, E., WATANABE, T., NEUMANN, G. & KAWAOKA, Y. 2011. RAB11A is essential for transport of the influenza virus genome to the plasma membrane. *J Virol,* 85**,** 6117-26.
ELLEMAN, C. J. & BARCLAY, W. S. 2004. The M1 matrix protein controls the filamentous phenotype of influenza A virus. *Virology,* 321**,** 144-53.
ELTON, D., BRUCE, E. A., BRYANT, N., WISE, H. M., MACRAE, S., RASH, A., SMITH, N., TURNBULL, M. L., MEDCALF, L., DALY, J. M. & DIGARD, P. 2013. The genetics of virus particle shape in equine influenza A virus. *Influenza Other Respir Viruses,* 7 Suppl 4**,** 81-9.
ELTON, D. & BRYANT, N. 2011. Facing the threat of equine influenza. *Equine Vet J,* 43**,** 250-8.
FONVILLE, J. M., MARSHALL, N., TAO, H., STEEL, J. & LOWEN, A. C. 2015. Influenza Virus Reassortment Is Enhanced by Semi-infectious Particles but Can Be Suppressed by Defective Interfering Particles. *PLoS Pathog,* 11**,** e1005204.
FRIEDMAN, J. R., WEBSTER, B. M., MASTRONARDE, D. N., VERHEY, K. J. & VOELTZ, G. K. 2010. ER sliding dynamics and ER-mitochondrial contacts occur on acetylated microtubules. *J Cell Biol,* 190**,** 363-75.
GABRIEL, G., HERWIG, A. & KLENK, H. D. 2008. Interaction of polymerase subunit PB2 and NP with importin alpha1 is a determinant of host range of influenza A virus. *PLoS Pathog,* 4**,** e11.

GABRIEL, G., KLINGEL, K., OTTE, A., THIELE, S., HUDJETZ, B., ARMAN-KALCEK, G., SAUTER, M., SHMIDT, T., ROTHER, F., BAUMGARTE, S., KEINER, B., HARTMANN, E., BADER, M., BROWNLEE, G. G., FODOR, E. & KLENK, H. D. 2011. Differential use of importin-alpha isoforms governs cell tropism and host adaptation of influenza virus. *Nat Commun,* 2**,** 156.

GALLOWAY, S. E., REED, M. L., RUSSELL, C. J. & STEINHAUER, D. A. 2013. Influenza HA subtypes demonstrate divergent phenotypes for cleavage activation and pH of fusion: implications for host range and adaptation. *PLoS Pathog,* 9**,** e1003151.

GARNER, M. G., SCANLAN, W. A., COWLED, B. D. & CARROLL, A. 2011. Regaining Australia's equine influenza-free status: a national perspective. *Aust Vet J,* 89 Suppl 1**,** 169-73.

GHOSAL, D., KAPLAN, M., CHANG, Y. W. & JENSEN, G. J. 2019. In Situ Imaging and Structure Determination of Bacterial Toxin Delivery Systems Using Electron Cryotomography. *Methods Mol Biol,* 1921**,** 249-265.

GOMEZ-PUERTAS, P., ALBO, C., PEREZ-PASTRANA, E., VIVO, A. & PORTELA, A. 2000. Influenza virus matrix protein is the major driving force in virus budding. *J Virol,* 74**,** 11538-47.

GORLICH, D., PREHN, S., HARTMANN, E., KALIES, K. U. & RAPOPORT, T. A. 1992. A mammalian homolog of SEC61p and SECYp is associated with ribosomes and nascent polypeptides during translocation. *Cell,* 71**,** 489-503.

GRANTHAM, M. L., STEWART, S. M., LALIME, E. N. & PEKOSZ, A. 2010. Tyrosines in the influenza A virus M2 protein cytoplasmic tail are critical for production of infectious virus particles. *J Virol,* 84**,** 8765-76.

GRIMM, L. H., KELLY, S., KRULL, R. & HEMPEL, D. C. 2005. Morphology and productivity of filamentous fungi. *Appl Microbiol Biotechnol,* 69**,** 375-84.

GUO, H., RABOUW, H., SLOMP, A., DAI, M., VAN DER VEGT, F., VAN LENT, J. W. M., MCBRIDE, R., PAULSON, J. C., DE GROOT, R. J., VAN KUPPEVELD, F. J. M., DE VRIES, E. & DE HAAN, C. A. M. 2018. Kinetic analysis of the influenza A virus HA/NA balance reveals contribution of NA to virus-receptor binding and NA-dependent rolling on receptor-containing surfaces. *PLoS Pathog,* 14**,** e1007233.

HAGEN, W. J. H., WAN, W. & BRIGGS, J. A. G. 2017. Implementation of a cryo-electron tomography tilt-scheme optimized for high resolution subtomogram averaging. *J Struct Biol,* 197**,** 191-198.

HAMPTON, C. M., STRAUSS, J. D., KE, Z., DILLARD, R. S., HAMMONDS, J. E., ALONAS, E., DESAI, T. M., MARIN, M., STORMS, R. E., LEON, F., MELIKYAN, G. B., SANTANGELO, P. J., SPEARMAN, P. W. & WRIGHT, E. R. 2017. Correlated fluorescence microscopy and cryo-electron tomography of virus-infected or transfected mammalian cells. *Nat Protoc,* 12**,** 150-167.

HARRIS, A., CARDONE, G., WINKLER, D. C., HEYMANN, J. B., BRECHER, M., WHITE, J. M. & STEVEN, A. C. 2006. Influenza virus pleiomorphy characterized by cryoelectron tomography. *Proc Natl Acad Sci U S A,* 103**,** 19123-7.

HESS, S. T., KUMAR, M., VERMA, A., FARRINGTON, J., KENWORTHY, A. & ZIMMERBERG, J. 2005. Quantitative electron microscopy and fluorescence spectroscopy of the membrane distribution of influenza hemagglutinin. *J Cell Biol,* 169**,** 965-76.

HESSA, T., MEINDL-BEINKER, N. M., BERNSEL, A., KIM, H., SATO, Y., LERCH-BADER, M., NILSSON, I., WHITE, S. H. & VON HEIJNE, G. 2007. Molecular code for transmembrane-helix recognition by the Sec61 translocon. *Nature,* 450**,** 1026-30.

HILSCH, M., GOLDENBOGEN, B., SIEBEN, C., HOFER, C. T., RABE, J. P., KLIPP, E., HERRMANN, A. & CHIANTIA, S. 2014. Influenza A matrix protein M1 multimerizes upon binding to lipid membranes. *Biophys J,* 107**,** 912-23.

HOFACKER, I. L. & LORENZ, R. 2014. Predicting RNA structure: advances and limitations. *Methods Mol Biol,* 1086**,** 1-19.

HOLSINGER, L. J. & LAMB, R. A. 1991. Influenza virus M2 integral membrane protein is a homotetramer stabilized by formation of disulfide bonds. *Virology,* 183**,** 32-43.

HOWLEY, P. M., KNIPE, D. M., WHELAN, S. & OVID TECHNOLOGIES INC. 2021. Fields virology. Volume 1, Emerging viruses. 7th ed. Philadelphia: Wolters Kluwer,.

HUANG, S., CHEN, J., CHEN, Q., WANG, H., YAO, Y., CHEN, J. & CHEN, Z. 2013. A second CRM1-dependent nuclear export signal in the influenza A virus NS2 protein contributes to the nuclear export of viral ribonucleoproteins. *J Virol,* 87**,** 767-78.

HUGHES, J., ALLEN, R. C., BAGUELIN, M., HAMPSON, K., BAILLIE, G. J., ELTON, D., NEWTON, J. R., KELLAM, P., WOOD, J. L., HOLMES, E. C. & MURCIA, P. R. 2012. Transmission of equine influenza virus during an outbreak is characterized by frequent mixed infections and loose transmission bottlenecks. *PLoS Pathog,* 8**,** e1003081.

HULL, J. D., GILMORE, R. & LAMB, R. A. 1988. Integration of a small integral membrane protein, M2, of influenza virus into the endoplasmic reticulum: analysis of the internal signal-anchor domain of a protein with an ectoplasmic NH2 terminus. *J Cell Biol,* 106**,** 1489-98.

HUTCHINSON, E. C., CHARLES, P. D., HESTER, S. S., THOMAS, B., TRUDGIAN, D., MARTINEZ-ALONSO, M. & FODOR, E. 2014. Conserved and host-specific features of influenza virion architecture. *Nat Commun,* 5**,** 4816.

HUTCHINSON, E. C. & FODOR, E. 2013. Transport of the influenza virus genome from nucleus to nucleus. *Viruses,* 5**,** 2424-46.

IMAI, M., WATANABE, T., HATTA, M., DAS, S. C., OZAWA, M., SHINYA, K., ZHONG, G., HANSON, A., KATSURA, H., WATANABE, S., LI, C., KAWAKAMI, E., YAMADA, S., KISO, M., SUZUKI, Y., MAHER, E. A., NEUMANN, G. & KAWAOKA, Y. 2012. Experimental adaptation of an influenza H5 HA confers respiratory droplet transmission to a reassortant H5 HA/H1N1 virus in ferrets. *Nature,* 486**,** 420-8.

ITO, T., SUZUKI, Y., SUZUKI, T., TAKADA, A., HORIMOTO, T., WELLS, K., KIDA, H., OTSUKI, K., KISO, M., ISHIDA, H. & KAWAOKA, Y. 2000. Recognition of N-glycolylneuraminic acid linked to galactose by the alpha2,3 linkage is associated with intestinal replication of influenza A virus in ducks. *J Virol,* 74**,** 9300-5.

ITOH, Y., SHINYA, K., KISO, M., WATANABE, T., SAKODA, Y., HATTA, M., MURAMOTO, Y., TAMURA, D., SAKAI-TAGAWA, Y., NODA, T., SAKABE, S., IMAI, M., HATTA, Y., WATANABE, S., LI, C., YAMADA, S., FUJII, K., MURAKAMI, S., IMAI, H., KAKUGAWA, S., ITO, M., TAKANO, R., IWATSUKI-HORIMOTO, K., SHIMOJIMA, M., HORIMOTO, T., GOTO, H., TAKAHASHI, K., MAKINO, A., ISHIGAKI, H., NAKAYAMA, M., OKAMATSU, M., TAKAHASHI, K., WARSHAUER, D., SHULT, P. A., SAITO, R., SUZUKI, H., FURUTA, Y., YAMASHITA, M., MITAMURA, K., NAKANO, K., NAKAMURA, M., BROCKMAN-SCHNEIDER, R., MITAMURA, H., YAMAZAKI, M., SUGAYA, N., SURESH, M., OZAWA, M., NEUMANN, G., GERN, J., KIDA, H., OGASAWARA, K. & KAWAOKA, Y. 2009. In vitro and in vivo characterization of new swine-origin H1N1 influenza viruses. *Nature,* 460**,** 1021-5.

IWATSUKI-HORIMOTO, K., HORIMOTO, T., FUJII, Y. & KAWAOKA, Y. 2004. Generation of influenza A virus NS2 (NEP) mutants with an altered nuclear export signal sequence. *J Virol,* 78**,** 10149-55.

JIN, H., LESER, G. P. & LAMB, R. A. 1994. The influenza virus hemagglutinin cytoplasmic tail is not essential for virus assembly or infectivity. *EMBO J,* 13**,** 5504-15.

JIN, H., LESER, G. P., ZHANG, J. & LAMB, R. A. 1997. Influenza virus hemagglutinin and neuraminidase cytoplasmic tails control particle shape. *EMBO J,* 16**,** 1236-47.

JORBA, N., COLOMA, R. & ORTIN, J. 2009. Genetic trans-complementation establishes a new model for influenza virus RNA transcription and replication. *PLoS Pathog,* 5**,** e1000462.

KARAMENDIN, K., KYDYRMANOV, A., SAYATOV, M., STROCHKOV, V., SANDYBAYEV, N. & SULTANKULOVA, K. 2016. Retrospective Analysis of the Equine Influenza Virus A/Equine/Kirgizia/26/1974 (H7N7) Isolated in Central Asia. *Pathogens,* 5.

KAWAOKA, Y., BEAN, W. J. & WEBSTER, R. G. 1989. Evolution of the hemagglutinin of equine H3 influenza viruses. *Virology,* 169**,** 283-92.

KE, Z., DILLARD, R. S., CHIRKOVA, T., LEON, F., STOBART, C. C., HAMPTON, C. M., STRAUSS, J. D., RAJAN, D., ROSTAD, C. A., TAYLOR, J. V., YI, H., SHAH, R., JIN, M., HARTERT, T. V., PEEBLES, R. S., JR., GRAHAM, B. S., MOORE, M. L., ANDERSON, L. J. & WRIGHT, E. R. 2018. The Morphology and Assembly of Respiratory Syncytial Virus Revealed by Cryo-Electron Tomography. *Viruses,* 10.

KITCHEN, R. H., KEHLER, W. H. & HENTHORNE, J. C. 1963. The 1963 Equine Influenza Epizootic. *J Am Vet Med Assoc,* 143**,** 1108-10.

KOREN, C. W. R., AND A. NYLUND 1997. Morphology and morphogenesis of infectious salmon anaemia virus replicating in the endothelium of Atlantic salmon Salmo salar. *Diseases of aquatic organisms,* 29**,** 10.

KREMER, J. R., MASTRONARDE, D. N. & MCINTOSH, J. R. 1996. Computer visualization of three-dimensional image data using IMOD. *J Struct Biol,* 116**,** 71-6.

LAI, A. C., ROGERS, K. M., GLASER, A., TUDOR, L. & CHAMBERS, T. 2004. Alternate circulation of recent equine-2 influenza viruses (H3N8) from two distinct lineages in the United States. *Virus Res,* 100**,** 159-64.

LAKDAWALA, S. S., WU, Y., WAWRZUSIN, P., KABAT, J., BROADBENT, A. J., LAMIRANDE, E. W., FODOR, E., ALTAN-BONNET, N., SHROFF, H. & SUBBARAO, K. 2014. Influenza a virus assembly intermediates fuse in the cytoplasm. *PLoS Pathog,* 10**,** e1003971.

LAMB, R. A., LAI, C. J. & CHOPPIN, P. W. 1981. Sequences of mRNAs derived from genome RNA segment 7 of influenza virus: colinear and interrupted mRNAs code for overlapping proteins. *Proc Natl Acad Sci U S A,* 78**,** 4170-4.

LANDOLT, G. A. 2014. Equine influenza virus. *Vet Clin North Am Equine Pract,* 30**,** 507-22.
LE SAGE, V., KANAREK, J. P., SNYDER, D. J., COOPER, V. S., LAKDAWALA, S. S. & LEE, N. 2020. Mapping of Influenza Virus RNA-RNA Interactions Reveals a Flexible Network. *Cell Rep,* 31**,** 107823.
LESER, G. P. & LAMB, R. A. 2005. Influenza virus assembly and budding in raft-derived microdomains: a quantitative analysis of the surface distribution of HA, NA and M2 proteins. *Virology,* 342**,** 215-27.
LESER, G. P. & LAMB, R. A. 2017. Lateral Organization of Influenza Virus Proteins in the Budozone Region of the Plasma Membrane. *J Virol,* 91.
LEWIS, N. S., DALY, J. M., RUSSELL, C. A., HORTON, D. L., SKEPNER, E., BRYANT, N. A., BURKE, D. F., RASH, A. S., WOOD, J. L., CHAMBERS, T. M., FOUCHIER, R. A., MUMFORD, J. A., ELTON, D. M. & SMITH, D. J. 2011. Antigenic and genetic evolution of equine influenza A (H3N8) virus from 1968 to 2007. *J Virol,* 85**,** 12742-9.
LIU, T., MULLER, J. & YE, Z. 2002. Association of influenza virus matrix protein with ribonucleoproteins may control viral growth and morphology. *Virology,* 304**,** 89-96.
LONG, J. S., GIOTIS, E. S., MONCORGE, O., FRISE, R., MISTRY, B., JAMES, J., MORISSON, M., IQBAL, M., VIGNAL, A., SKINNER, M. A. & BARCLAY, W. S. 2016. Species difference in ANP32A underlies influenza A virus polymerase host restriction. *Nature,* 529**,** 101-4.
LORENZ, R., BERNHART, S. H., HONER ZU SIEDERDISSEN, C., TAFER, H., FLAMM, C., STADLER, P. F. & HOFACKER, I. L. 2011. ViennaRNA Package 2.0. *Algorithms Mol Biol,* 6**,** 26.
LU, Z., DUBOVI, E. J., ZYLICH, N. C., CRAWFORD, P. C., SELLS, S., GO, Y. Y., LOYNACHAN, A. T., TIMONEY, P. J., CHAMBERS, T. M. & BALASURIYA, U. B. 2010. Diagnostic application of H3N8-specific equine influenza real-time reverse transcription polymerase chain reaction assays for the detection of Canine influenza virus in clinical specimens. *J Vet Diagn Invest,* 22**,** 942-5.
MA, E. J., HILL, N. J., ZABILANSKY, J., YUAN, K. & RUNSTADLER, J. A. 2016. Reticulate evolution is favored in influenza niche switching. *Proc Natl Acad Sci U S A,* 113**,** 5335-9.
MAHAMID, J., PFEFFER, S., SCHAFFER, M., VILLA, E., DANEV, R., CUELLAR, L. K., FORSTER, F., HYMAN, A. A., PLITZKO, J. M. & BAUMEISTER, W. 2016. Visualizing the molecular sociology at the HeLa cell nuclear periphery. *Science,* 351**,** 969-72.
MANZ, B., BRUNOTTE, L., REUTHER, P. & SCHWEMMLE, M. 2012. Adaptive mutations in NEP compensate for defective H5N1 RNA replication in cultured human cells. *Nat Commun,* 3**,** 802.
MARCUS, P. I., NGUNJIRI, J. M. & SEKELLICK, M. J. 2009. Dynamics of biologically active subpopulations of influenza virus: plaque-forming, noninfectious cell-killing, and defective interfering particles. *J Virol,* 83**,** 8122-30.
MARTIN, K. & HELENIUS, A. 1991. Nuclear transport of influenza virus ribonucleoproteins: the viral matrix protein (M1) promotes export and inhibits import. *Cell,* 67**,** 117-30.
MARTYNOWYCZ, M. W., CLABBERS, M. T. B., UNGE, J., HATTNE, J. & GONEN, T. 2021. Benchmarking the ideal sample thickness in cryo-EM. *Proceedings of the National Academy of Sciences,* 118**,** e2108884118.
MATLIN, K. S., REGGIO, H., HELENIUS, A. & SIMONS, K. 1981. Infectious entry pathway of influenza virus in a canine kidney cell line. *J Cell Biol,* 91**,** 601-13.
MATROSOVICH, M. N., GAMBARYAN, A. S., TUZIKOV, A. B., BYRAMOVA, N. E., MOCHALOVA, L. V., GOLBRAIKH, A. A., SHENDEROVICH, M. D., FINNE, J. & BOVIN, N. V. 1993. Probing of the receptor-binding sites of the H1 and H3 influenza A and influenza B virus hemagglutinins by synthetic and natural sialosides. *Virology,* 196**,** 111-21.
MATROSOVICH, M. N., MATROSOVICH, T. Y., GRAY, T., ROBERTS, N. A. & KLENK, H. D. 2004. Human and avian influenza viruses target different cell types in cultures of human airway epithelium. *Proc Natl Acad Sci U S A,* 101**,** 4620-4.
MCAULEY, J. L., GILBERTSON, B. P., TRIFKOVIC, S., BROWN, L. E. & MCKIMM-BRESCHKIN, J. L. 2019. Influenza Virus Neuraminidase Structure and Functions. *Front Microbiol,* 10**,** 39.
MCCOWN, M. F. & PEKOSZ, A. 2005. The influenza A virus M2 cytoplasmic tail is required for infectious virus production and efficient genome packaging. *J Virol,* 79**,** 3595-605.
MCCOWN, M. F. & PEKOSZ, A. 2006. Distinct domains of the influenza a virus M2 protein cytoplasmic tail mediate binding to the M1 protein and facilitate infectious virus production. *J Virol,* 80**,** 8178-89.
MIBAYASHI, M., MARTINEZ-SOBRIDO, L., LOO, Y. M., CARDENAS, W. B., GALE, M., JR. & GARCIA-SASTRE, A. 2007. Inhibition of retinoic acid-inducible gene I-mediated induction of beta interferon by the NS1 protein of influenza A virus. *J Virol,* 81**,** 514-24.
MITNAUL, L. J., CASTRUCCI, M. R., MURTI, K. G. & KAWAOKA, Y. 1996. The cytoplasmic tail of influenza A virus neuraminidase (NA) affects NA incorporation into virions, virion

morphology, and virulence in mice but is not essential for virus replication. *J Virol,* 70**,** 873-9.
MOMOSE, F., KIKUCHI, Y., KOMASE, K. & MORIKAWA, Y. 2007. Visualization of microtubule-mediated transport of influenza viral progeny ribonucleoprotein. *Microbes Infect,* 9**,** 1422-33.
MURAMOTO, Y., NODA, T., KAWAKAMI, E., AKKINA, R. & KAWAOKA, Y. 2013. Identification of novel influenza A virus proteins translated from PA mRNA. *J Virol,* 87**,** 2455-62.
MURCIA, P. R., BAILLIE, G. J., DALY, J., ELTON, D., JERVIS, C., MUMFORD, J. A., NEWTON, R., PARRISH, C. R., HOELZER, K., DOUGAN, G., PARKHILL, J., LENNARD, N., ORMOND, D., MOULE, S., WHITWHAM, A., MCCAULEY, J. W., MCKINLEY, T. J., HOLMES, E. C., GRENFELL, B. T. & WOOD, J. L. 2010. Intra- and interhost evolutionary dynamics of equine influenza virus. *J Virol,* 84**,** 6943-54.
MURCIA, P. R., WOOD, J. L. & HOLMES, E. C. 2011. Genome-scale evolution and phylodynamics of equine H3N8 influenza A virus. *J Virol,* 85**,** 5312-22.
MURPHY, R. F. 1991. Maturation models for endosome and lysosome biogenesis. *Trends Cell Biol,* 1**,** 77-82.
NAKATSU, S., MURAKAMI, S., SHINDO, K., HORIMOTO, T., SAGARA, H., NODA, T. & KAWAOKA, Y. 2018. Influenza C and D Viruses Package Eight Organized Ribonucleoprotein Complexes. *J Virol,* 92.
NEUMANN, G., HUGHES, M. T. & KAWAOKA, Y. 2000. Influenza A virus NS2 protein mediates vRNP nuclear export through NES-independent interaction with hCRM1. *EMBO J,* 19**,** 6751-8.
NODA, T. & KAWAOKA, Y. 2010. Structure of influenza virus ribonucleoprotein complexes and their packaging into virions. *Rev Med Virol,* 20**,** 380-91.
NODA, T., SAGARA, H., SUZUKI, E., TAKADA, A., KIDA, H. & KAWAOKA, Y. 2002. Ebola virus VP40 drives the formation of virus-like filamentous particles along with GP. *J Virol,* 76**,** 4855-65.
NODA, T., SAGARA, H., YEN, A., TAKADA, A., KIDA, H., CHENG, R. H. & KAWAOKA, Y. 2006. Architecture of ribonucleoprotein complexes in influenza A virus particles. *Nature,* 439**,** 490-2.
NODA, T., SUGITA, Y., AOYAMA, K., HIRASE, A., KAWAKAMI, E., MIYAZAWA, A., SAGARA, H. & KAWAOKA, Y. 2012. Three-dimensional analysis of ribonucleoprotein complexes in influenza A virus. *Nat Commun,* 3**,** 639.
O'NEILL, R. E., TALON, J. & PALESE, P. 1998. The influenza virus NEP (NS2 protein) mediates the nuclear export of viral ribonucleoproteins. *EMBO J,* 17**,** 288-96.
OHKURA, T., MOMOSE, F., ICHIKAWA, R., TAKEUCHI, K. & MORIKAWA, Y. 2014. Influenza A virus hemagglutinin and neuraminidase mutually accelerate their apical targeting through clustering of lipid rafts. *J Virol,* 88**,** 10039-55.
PAILLOT, R., PITEL, P. H., PRONOST, S., LEGRAND, L., FOUGEROLLE, S., JOURDAN, M. & MARCILLAUD-PITEL, C. 2019. Florida clade 1 equine influenza virus in France. *Vet Rec,* 184**,** 101.
PARRISH, C. R. & KAWAOKA, Y. 2005. The origins of new pandemic viruses: the acquisition of new host ranges by canine parvovirus and influenza A viruses. *Annu Rev Microbiol,* 59**,** 553-86.
PARRISH, C. R., MURCIA, P. R. & HOLMES, E. C. 2015. Influenza virus reservoirs and intermediate hosts: dogs, horses, and new possibilities for influenza virus exposure of humans. *J Virol,* 89**,** 2990-4.
PEUKES, J., XIONG, X., ERLENDSSON, S., QU, K., WAN, W., CALDER, L. J., SCHRAIDT, O., KUMMER, S., FREUND, S. M. V., KRAUSSLICH, H. G. & BRIGGS, J. A. G. 2020. The native structure of the assembled matrix protein 1 of influenza A virus. *Nature,* 587**,** 495-498.
PFEFFER, C., LARSEN, S., SONG, J., DONG, M., BESENBACHER, F., MEYER, R. L., KJELDSEN, K. U., SCHREIBER, L., GORBY, Y. A., EL-NAGGAR, M. Y., LEUNG, K. M., SCHRAMM, A., RISGAARD-PETERSEN, N. & NIELSEN, L. P. 2012. Filamentous bacteria transport electrons over centimetre distances. *Nature,* 491**,** 218-21.
POLILOV, A. A., MAKAROVA, A. A., PANG, S., SHAN XU, C. & HESS, H. 2021. Protocol for preparation of heterogeneous biological samples for 3D electron microscopy: a case study for insects. *Sci Rep,* 11**,** 4717.
POON, L. L., PRITLOVE, D. C., SHARPS, J. & BROWNLEE, G. G. 1998. The RNA polymerase of influenza virus, bound to the 5' end of virion RNA, acts in cis to polyadenylate mRNA. *J Virol,* 72**,** 8214-9.
RASH, A. 2017. Diagnosis of equine influenza. *Vet Rec,* 181**,** 113-114.

REICH, S., GUILLIGAY, D., PFLUG, A., MALET, H., BERGER, I., CREPIN, T., HART, D., LUNARDI, T., NANAO, M., RUIGROK, R. W. & CUSACK, S. 2014. Structural insight into cap-snatching and RNA synthesis by influenza polymerase. *Nature,* 516**,** 361-6.
ROBERTS, P. C. & COMPANS, R. W. 1998. Host cell dependence of viral morphology. *Proc Natl Acad Sci U S A,* 95**,** 5746-51.
ROBERTS, P. C., LAMB, R. A. & COMPANS, R. W. 1998. The M1 and M2 proteins of influenza A virus are important determinants in filamentous particle formation. *Virology,* 240**,** 127-37.
ROSANOWSKI, S. M., CARPENTER, T. E., ADAMSON, D., ROGERS, C. W., PEARCE, P., BURNS, M. & COGGER, N. 2019. An economic analysis of a contingency model utilising vaccination for the control of equine influenza in a non-endemic country. *PLoS One,* 14**,** e0210885.
ROSANOWSKI, S. M., COGGER, N., ROGERS, C. W. & STEVENSON, M. A. 2016. Evaluating the Effectiveness of Strategies for the Control of Equine Influenza Virus in the New Zealand Equine Population. *Transbound Emerg Dis,* 63**,** 321-32.
ROSSMAN, J. S., JING, X., LESER, G. P., BALANNIK, V., PINTO, L. H. & LAMB, R. A. 2010a. Influenza virus m2 ion channel protein is necessary for filamentous virion formation. *J Virol,* 84**,** 5078-88.
ROSSMAN, J. S., JING, X., LESER, G. P. & LAMB, R. A. 2010b. Influenza virus M2 protein mediates ESCRT-independent membrane scission. *Cell,* 142**,** 902-13.
ROSSMAN, J. S. & LAMB, R. A. 2011. Influenza virus assembly and budding. *Virology,* 411**,** 229-36.
ROSSMAN, J. S., LESER, G. P. & LAMB, R. A. 2012. Filamentous influenza virus enters cells via macropinocytosis. *J Virol,* 86**,** 10950-60.
SAKAI, T., TAKAGI, H., MURAKI, Y. & SAITO, M. 2018. Unique Directional Motility of Influenza C Virus Controlled by Its Filamentous Morphology and Short-Range Motions. *J Virol,* 92.
SATO, R., OKURA, T., KAWAHARA, M., TAKIZAWA, N., MOMOSE, F. & MORIKAWA, Y. 2019. Apical Trafficking Pathways of Influenza A Virus HA and NA via Rab17- and Rab23-Positive Compartments. *Front Microbiol,* 10**,** 1857.
SCHNEIDER, C. A., RASBAND, W. S. & ELICEIRI, K. W. 2012. NIH Image to ImageJ: 25 years of image analysis. *Nat Methods,* 9**,** 671-5.
SCHOLTENS, R. G., STEELE, J. H., DOWDLE, W. R., YARBROUGH, W. B. & ROBINSON, R. Q. 1964. U.S. Epizootic of Equine Influenza, 1963. *Public Health Rep,* 79**,** 393-402.
SCHUSTER, P., FONTANA, W., STADLER, P. F. & HOFACKER, I. L. 1994. From sequences to shapes and back: a case study in RNA secondary structures. *Proc Biol Sci,* 255**,** 279-84.
SELADI-SCHULMAN, J., CAMPBELL, P. J., SUPPIAH, S., STEEL, J. & LOWEN, A. C. 2014. Filament-producing mutants of influenza A/Puerto Rico/8/1934 (H1N1) virus have higher neuraminidase activities than the spherical wild-type. *PLoS One,* 9**,** e112462.
SELADI-SCHULMAN, J., STEEL, J. & LOWEN, A. C. 2013. Spherical influenza viruses have a fitness advantage in embryonated eggs, while filament-producing strains are selected in vivo. *J Virol,* 87**,** 13343-53.
SELZER, L., SU, Z., PINTILIE, G. D., CHIU, W. & KIRKEGAARD, K. 2020. Full-length three-dimensional structure of the influenza A virus M1 protein and its organization into a matrix layer. *PLoS Biol,* 18**,** e3000827.
SHAFIUDDIN, M. & BOON, A. C. M. 2019. RNA Sequence Features Are at the Core of Influenza A Virus Genome Packaging. *J Mol Biol,* 431**,** 4217-4228.
SHAPIRO, G. I. & KRUG, R. M. 1988. Influenza virus RNA replication in vitro: synthesis of viral template RNAs and virion RNAs in the absence of an added primer. *J Virol,* 62**,** 2285-90.
SHAW, M. L., STONE, K. L., COLANGELO, C. M., GULCICEK, E. E. & PALESE, P. 2008. Cellular proteins in influenza virus particles. *PLoS Pathog,* 4**,** e1000085.
SHINYA, K., EBINA, M., YAMADA, S., ONO, M., KASAI, N. & KAWAOKA, Y. 2006. Avian flu: influenza virus receptors in the human airway. *Nature,* 440**,** 435-6.
SIECZKARSKI, S. B. & WHITTAKER, G. R. 2002. Influenza virus can enter and infect cells in the absence of clathrin-mediated endocytosis. *J Virol,* 76**,** 10455-64.
SIMPSON-HOLLEY, M., ELLIS, D., FISHER, D., ELTON, D., MCCAULEY, J. & DIGARD, P. 2002. A functional link between the actin cytoskeleton and lipid rafts during budding of filamentous influenza virions. *Virology,* 301**,** 212-25.
SINGANAYAGAM, A., ZAMBON, M. & BARCLAY, W. S. 2019. Influenza Virus with Increased pH of Hemagglutinin Activation Has Improved Replication in Cell Culture but at the Cost of Infectivity in Human Airway Epithelium. *J Virol,* 93.
SINGH, R. K., DHAMA, K., KARTHIK, K., KHANDIA, R., MUNJAL, A., KHURANA, S. K., CHAKRABORTY, S., MALIK, Y. S., VIRMANI, N., SINGH, R., TRIPATHI, B. N., MUNIR, M. & VAN DER KOLK, J. H. 2018. A Comprehensive Review on Equine Influenza Virus:

Etiology, Epidemiology, Pathobiology, Advances in Developing Diagnostics, Vaccines, and Control Strategies. *Front Microbiol,* 9**,** 1941.
SMOLA, M. J., RICE, G. M., BUSAN, S., SIEGFRIED, N. A. & WEEKS, K. M. 2015. Selective 2'-hydroxyl acylation analyzed by primer extension and mutational profiling (SHAPE-MaP) for direct, versatile and accurate RNA structure analysis. *Nat Protoc,* 10**,** 1643-69.
SMYTH, G. B., DAGLEY, K. & TAINSH, J. 2011. Insights into the economic consequences of the 2007 equine influenza outbreak in Australia. *Aust Vet J,* 89 Suppl 1**,** 151-8.
SOVINOVA, O. & LUDVIK, J. 1959. Electron microscopic study of the influenza virus A-equi-Praha/56. *Acta Virol,* 3**,** 59-60.
STEGMANN, T., WHITE, J. M. & HELENIUS, A. 1990. Intermediates in influenza induced membrane fusion. *EMBO J,* 9**,** 4231-41.
TANG, G., PENG, L., BALDWIN, P. R., MANN, D. S., JIANG, W., REES, I. & LUDTKE, S. J. 2007. EMAN2: an extensible image processing suite for electron microscopy. *J Struct Biol,* 157**,** 38-46.
TEGUNOV, D., XUE, L., DIENEMANN, C., CRAMER, P. & MAHAMID, J. 2021. Multi-particle cryo-EM refinement with M visualizes ribosome-antibiotic complex at 3.5 A in cells. *Nat Methods,* 18**,** 186-193.
TIMONEY, P. J. 1996. Equine influenza. *Comp Immunol Microbiol Infect Dis,* 19**,** 205-11.
VAHEY, M. D. & FLETCHER, D. A. 2019a. Influenza A virus surface proteins are organized to help penetrate host mucus. *Elife,* 8.
VAHEY, M. D. & FLETCHER, D. A. 2019b. Low-Fidelity Assembly of Influenza A Virus Promotes Escape from Host Cells. *Cell,* 176**,** 678.
VAHEY, M. D. & FLETCHER, D. A. 2019c. Low-Fidelity Assembly of Influenza A Virus Promotes Escape from Host Cells. *Cell,* 176**,** 281-294 e19.
VALE-COSTA, S., ALENQUER, M., SOUSA, A. L., KELLEN, B., RAMALHO, J., TRANFIELD, E. M. & AMORIM, M. J. 2016. Influenza A virus ribonucleoproteins modulate host recycling by competing with Rab11 effectors. *J Cell Sci,* 129**,** 1697-710.
VALE-COSTA, S. & AMORIM, M. J. 2017. Clustering of Rab11 vesicles in influenza A virus infected cells creates hotspots containing the 8 viral ribonucleoproteins. *Small GTPases,* 8**,** 71-77.
VASIN, A. V., TEMKINA, O. A., EGOROV, V. V., KLOTCHENKO, S. A., PLOTNIKOVA, M. A. & KISELEV, O. I. 2014. Molecular mechanisms enhancing the proteome of influenza A viruses: an overview of recently discovered proteins. *Virus Res,* 185**,** 53-63.
VIJAYAKRISHNAN, S., LONEY, C., JACKSON, D., SUPHAMUNGMEE, W., RIXON, F. J. & BHELLA, D. 2013. Cryotomography of budding influenza A virus reveals filaments with diverse morphologies that mostly do not bear a genome at their distal end. *PLoS Pathog,* 9**,** e1003413.
VIJAYKRISHNA, D., POON, L. L., ZHU, H. C., MA, S. K., LI, O. T., CHEUNG, C. L., SMITH, G. J., PEIRIS, J. S. & GUAN, Y. 2010. Reassortment of pandemic H1N1/2009 influenza A virus in swine. *Science,* 328**,** 1529.
VREEDE, F. T., GIFFORD, H. & BROWNLEE, G. G. 2008. Role of initiating nucleoside triphosphate concentrations in the regulation of influenza virus replication and transcription. *J Virol,* 82**,** 6902-10.
WANDZIK, J. M., KOUBA, T., KARUPPASAMY, M., PFLUG, A., DRNCOVA, P., PROVAZNIK, J., AZEVEDO, N. & CUSACK, S. 2020. A Structure-Based Model for the Complete Transcription Cycle of Influenza Polymerase. *Cell,* 181**,** 877-893 e21.
WANG, C., LAMB, R. A. & PINTO, L. H. 1995. Activation of the M2 ion channel of influenza virus: a role for the transmembrane domain histidine residue. *Biophys J,* 69**,** 1363-71.
WANG, N., GLIDDEN, E. J., MURPHY, S. R., PEARSE, B. R. & HEBERT, D. N. 2008. The cotranslational maturation program for the type II membrane glycoprotein influenza neuraminidase. *J Biol Chem,* 283**,** 33826-37.
WATANABE, K., SHIMIZU, T., NODA, S., TSUKAHARA, F., MARU, Y. & KOBAYASHI, N. 2014. Nuclear export of the influenza virus ribonucleoprotein complex: Interaction of Hsc70 with viral proteins M1 and NS2. *FEBS Open Bio,* 4**,** 683-8.
WEBSTER, R. G., BEAN, W. J., GORMAN, O. T., CHAMBERS, T. M. & KAWAOKA, Y. 1992. Evolution and ecology of influenza A viruses. *Microbiol Rev,* 56**,** 152-79.
WEBSTER, R. G. & GOVORKOVA, E. A. 2014. Continuing challenges in influenza. *Ann N Y Acad Sci,* 1323**,** 115-39.
WEI, Z., MCEVOY, M., RAZINKOV, V., POLOZOVA, A., LI, E., CASAS-FINET, J., TOUS, G. I., BALU, P., PAN, A. A., MEHTA, H. & SCHENERMAN, M. A. 2007. Biophysical characterization of influenza virus subpopulations using field flow fractionation and multiangle light scattering: correlation of particle counts, size distribution and infectivity. *J Virol Methods,* 144**,** 122-32.

WHITE, J. M. & WHITTAKER, G. R. 2016. Fusion of Enveloped Viruses in Endosomes. *Traffic,* 17**,** 593-614.

WILLIAMS, G. D., TOWNSEND, D., WYLIE, K. M., KIM, P. J., AMARASINGHE, G. K., KUTLUAY, S. B. & BOON, A. C. M. 2018. Nucleotide resolution mapping of influenza A virus nucleoprotein-RNA interactions reveals RNA features required for replication. *Nat Commun,* 9**,** 465.

WILSON, J. C., BRYANS, J. T. & DOLL, E. R. 1965. Recovery of influenza virus from horses in the equine influenza epizootic of 1963. *Am J Vet Res,* 26**,** 1466-8.

WILSON, R. L., FRISZ, J. F., KLITZING, H. A., ZIMMERBERG, J., WEBER, P. K. & KRAFT, M. L. 2015. Hemagglutinin clusters in the plasma membrane are not enriched with cholesterol and sphingolipids. *Biophys J,* 108**,** 1652-1659.

WINEY, M., MEEHL, J. B., O'TOOLE, E. T. & GIDDINGS, T. H., JR. 2014. Conventional transmission electron microscopy. *Mol Biol Cell,* 25**,** 319-23.

WISE, H. M., FOEGLEIN, A., SUN, J., DALTON, R. M., PATEL, S., HOWARD, W., ANDERSON, E. C., BARCLAY, W. S. & DIGARD, P. 2009. A complicated message: Identification of a novel PB1-related protein translated from influenza A virus segment 2 mRNA. *J Virol,* 83**,** 8021-31.

WISE, H. M., HUTCHINSON, E. C., JAGGER, B. W., STUART, A. D., KANG, Z. H., ROBB, N., SCHWARTZMAN, L. M., KASH, J. C., FODOR, E., FIRTH, A. E., GOG, J. R., TAUBENBERGER, J. K. & DIGARD, P. 2012. Identification of a novel splice variant form of the influenza A virus M2 ion channel with an antigenically distinct ectodomain. *PLoS Pathog,* 8**,** e1002998.

WITTE, R., ANDRIASYAN, V., GEORGI, F., YAKIMOVICH, A. & GREBER, U. F. 2018. Concepts in Light Microscopy of Viruses. *Viruses,* 10.

WOODWARD, A., RASH, A. S., MEDCALF, E., BRYANT, N. A. & ELTON, D. M. 2015. Using epidemics to map H3 equine influenza virus determinants of antigenicity. *Virology,* 481**,** 187-98.

YANG, H., NGUYEN, H. T., CARNEY, P. J., GUO, Z., CHANG, J. C., JONES, J., DAVIS, C. T., VILLANUEVA, J. M., GUBAREVA, L. V. & STEVENS, J. 2015. Structural and functional analysis of surface proteins from an A(H3N8) influenza virus isolated from New England harbor seals. *J Virol,* 89**,** 2801-12.

YE, Z., LIU, T., OFFRINGA, D. P., MCINNIS, J. & LEVANDOWSKI, R. A. 1999. Association of influenza virus matrix protein with ribonucleoproteins. *J Virol,* 73**,** 7467-73.

YUSUPOVA, G. & YUSUPOV, M. 2017. Crystal structure of eukaryotic ribosome and its complexes with inhibitors. *Philos Trans R Soc Lond B Biol Sci,* 372.

ZACHS, T., SCHERTEL, A., MEDEIROS, J., WEISS, G. L., HUGENER, J., MATOS, J. & PILHOFER, M. 2020. Fully automated, sequential focused ion beam milling for cryo-electron tomography. *Elife,* 9.

ZANOTTI, G. & GRINZATO, A. 2021. Structure of filamentous viruses. *Curr Opin Virol,* 51**,** 25-33.

ZHANG, J., PEKOSZ, A. & LAMB, R. A. 2000. Influenza virus assembly and lipid raft microdomains: a role for the cytoplasmic tails of the spike glycoproteins. *J Virol,* 74**,** 4634-44.

ZHANG, K., WANG, Z., FAN, G. Z., WANG, J., GAO, S., LI, Y., SUN, L., YIN, C. C. & LIU, W. J. 2015. Two polar residues within C-terminal domain of M1 are critical for the formation of influenza A Virions. *Cell Microbiol,* 17**,** 1583-93.

ZHIRNOV, O. P. 1992. Isolation of matrix protein M1 from influenza viruses by acid-dependent extraction with nonionic detergent. *Virology,* 186**,** 324-30.